



HAL
open science

NMR study of lithium mobility in polymer electrolytes

Tan-Vu Huynh

► **To cite this version:**

Tan-Vu Huynh. NMR study of lithium mobility in polymer electrolytes. Other. Université d'Orléans, 2015. English. NNT: 2015ORLE2054 . tel-01362053

HAL Id: tel-01362053

<https://theses.hal.science/tel-01362053>

Submitted on 8 Sep 2016

HAL is a multi-disciplinary open access archive for the deposit and dissemination of scientific research documents, whether they are published or not. The documents may come from teaching and research institutions in France or abroad, or from public or private research centers.

L'archive ouverte pluridisciplinaire **HAL**, est destinée au dépôt et à la diffusion de documents scientifiques de niveau recherche, publiés ou non, émanant des établissements d'enseignement et de recherche français ou étrangers, des laboratoires publics ou privés.

**ÉCOLE DOCTORALE
ÉNERGIE, MATÉRIAUX, SCIENCES DE LA TERRE ET DE
L'UNIVERS**

Laboratoire CNRS UPR 3079 Conditions Extrêmes et Matériaux :
Haute Température et Irradiation

THÈSE présentée par :

Tan-Vu HUYNH

soutenue le : **4 Novembre 2015**

pour obtenir le grade de : **Docteur de l'université d'Orléans**

Discipline/ Spécialité: **Chimie**

**Etude par Résonance Magnétique Nucléaire
de la mobilité du lithium
dans les électrolytes à base de polymères**

THÈSE dirigée par :

Michaël Deschamps

Professeur, Université d'Orléans

RAPPORTEURS :

Daniel ABERGEL

Directeur de Recherche, Ecole Normale
Supérieure, Paris

Anne-Laure ROLLET

Chargée de Recherches HDR, Université Pierre
et Marie Curie, Paris

JURY :

Renaud BOUCHET

Professeur, Institut Polytechnique de Grenoble

François TRAN VAN

Professeur, Université de Tours

Michaël DESCHAMPS

Professeur, Université d'Orléans

Abstract

Nuclear magnetic resonance (NMR) spectroscopy is well known as a powerful tool to study molecular structure and dynamics. In battery materials, the mobility of lithium cations is especially important as it is the key to the limitations in battery power and charging rates. NMR spectroscopy can give access to self-diffusion coefficients of spin bearing species using pulsed field gradients which measure atomic displacement over 1-2 μm length scales. The relaxation of nuclear spins at high magnetic fields, on the other hand, is governed by fluctuations of NMR interactions resonant with the Larmor frequency, at the nanosecond timescale, and these are usually related to atomic motions over 0.1 - 1 nm.

In this thesis, we recorded self-diffusion coefficients and ^7Li relaxation rates for two polymer electrolytes: LiTFSI in polyethylene oxide (PEO) and in a block-copolymer PS-PEO(LiTFSI)-PS. We first investigated the effect of magic-angle spinning (MAS) on diffusion and relaxation, showing that MAS can help retrieve diffusion coefficient when relaxation is fast and diffusion is slow, and second, that lithium motion is not perturbed by the partial alignment of PEO under MAS induced pressure. The relaxation rates of ^7Li were measured at three high magnetic fields (4.7, 9.4 and 17.6 Tesla) allowing us to perform a simple relaxometry study of Li^+ motion at the nanosecond timescale. In order to reproduce the transverse and longitudinal relaxation behaviors, it proved necessary to introduce a simple model with two correlation times. It showed for the first time that the lithium dynamics in PS-PEO(LiTFSI)-PS is slowed down by the presence of PS domains compared to the pure PEO with similar chain lengths. The results are analyzed and compared to other studies based on molecular dynamics or physical models of diffusion in polymers.

A second series of gel polymer electrolytes based on poly(vinylidene fluoride-co-hexafluoropropylene) (PVdF-HFP), PEGM (Poly ethyleneglycol methyl ether methacrylate)/PEGDM (Poly ethyleneglycol dimethacrylate), and LiTFSI in ionic liquids were also studied. Adding oxygenated polymers to increase the retention of ionic liquids slowed the diffusion down and explained why the battery performance was degraded at higher charging rates.

Acknowledgements

This work was carried out in the laboratory Conditions Extrêmes et Matériaux : Haute Température et Irradiation (CEMHTI)-UPR3079 CNRS, Université d'Orléans, under the direction of Prof. Michaël Deschamps.

I would like to thank Prof. Michaël Deschamps for proposing me this subject, giving a chance to study in NMR world. He has aroused me about the inspiration of science. I would like to thank him also about his kindness, his time to guide me to finish this thesis.

I would like to thank Dr. Robert Messinger for teaching me about NMR experiments, helping me to learn NMR theory, accompanying me throughout my research work sympathetically.

I would like to thank Dr. Vincent Sarou-Kanian for helping to set up NMR experiments, solving out technical problems, sharing his knowledge about NMR. I would like to thank also Dr. Catherine Bessada, director of CEMHTI, for welcoming me for three years.

I would like to thank Prof. Renaud Bouchet from the laboratory of Electrochimie et de Physicochimie des Matériaux et des Interfaces (LEPMI) and Victor Chaudoy from the laboratory Physico-Chimie des Matériaux et des Electrolytes pour l'Energie (PCM2E). They have provided me the materials that were used in this thesis. Thank you a lot for spending your time on discussing about my works.

I would like to thank the jury for reading and correcting my thesis.

A big thank for all peoples working in CEMHTI, for your kindness. Finally, I extend my gratitude to my family in Vietnam, my dear parents, my brother, and my girlfriend who encouraged and supported me.

Contents

Abstract	i
Acknowledgements	ii
Contents	iii
Resumé de la thèse en français	vii
1. Les électrolytes à base de polymères	vii
2. Introduction de Résonance Magnétique Nucléaire	ix
3. L'influence de la rotation à l'angle magique (MAS) sur les expériences de RMN dans les électrolytes polymères	x
4. Caractérisation des temps de relaxation et des coefficients de diffusion	xi
5. Les électrolytes polymères à base de PVdF-HFP	xii
6. Conclusions et perspectives	xiv
1 Lithium metal battery	1
1.1 Lithium metal battery	1
1.2 Ultra-thin lithium metal battery	3
1.3 Solid polymer electrolytes	4
1.4 Ion motion mechanisms	5
1.5 Materials	9
1.6 Difficulties in studying polymer electrolytes	10
2 Introduction to Nuclear Magnetic Resonance	13
2.1 Introduction to NMR	13
2.1.1 The Hamiltonians	13
2.1.2 Spin angular momentum operators	14
2.1.3 Zeeman interaction	15
2.1.4 Chemical shift	15
2.1.5 Dipolar interaction	16
2.1.6 Quadrupolar interaction	17
2.2 Relaxation of nuclear spins to study molecular motion	19
2.2.1 Longitudinal relaxation time T_1	20
2.2.2 Transverse relaxation time T_2	20

2.2.3	Molecular vibrations	21
2.2.4	Molecular flexibility	21
2.2.5	Molecular rotations	22
2.3	How to study molecular motions with relaxation times	22
2.3.1	Angular dependent NMR interactions	22
2.3.2	Auto-correlation functions	23
2.3.3	Determination of the spectral density	25
2.3.4	Spectral densities	25
	2.3.4.1 Bloembergen-Purcell-Pound (BPP) model	26
	2.3.4.2 Cole-Davidson function	26
	2.3.4.3 Lipari-Szabo model	26
2.4	Diffusion	27
2.4.1	Fick's laws	28
2.4.2	Self-Diffusion	29
	2.4.2.1 Introduction	29
	2.4.2.2 Stokes-Einstein equation	30
	2.4.2.3 Random walk theory	30
	2.4.2.4 Diffusion propagators	31
2.4.3	Conductivity and diffusion	32
	2.4.3.1 Mobility of Ions	32
	2.4.3.2 Nernst-Einstein equation	33
2.4.4	Diffusion coefficient measurements by NMR	33
3	The Effect of Magic Angle Spinning on Relaxation and Diffusion	39
3.1	Magic angle spinning	39
3.2	Temperature calibration	40
3.3	Observation	40
3.4	Previous studies	42
3.5	Polymer state control	44
3.6	Diffusion and relaxation time results	47
3.7	Conclusion	50
4	Relaxation times and diffusion coefficient measurement	51
4.1	Introduction	51
4.2	Diffusion coefficient and conductivity of polymer samples	53
4.3	Relaxation rates R_1 and R_2 characterization	60
	4.3.1 Calculation of relaxation rates	60
	4.3.2 Simple models: Bloembergen-Purcell-Pound (BPP) and Cole-Davidson function	62
	4.3.2.1 $\langle C_Q^2 \rangle$ variation	64
	4.3.2.2 Dipolar Relaxation term R_{DD}	66
	4.3.3 Multi-exponentials correlation function	68
4.4	Conclusion	79
5	Polymer electrolytes in ultra thin film battery	81

5.1	Introduction	81
5.2	Experiments	83
5.3	Results and discussions	83
5.4	Conclusions	90
6	Conclusions and Perspectives	91
6.1	Conclusions	91
6.2	Perspectives	92
A	Experimental relaxation rates and calculated parameters	93
A.1	Calculation method	93
A.2	Experimental relaxation rates	94
A.3	The parameters calculated from successful model	97
	Bibliography	99

Resumé de la thèse en français

1. Les électrolytes à base de polymères

L'accumulateur lithium-métal-polymère (LMP) possède une grande capacité et une tension plus élevée grâce à l'utilisation de l'anode en lithium métallique. Cependant, les risques d'incendie et d'explosion limitent l'application de ces types de batteries au quotidien. Ces désavantages viennent de la formation de dendrites de lithium métallique pendant la charge causant des court-circuits. Les électrolytes liquides sont inflammables et peuvent réagir avec les électrodes actives (principalement le lithium métal). Par contre, les électrolytes à base de polymères comme le polyoxyde d'éthylène (PEO) sont de bons candidats pour une utilisation dans les batteries lithium-métal (comme dans la Bluecar d'Autolib...). Deux problèmes sont néanmoins observés dans ces électrolytes: d'abord, la conductivité est plus basse que dans un électrolyte liquide conventionnel, et deuxièmement, leur résistance mécanique est faible et n'empêche pas forcément la formation de dendrites au cours de la charge. Donc, les copolymères à bloc dérivés du PEO et renforcés par des blocs de polystyrène (PS) [1] ont été développés pour augmenter la résistance à la formation de dendrites. La figure 1 montre la composition des électrolytes polymères étudiés dans chapitres 3 et 4.

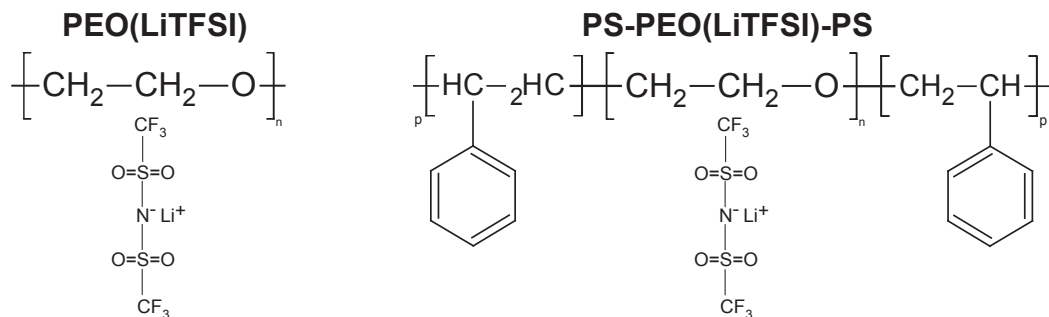


FIGURE 1: La structure des électrolytes polymères étudiés: PEO(LiTFSI) et PS-PEO(LiTFSI)-PS

L'utilisation de la relaxation et de la diffusion vont ainsi permettre de mieux appréhender l'effet des blocs de PS sur la dynamique du Li^+ dans les domaines de PEO. Dans un deuxième temps, un autre type d'électrolyte a aussi été étudié: ils sont réalisés à base de PVdF-HFP -poly(vinylidène fluoride-co-hexafluoropropylène)- sous forme de gels. Ces électrolytes sont utilisés dans des batteries ultra-fines à la place du LIPON (pour oxynitride de lithium et de phosphore $Li_xPO_yN_z$) en raison de leur coût plus faible. Le sel de LiTFSI est ici solubilisé dans un liquide ionique (IL) $Pyr_{13}FSI$ (N-méthyl-N-propylpyrrolidinium bis(fluorosulfonyl)imide) mélangé avec le polymère pour avoir une conductivité plus élevée.

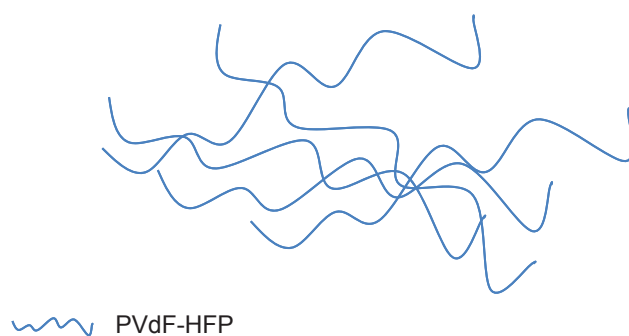


FIGURE 2: Echantillon PH: la solution de LiTFSI dans Pyr₁₃FSI est mélangée avec le PVdF-HFP (©Victor Chaudoy - Université de Tours).

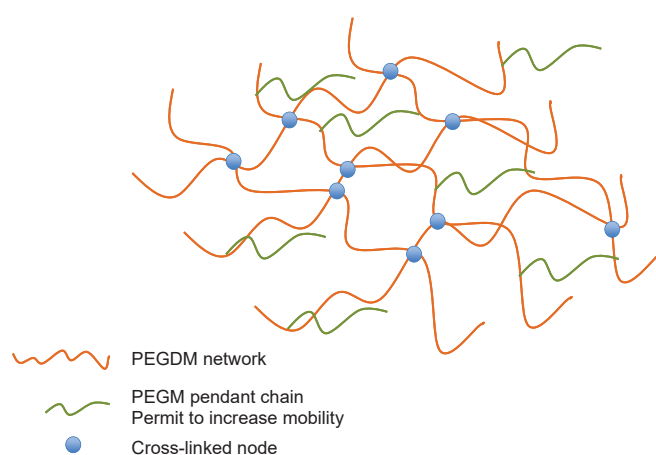


FIGURE 3: Echantillon POE: l'électrolyte (LiTFSI dans le Pyr₁₃FSI) est mélangé avec un polymère PEGDM/PEGM (©Victor Chaudoy - Université de Tours)

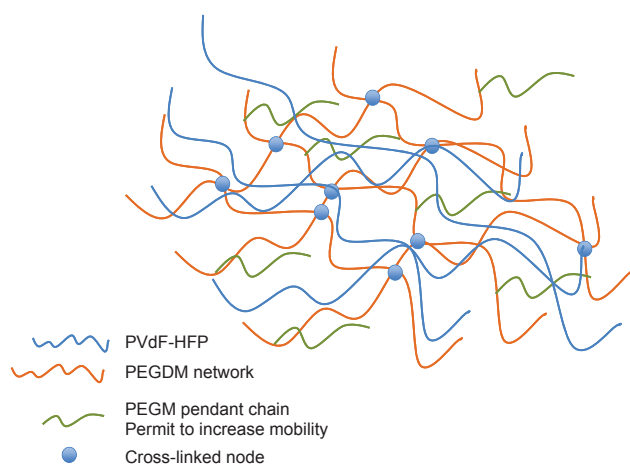


FIGURE 4: Echantillon SRIP: Le polymère est un mélange de PVdF-HFP et de PEGM/PEGDM -sans lien chimique entre eux-, avec le même électrolyte (©Victor Chaudoy - Université de Tours).

Cependant, les membranes poreuses de PVdF-HFP retiennent faiblement le liquide ionique à température plus élevée (60 °C) ce qui cause une perte de IL lorsque le système est assemblé. L'utilisation de polymères de type PEGM (Poly ethyleneglycol methyl ether methacrylate)/PEGDM (Poly ethyleneglycol dimethacrylate) permet d'améliorer la rétention de l'électrolyte mais diminue malheureusement la vitesse de diffusion du lithium par interaction de celui-ci avec le polymère ajouté. Les polymères étudiés sont décrits dans les figures ci-dessus.

2. Introduction de Résonance Magnétique Nucléaire

Dans cette section, nous présenterons les principes de la Résonance Magnétique Nucléaire (RMN) et les différentes méthodes expérimentales utilisées dans cette thèse. Le principal avantage de la spectroscopie RMN réside dans sa capacité à fournir des informations sur la structure (distances ou angles de liaisons) et la dynamique des molécules (relaxation ou diffusion). Dans le cadre de cette étude, la RMN vient compléter les informations données par les mesures de conductivité. La conductivité est un paramètre important dans l'étude des matériaux électrolytes solides comme les polymères, et elle est étroitement liée à la diffusion des cations et des anions dans l'électrolyte. L'utilisation de gradient de champs magnétiques "pulsés" (PFG) donne accès aux coefficients d'auto-diffusion des espèces portant un spin nucléaire détectable. Les coefficients d'auto-diffusion mesurés valent entre 10^{-10} et 10^{-13} m²/s, et les déplacements spatiaux des ions sont mesurés sur des temps variant de 1 ms (pour les espèces rapides) à 1 s (pour les espèces diffusant plus lentement), ce qui correspond à des déplacements ioniques de quelques µm pour la mesure du coefficient d'auto-diffusion. La mesure de la conductivité (plus simple dans sa mise en oeuvre) ne peut mesurer que la somme des contributions de toutes les espèces chargées. Ces deux techniques, ensemble, peuvent se compléter utilement pour étudier le mécanisme de transport dans les électrolytes à base de polymère. [2] Cependant, elles ne peuvent donner qu'une description macroscopique à l'échelle du micromètre. La complexité des phénomènes en jeu montre que ces mesures ne suffisent pas pour comprendre parfaitement la mobilité des cations comme le Li⁺, qui est cruciale pour améliorer la vitesse de charge des batteries au lithium. La mobilité des molécules peut être étudiée via les processus de relaxation (ou de retour à l'équilibre des états de spins) qui sont liés aux fluctuations des interactions des spins avec leur environnement ayant lieu à des fréquences jusqu'à la fréquence de Larmor (soit quelques centaines de MHz).

Dans cette thèse, nous avons ainsi combiné ces deux types d'étude afin de mieux comprendre la mobilité des ions lithium dans les électrolytes à base de polymères.

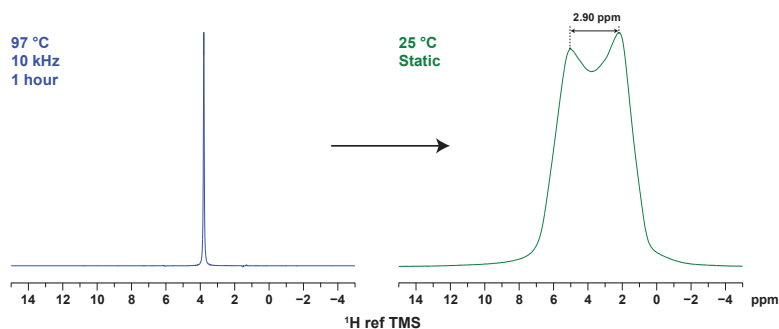


FIGURE 5: Comparaison des spectres RMN du ^1H en MAS (10 kHz) à 97 °C(à gauche) et en condition statique à 25 °C(à droite)

3. L'influence de la rotation à l'angle magique (MAS) sur les expériences de RMN dans les électrolytes polymères

La rotation à l'angle magique (MAS) consiste à faire tourner l'échantillon à grande vitesse selon un axe incliné de 54.74° avec le champ magnétique afin de moyenniser les interactions anisotropes diminuant la résolution du spectre (comme le couplage dipolaire, le déplacement chimique anisotrope, l'interaction quadrupolaire de premier ordre ou les anisotropies de susceptibilité magnétique...). Dans les électrolytes polymères, à température ambiante, les polymères sont suffisamment mobiles pour que les interactions (dipolaires, quadrupolaire...) soient déjà en partie moyennées. Le MAS à vitesse réduite (quelques kHz) est ici utile pour moyenniser les interactions résiduelles (susceptibilité, dipolaire longue distance...) et affiner les pics de ^{19}F et ^7Li aux températures inférieures à T_M .

Cependant, l'apparition d'une forme de raie en doublet sur les spectres acquis en conditions statiques (sans MAS) après rotation en MAS de l'échantillon suggère que la rotation rapide engendre une orientation résiduelle des chaînes de polymères et une modification du tenseur de susceptibilité magnétique comme cela a été montré par d'autres groupes.[3] Cet élargissement est le même en ppm sur tous les spectres (^1H , ^{19}F et ^7Li). Un exemple est donné ici avec le spectre ^1H après que l'échantillon de PEO(LiTFSI) ait subi la rotation à l'angle magique à 10 kHz (voir figure 5). Le chauffage de l'échantillon permet de retrouver un spectre isotrope.

Les mesures de relaxation longitudinale et de diffusion avec et sans MAS ont permis de montrer que le MAS avait une certaine influence sur les résultats de diffusion, mais relativement peu sur les temps de relaxation longitudinale, et par conséquent, le MAS pouvait avoir un effet modéré sur la dynamique du lithium au niveau macroscopique, et moins au niveau microscopique.

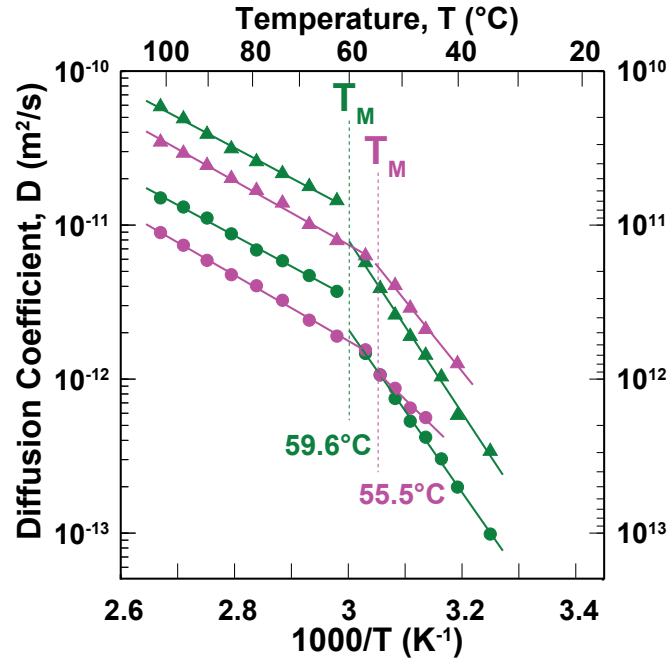


FIGURE 6: Les coefficients d’auto-diffusion de Li^+ (●), TFSI^- (▲) dans $\text{PEO}(\text{LiTFSI})$ et $\text{PS-PEO}(\text{LiTFSI})\text{-PS}$ mesurés dans un échantillon statique. Les énergies d’activation sont calculées pour les coefficients de diffusion en utilisant la loi d’Arrhenius. Les températures de fusion de $\text{PEO}(\text{LiTFSI})$ et $\text{PS-PEO}(\text{LiTFSI})\text{-PS}$ sont estimées ici à environ 59.6 et 55.5 °C.

4. Caractérisation des temps de relaxation et des coefficients de diffusion

Dans cette section, nous étudierons la mobilité du Li^+ au niveau microscopique (en utilisant les temps de relaxation) et macroscopique (avec les mesures de diffusion par PFG, conductivité, etc...). Pour éviter les effets éventuels du MAS, nous avons choisi de réaliser les expériences en condition statique.

La figure 6 présente les coefficients d’auto-diffusion (D) de Li^+ et TFSI^- dans les polymères $\text{PEO}(\text{LiTFSI})$ et $\text{PS-PEO}(\text{LiTFSI})\text{-PS}$. Ils ont été mesurés de telle sorte que le libre parcours moyen λ des ions durant le temps de diffusion Δ était d’environ 2 μm en utilisant l’équation: $\lambda = \sqrt{6D\Delta}$.

Nous avons mesuré les temps de relaxation longitudinale et transverse du ^7Li à trois champs magnétiques (4.7, 9.4 et 17.6 T) en fonction de la température de 25 à 100 °C. Nous avons observé que la relaxation longitudinale est mono-exponentielle avec un seul temps caractéristique T_1 , tandis que la relaxation transverse a un comportement bi-exponentiel pour $\text{PEO}(\text{LiTFSI})$ (si $T < T_M$) et $\text{PS-PEO}(\text{LiTFSI})\text{-PS}$ (à toute température). Les temps de relaxation longitudinale et transverse sont ensuite interprétés en utilisant le logiciel Maple (Maple est produit par Waterloo Maple Inc.) à l’aide d’un modèle à quatre variables, le plus simple possible, décrivant la relaxation des ^7Li comme provenant principalement

de l'interaction quadrupolaire et d'une perturbation d'origine dipolaire (on négligera les termes croisés).

Brièvement, nous avons considéré que l'interaction quadrupolaire fluctue à trois différentes échelles de temps:

- a. Les mouvements très rapides: la vibration du lithium ou des atomes de polymères, qui affecte la valeur de l'interaction quadrupolaire effective $\langle C_Q^2 \rangle$, dépendante de la température.
- b. Les fluctuations dans la sphère de coordination des ions lithium, formée par les atomes d'oxygènes voisins: arrivée ou départ d'un oxygène, ou réorientation de l'ensemble du polyèdre de coordination par mouvements concertés des chaînes de polymère. Ces fluctuations vont mener à un moyennement partiel de l'interaction quadrupolaire (décrit par le paramètre d'ordre S^2) avec une échelle de temps τ_1 .
- c. Sur une échelle de temps plus longue (τ_2), le lithium s'est déplacé dans un autre environnement dans lequel son interaction quadrupolaire a une orientation complètement différente.

Ce modèle nous a permis d'expliquer la relaxation de Li^+ dans nos électrolytes polymères. Les paramètres obtenus après ajustement sont présentés dans la figure 7. Le point le plus important est que nous avons prouvé le ralentissement induit par les blocs de PS sur les mouvements microscopiques du lithium, en contradiction avec l'hypothèse communément admise: la conductivité est identique dans le polymère homogène PEO(LiTFSI) et dans les domaines de PEO du copolymère PS-PEO(LiTFSI)-PS.[4, 5] Ceci implique que la différence entre coefficients de diffusion (voir figure 6) n'est pas seulement un effet "géométrique" du à la tortuosité des domaines de PEO.

5. Les électrolytes polymères à base de PVdF-HFP

Ce projet est une collaboration entre le laboratoire "Physico Chimie des Matériaux et des Electrolytes pour L'Energie" (PCM2E) à Tours et le CEMHTI. Le but de ce projet était de comprendre pourquoi l'ajout d'un polymère oxygéné a des conséquences négatives sur la capacité des batteries ultra-fines à vitesses de charge élevées (C ou 2C soit une charge complète en 1 heure ou 1/2 heure). Ce polymère avait pour but d'améliorer la rétention de l'électrolyte au sein de la membrane poreuse, et même si la conductivité diminuait avec l'ajout de polymère oxygéné, il restait à confirmer que le lithium était bien ralenti par ce polymère (et pas seulement les autres espèces, le cation du LI et les anions).

Les coefficients de diffusion des différentes molécules des échantillons ont été mesurés. Le coefficient de diffusion de Li^+ est maximal pour une concentration de LiTFSI de $x = 1.3$

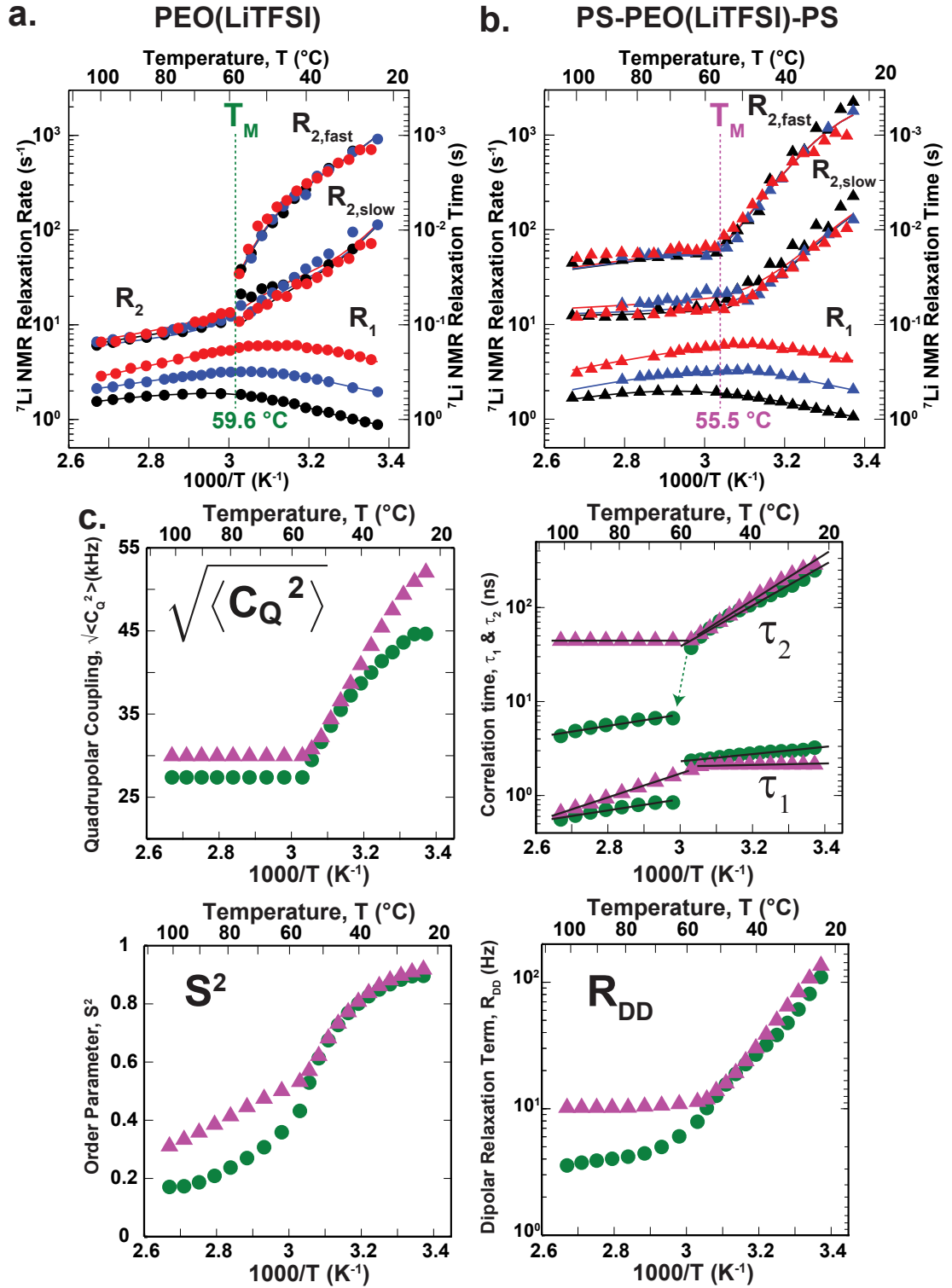


FIGURE 7: a. et b. Les vitesses de relaxation R_1 (partie basse de la graphique) et R_2 (partie haute du graphique) observées pour le ^{7}Li sous trois champs magnétiques (17.4 T, 9.4 T, 4.7 T) en fonction de la température. Les lignes continues et pointillées représentent les courbes ajustées pour R_1 et R_2 . La figure (c) présente les paramètres ajustés $\sqrt{\langle C_Q^2 \rangle}$, τ_1 et τ_2 , S^2 et R_{DD} dans PEO(LiTFSI)(●) et PS-PEO(LiTFSI)-PS(▲). Les énergies d'activation sont calculées pour τ_1 et τ_2 en utilisant la loi d'Arrhenius.

M. Les coefficients de diffusion de Li^+ des échantillons SRIP sont plus faibles que dans les échantillons sans polymère oxygéné. De plus, le ratio PEGM:PEGDM n'a pas d'effet sur la diffusion du lithium.

La présence d'interactions entre Li^+ et le polymère oxygéné est confirmée par le caractère bi-exponentiel de la relaxation transverse du ^7Li dans les échantillons SRIP et POE (comme cela est détaillé dans le chapitre 5).

6. Conclusions et perspectives

Dans cette thèse, nous avons cherché à caractériser la mobilité du Li^+ dans les électrolytes à base de polymère, à l'échelle du nanomètre avec la relaxation des spins nucléaires, et à l'échelle du micromètre avec la mesure de coefficients de diffusion par gradients de champ pulsés. Pour pouvoir interpréter les vitesses de relaxation du ^7Li , nous avons réussi à développer une nouvelle fonction de corrélation des interactions quadrupolaires subies par Li^+ dans un polymère. Ces résultats peuvent ensuite être combinés au sein de modèle théorique tpe "Rouse".

Dans le futur, nous pourrons aussi appliquer la même démarche sur d'autres matériaux comme PSTFSILi-PEO-PSTFSILi. Par ailleurs, des études de dynamique moléculaires pourront être réalisées afin d'affiner notre compréhension de la relaxation.

En parallèle, les outils développés ont pu être utilisés sur des électrolytes à base de PVdF-HFP et nous donne des résultats très intéressants. L'ajout de polymères oxygénés PEGM/PEGDM permet d'améliorer la rétention de l'électrolyte dans les pores de la membrane, cependant, la diffusion des ions Li^+ est ralenties ce qui nuit aux propriétés de la batterie à vitesse de charge élevée.

Dans le futur, nous pourrons aussi envisager des études similaires mais en condition in situ, de façon à prendre en compte les modifications éventuelles des polymères lors de l'assemblage des cellules.

Chapter 1

Lithium metal battery

1.1 Lithium metal battery

The development of mobile electronic technology and the need for clean energy storage lead to the development of battery industry. In particular, the electric car is expected to play an important place in near future, as 27 % of the world's energy consumption concerns transportation.[6] Batteries which possess a high energy density are becoming more and more necessary, as most systems do not yet offer enough capacity to compete with fossile fuels.

Presented by Sony in 1991, the Li-ion battery is based on a graphite anode and have been developed during more than two decades. However, their improvement is threatened due to the theoretical performance limits of both cathode and anode materials. [6, 7]

The use of metallic lithium as anode in batteries started in the 70s.[6] This was due to its high theoretical specific capacity (3860 mAh/g for the anode), its lightest weight metal ($M=6.94$ g/mol, $\rho=0.59$ g/cm³), and to its lowest negative electrochemical potential (-3.040 V vs the standard hydrogen electrode).[8] Moreover, polymer electrolytes can withstand the reductive power of metallic lithium. Figure 1.2 depicts a lithium-metal polymer battery, as the one used in the Bluecar from the Bolloré company. It must be noted that the "LiPo" batteries that are found on the market have no polymer electrolyte and are in fact, Li-ion batteries.

However, the formation of lithium dendrites during repeated charge/discharge cycles is still the biggest problem of this kind of batteries, as seen in figure 1.1.

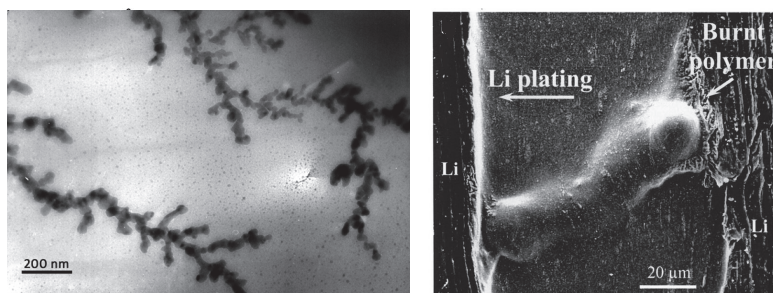


FIGURE 1.1: Formation of lithium dendrite in a solid polymer electrolyte, adapted from G.M. Stone, UC Berkeley and LBNL (left) and ref [9](right)

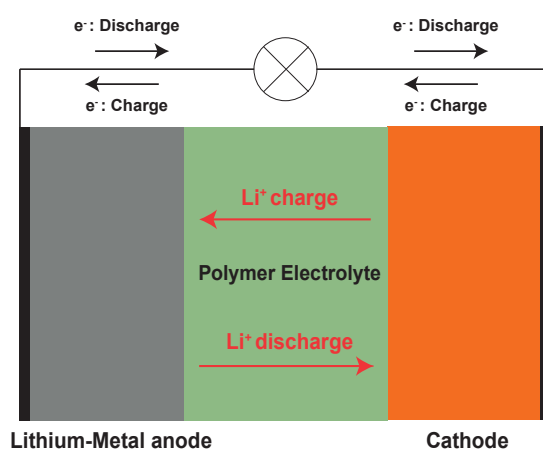


FIGURE 1.2: Lithium-metal-polymer battery

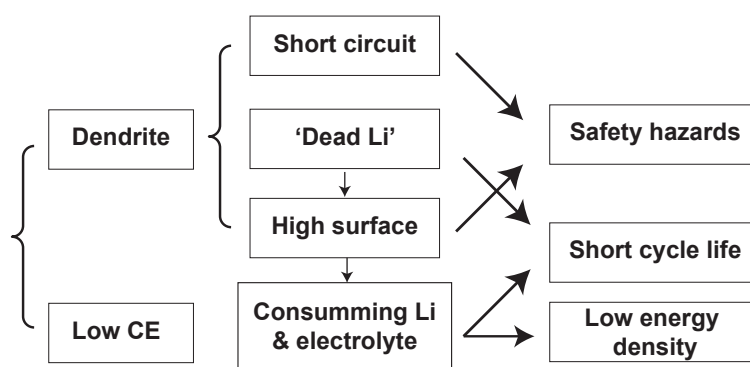


FIGURE 1.3: The consequences of metallic lithium dendrites formation in batteries, adapted from ref [8]

The formation of dendrites causes internal short-circuits and limits the battery life. Furthermore, it can lead to explosion or fires, which are the biggest issue for common usage of these batteries. Figure 1.3 shows the consequences of the development of lithium dendrites.

There are many ways to prevent the formation of lithium dendrites:[8] using solid electrolyte interphases (SEI), polymer electrolytes or self-healing electrostatic

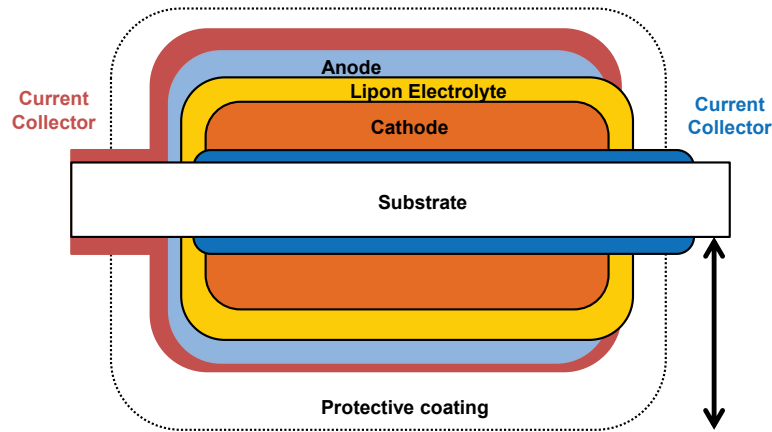


FIGURE 1.4: Schematic cross-section of a thin-film lithium battery, adapted from ref [11].

shields (SHES).

However, to date, there is no electrolyte that can simultaneously prevent lithium dendrites' growth, enhance Coulombic efficiency and performance rate in Li-metal electrodes. [7]

1.2 Ultra-thin lithium metal battery

The appearance of smart cards, sensors, implantable defibrillators or neural stimulators leads to the study of thin-film batteries.[10] Figure 1.4 shows the construction of a thin-film lithium battery. Similarly to common batteries seen in figure 1.2, the thin-film batteries have more or less the same construction, however, compared to the usual batteries with 100 μm -thick electrodes, the overall thickness of these batteries is around 20-30 μm . [11]

The preparation of a thin-film battery is somewhat different from what is done for common batteries. Patil et al. [12] have reviewed some methods used to prepare anode, cathode and electrolyte in thin-film batteries: vacuum thermal vapor deposition -VD- (usually used for Li-metal as anode), RF sputtering -RFS-, RF magnetron sputtering -RFMS-, chemical vapor deposition -CVD-, electrostatic spray deposition -ESD-, pulsed laser deposition -PLD-. Furthermore, Dudney et al. [11] have reviewed also methods like electron cyclotron resonance, and aerosol spray coating.

Dudney et al. [10, 13–15] have developed processes to prepare the physical vapor phase deposition method. The battery cells were prepared onto an insulating substrate, as seen in figure 1.4.

The famous LiPON electrolyte (for lithium phosphorus oxynitride $\text{Li}_x\text{PO}_y\text{N}_z$), which was invented at the Oak Ridge National Laboratory in the early 1990s, [11, 16] is widely used in thin film battery. [11] Importantly, LiPON expressed the single conducting of Li^+ with conductivity is up to $2.3 \pm 0.7 \times 10^{-6}$ S/cm at 25 °C, it has a wide electrochemical window (up 5.5 V versus Li/Li⁺), and no degradation and reaction are observed at the Li/LiPON interface. [17]

On the other hand, the use of polymer electrolytes in thin-film batteries was investigated.[11, 18–20] Two main advantages of polymer electrolytes over LiPON in thin-film batteries are: [12]

- a. Simpler fabrication of thin electrolyte film by casting or spin-coating;
- b. Broader range of electrode and/or cell designs.

1.3 Solid polymer electrolytes

The polymer electrolytes were developed for lithium-metal batteries in order to replace liquid electrolytes to improve their safety. The first polymer used as ionic conductor is polyethylene oxide (PEO) containing sodium and potassium thiocyanates and sodium iodide in the works of Fenton et al. [21] Armand et al. [22] have realized the PEO form complexes with the salts and introduced the notion of solid polymer electrolytes (SPE). In this thesis, we will consider "dry polymer electrolytes" in chapters 3, 4 and hydrid-polymer electrolytes in chapter 5.

The SPEs are expected to be the best technical solution for an all-solid-state battery with good mechanical and electrochemical properties, higher energy density and easy tailoring. [12] However, the SPEs have a lower conductivity at room temperature than liquid electrolytes (LEs). Therefore, the usage of SPEs in lithium batteries requires a better understanding of the fundamentals of ion dissociation and transport. [23]

Therefore, researchers are still paying attention on SPEs, especially for in lithium-metal batteries. [5, 24] The advantages of SPEs are: [25]

- They possess much higher mechanical strengths than liquid electrolytes. Thus, SPEs can prevent the formation of lithium dendrites.
- SPEs can possess high electrochemical stability (or the electrochemical stability window) which can be extended from 0 V to as high as 4-5V.
- A high chemical stability prevents undesired chemical reactions at the electrode/electrolyte interfaces.
- The high thermal stability is also important because such batteries operate at high temperature (around 80 °C[23]).

1.4 Ion motion mechanisms

We will assume that the electrolyte is completely dissociated in solvent. The temperature-dependence of ionic conductivity σ in the polymer electrolyte may follow a Vogel-Tamman-Fulcher (VTF) equation [25]

$$\sigma = AT^{-1/2} \exp \left[\frac{-B}{(T - T_0)} \right] \quad (1.1)$$

where A is pre-exponential factor, T_0 is a reference temperature which is usually identical to T_g and B is the pseudo-activation energy. The Williams-Landel-Ferry (WLF) theory is an extension of the VTF model. It is based on "free volume theory". [26] The WLF equation can be written as:

$$\log \left[\frac{\sigma(T)}{\sigma(T_{ref})} \right] = \log(a_T) = -\frac{C_1(T - T_{ref})}{C_2 + T - T_{ref}} \quad (1.2)$$

where T_{ref} is a reference temperature, a_T is the shift factor, C_1 and C_2 are constants. The free volume theory is based on the assumption that ion transport is governed by the semi-random motion of short polymer segments which creates free volumes for ions to migrate into.[26] In this theory, ion hopping is therefore strongly coupled with the relaxation/breathing and/or segmental motion of polymer chains. [25]

On the other hand, the Arrhenius law behavior (which is observed for lithium diffusion in our systems, between RT and 100 °C) is usually associated to "simple"

hopping mechanisms, which may be "decoupled" from the breathing of polymer-chains: [25]

$$\sigma = \sigma_0 \exp\left(\frac{-E_a}{kT}\right) \quad (1.3)$$

Beside these models, the dynamic bond theory (DBP) [27] is also interesting. It takes into account the dependence of ionic motion rates on the fluidity, or the rate of segmental motion, of the polymer host. [28] The description of the time-dependent hopping probability is linked to the structural evolution of the polymer host. [27] The master equation of the probability of finding a particle at site i at time t is:

$$\dot{P}_i(t) = \sum_{j \neq i} [P_j(t) w_{ji} - P_i(t) w_{ij}] \quad (1.4)$$

where w_{ij} is the probability rate of hopping from site i to site j .

$$w_{ij} = \begin{cases} 0, & \text{when path } (i, j) \text{ not available} \\ w, & \text{when path } (i, j) \text{ available} \end{cases} \quad (1.5)$$

The fraction of available path is defined as: $0 \leq f \leq 1$

The amorphous phase was believed to give rise to efficient ion transport. [29] Berthier et al. have studied SPEs P(EO)₈LiCF₃SO₃ and P(EO)₁₀NaI. The a.c. impedance measurements have shown that the conductivity of P(EO)₈LiCF₃SO₃ follows the Arrhenius law above and below 328 K. On the other hand, the conductivity of P(EO)₁₀NaI is following the VTF law above 322 K, but below this temperature the Arrhenius behavior was observed. The NMR experiments have shown the melting of pure PEO (at 328 K) and the existence of PEO salt-rich complexes (above 328 K) which progressively dissolve in the elastomeric phase. They have found that the ionic motion mainly occurs within the amorphous phase but not in the crystalline phase. Choi et al. [30] have studied the SPEs system of P(EO) _{n} LiClO₄ ($n = 8, 10, 16, 64$) by the conductivity of SPEs during consecutive thermal cyclings. The presence of a crystalline phase induces lower conductivities. They observed a strong dependence of conductivity on cooling/heating rates and on the previous thermal history of materials.

The works of Gadjourova et al. [31] provided us with new results. Using the polymer electrolyte with composition P(EO)₆:LiSbF₆ ($M_w=1000\text{g/mol}$), -i.e. 6 units of ether oxygen per lithium ion- a purely crystalline phase was prepared.

They observed that the conductivity in the crystalline phase was higher than in the equivalent amorphous phase ($M_w=100000$ g/mol) above T_g . It was explained by the presence of permanently opened pathways for ionic transport. They described these pathways like tunnels in which Li^+ can diffuse easily. The anions stay outside these tunnels and are immobile with respect to the polymer chains. Therefore, the transport number t_+ is expected to be 1.

Golodnitsky et al. [32] studied stretched and unstretched SPEs system with composition $\text{P}(\text{EO})_n:\text{LiI}$ ($3 \leq n \leq 100$). The high-temperature stretched SPEs (at T_M) had more ordered fibers than room-temperature stretched ones. The room-temperature longitudinal ionic conductivity of the former is also higher than the latter one. However, Marzantowicz et al. [33] pointed out that the previous authors did not consider the amorphous phase surrounding the crystalline one whose width and alignment depend on the crystallization regime. Therefore, the ionic transport may not take place only in the crystalline phase. They found the opposite, a decrease of ionic conductivity with the degree of crystallinity. [33]

It was believed that the diffusivity or mobility of the ions is related to the motion of polymer chains. [34, 35] An effort was put to produce SPEs having T_g as low as possible in order to have a better segmental motion at room temperature. [34] Shi et al. [36] have shown that the ionic conductivity in $\text{PEO}(\text{LiCF}_3\text{SO}_3)$ and $\text{PEO}(\text{Mg}(\text{CF}_3\text{SO}_3)_2)$ polymer electrolytes decreased with the molecular weights then were constant at a certain molecular weight. The same observation was seen for Li^+ diffusion coefficient at 70 and 90 °C (using PFG-NMR) in this paper.

We should not forget the mechanical properties of SPEs for a use in lithium-metal batteries. Cross-linked polymer electrolytes were made to meet this requirement. [37] It can be physical or chemical crosslinking. [38] The former has one disadvantage : phase separation lead to a phase that does not contribute to conductivity. Another material was presented, based on stiff macromolecules with short flexible polyoxyethylene side chains attached. [39] It is expected that the side-chain matrix supports the ion conductivity.

Block-copolymers electrolytes were introduced with the idea of combining a conducting polymer with another one having a high mechanical strength. Giles et al. [40] have shown that ABA triblock copolymers (styrene-butadiene-styrene) with short PEO chains grafted on the B block can be used as electrolytes. Alloin et

al. [41] introduced an ABA block-copolymer where A is POS -poly(oxystyren)- or PAGE -poly(allyle glycidyl ether)- and B is PEO(LiTFSI).

Singh et al. [1] used polystyrene-*block* -poly(ethylene oxide) doped with LiTFSI. In contrast with Shi,[36] Singh have seen an increase of Li^+ diffusion coefficient with increasing molecular weigh. It was explained by the higher stretching degree of PEO chains with higher molecular weights in comparison to the ones with lower molecular weights. The more the chains are stretched the more difficult it is to coordinate PEO with Li^+ ions tightly, leading to faster Li^+ diffusion coefficient.

Niitani et al. [42] studied a tri-block copolymer PS-*b*-PPME(LiClO_4)-PS where PPME is poly(ethylene glycol) methyl ether methacrylate with PEO. The conductivity of this copolymer with a ratio of $[\text{Li}]/[\text{EO}]=0.05$ is relatively high at room temperature at 2×10^{-4} S/cm.

The transport numbers of each ion, as mentioned above, is an important parameter. The conductivity of SPEs has contributions from both, anion and cation. The mobility of the anion may cause concentration polarization near the electrode surfaces during battery operation. [43] Schaefer et al. [44] have mentioned that low t_+ will lead to problems such as low device performance due to ion concentration gradient and high internal resistances. Especially, in lithium-metal batteries, the ion concentration gradient can destabilize the electrolyte-electrode interface, leading to lithium dendrite formation. [44]

One method to enhance the transference number of cations is to use composite SPEs. Bronstein et al. [45] have reported the following strategy: tether anions directly to the inorganic component using silane with a sodium phosphate group. The transference number t_+ was enhanced up to 0.9. Mathews at al. [46] used the strong interaction between the triflate anions and boron sites of inorganic particles, leading to highest t_+ of Li^+ up to 0.89.

Another way is to incorporate the anion into the polymer chain such as: the end-capped PEO(SO_3Li)₂,[47] the system of PEO/salt hybrids,[48] the system of PEO separated by 5-sulfoisophthalate unit. [49]

Recently, Bouchet el al.[5] have developed a new single-ion conductor based on tri-block copolymer PSTFSILi-PEO-PSTFSILi where the anions TFSI⁻ were grafted on the PS part. This polymer has advantages as the conductivity reaches up to 1.3×10^{-5} S/cm at 60 °C with 20 %wt of P(STFSILi), the transport number of

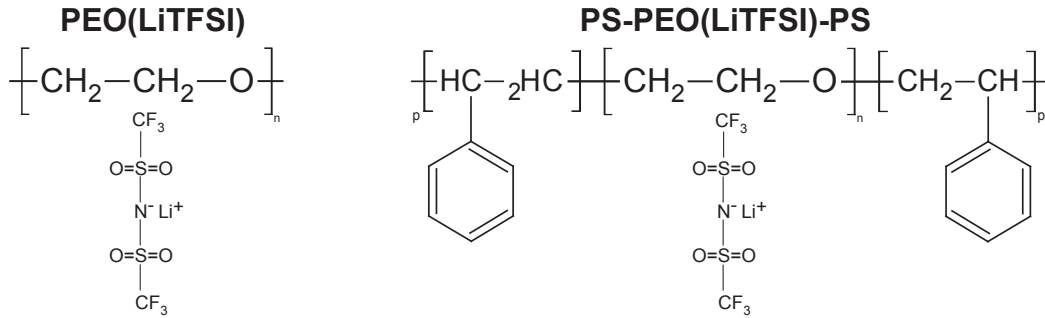


FIGURE 1.5: Molecular structures of the PEO(LiTFSI) and PS-PEO(LiTFSI)-PS polymers that will be studied in chapters 3 and 4.

Li^+ is greater than 0.85, and it has a better mechanical strength than neutral PS-PEO-PS and a larger electrochemical window than PEO (up to 5 V versus Li^+/Li). Figure 1.5 shows the molecular structures of PEO(LiTFSI) and PS-PEO(LiTFSI)-PS. These materials were prepared according to Bouchet et al. [50].

1.5 Materials

In chapters 3 and 4, we will study two solid polymer electrolytes based on poly(ethylene oxide)-PEO- with lithium bis(trifluoromethane)sulfonimide (LiTFSI). Figure 1.5 shows the molecular structures of PEO(LiTFSI) and PS-PEO(LiTFSI)-PS. These materials were prepared according to Bouchet et al. [50].

The molecular weights of PEO (provided by batScap Company) are 100 000 and 35 000 g/mol in PEO(LiTFSI) and in PS-PEO(LiTFSI)-PS, respectively. For homogeneous polymer electrolyte, PEO(LiTFSI) was prepared by using an acetonitrile casting technique. LiTFSI salt was added into the PEO solution whether the molar ratio of EO:Li=30. For block copolymer, the molecular weight of the PS domain is 7 500 g/mol which is a product from Aldrich. The triblock copolymer was made by the ATRP method. The block copolymer electrolyte was mixed with LiTFSI (molar ratio O:Li=30) by using dichloromethane/acetonitrile (50% v/v).

The final solution was stirred for hours, and casted onto Teflons Petri dish. Then, the solvents were allowed to evaporate slowly at 20 °C for 24h. The films were annealed under vacuum for 24 h at 50 °C to eliminate the remaining solvent, then placed in a glove box filled with argon ($\text{H}_2\text{O} < 1$ ppm, Jacomex) for 1 week.

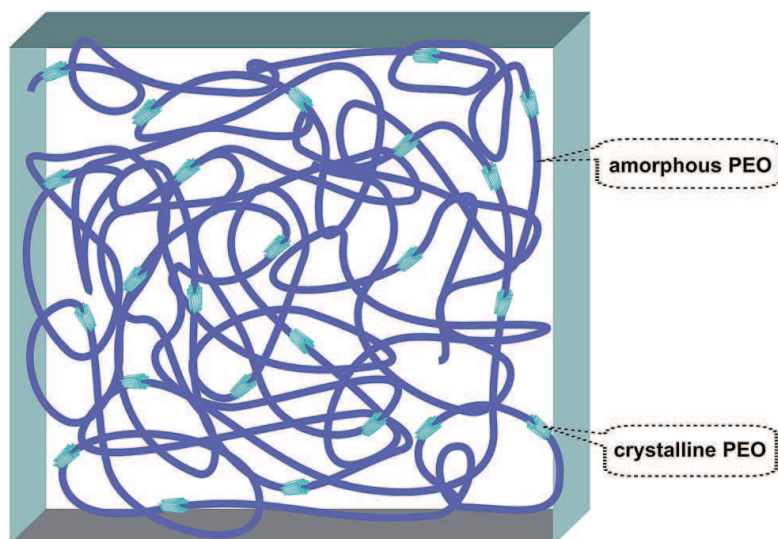


FIGURE 1.6: The appearance of PEO crystalline domains in PEO sample (figure adapted from ref [51])

1.6 Difficulties in studying polymer electrolytes

The first difficulty concerns the long duration of the diffusion experiments. As the diffusion processes are slower at low temperatures, longer diffusion delays are necessary although relaxation times (T_2 and T_1) are shorter, leading to signal loss.

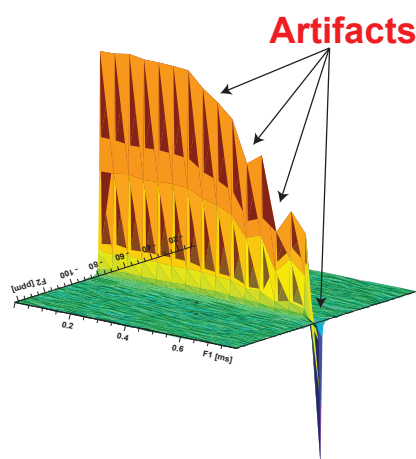


FIGURE 1.7: Artifacts appearing when applying high gradient strength

The most difficult part is to control the polymer state. To ensure the reproducibility of the NMR measurements (diffusion, relaxation time), the polymer "structural" state should more or less be the same for each experiments. However, there is always formation of PEO crystalline domains in the PEO polymer electrolyte (see figure 1.6), the kinetics of which are hard to control. This leads to a sensitivity towards the heat treatment history. Therefore, the polymer was melted and

quenched before each series of measurements, to ensure that the amount of glassy state was maximized, and the data points that are shown here are the results of the averaging of several results.

Another difficulty comes from Magic angle spinning (MAS), which averages the NMR anisotropic interactions and increases the sensitivity. We found that the induced pressure (caused by centrifugal forces) can modify the morphology of our polymer electrolytes, and induces alignment of the polymer chains. It leads to a splitting in the NMR signal in ^1H , ^{19}F and ^7Li static spectra after MAS. This effect is discussed in details in chapter 3.

Beside these issues, instrumental problems (see figure 1.7), such as the tumbling of rotor during high gradient pulse in static conditions, lead to artifact in the signals (see figure 1.7), and the resulting "decay" (as we can see in figure) is not due to diffusion. To fix this problem, we can physically block the rotor.

Chapter 2

Introduction to Nuclear Magnetic Resonance

2.1 Introduction to NMR

2.1.1 The Hamiltonians

The Hamiltonian operator presents the relevant interactions in the system. One can write the Schrödinger equation of the system formed by the nuclear spins: [52]

$$\frac{d}{dt} |\psi(t)\rangle = -i\hat{\mathcal{H}} |\psi(t)\rangle \quad (2.1)$$

where $|\psi\rangle$ is the wave function of spin nuclei, $\hat{\mathcal{H}}$ is the spin Hamiltonian.

With ${}^7\text{Li}$, the Hamiltonian interactions can be written as: [53]

$$\hat{\mathcal{H}} = \hat{\mathcal{H}}_Z + \hat{\mathcal{H}}_Q + \hat{\mathcal{H}}_{D,II} + \hat{\mathcal{H}}_{D,IS} + \hat{\mathcal{H}}_{CS} + \hat{\mathcal{H}}_{RF} \quad (2.2)$$

where $\hat{\mathcal{H}}_Z$ is the Zeeman Hamiltonian interaction, $\hat{\mathcal{H}}_Q$ is the quadrupolar interaction, $\hat{\mathcal{H}}_{D,II}$ is the homonuclear dipolar interaction, $\hat{\mathcal{H}}_{D,IS}$ is the heteronuclear dipolar interaction, $\hat{\mathcal{H}}_{CS}$ is the chemical shift term, and $\hat{\mathcal{H}}_{RF}$ describes the effect of the RF (radio frequency)-pulses. These interactions will be discussed in detail later.

We can define the density operator which describes the quantum state of the entire ensemble: [52]

$$\hat{\rho} = |\psi\rangle \langle\psi| \quad (2.3)$$

Then the Liouville-von Neumann equation, which is important in calculation of dynamic processes in quantum mechanical systems [54], can be defined as:

$$\frac{d}{dt}\hat{\rho}(t) = -i [\hat{\mathcal{H}}(t), \hat{\rho}(t)] \quad (2.4)$$

If the Hamiltonian is time independent, its solution is given by:

$$\hat{\rho}(t) = e^{-i\hat{\mathcal{H}}t} \hat{\rho}(0) e^{i\hat{\mathcal{H}}t} \quad (2.5)$$

2.1.2 Spin angular momentum operators

The spin angular momentum operators of spin I are denoted as three components: $\hat{I}_x, \hat{I}_y, \hat{I}_z$. They have cyclic commutation relationships :

$$[\hat{I}_x, \hat{I}_y] = i\hat{I}_z \circlearrowleft \quad (2.6)$$

Then \hat{I}^2 can be defined:

$$\hat{I}^2 = \hat{I}_x^2 + \hat{I}_y^2 + \hat{I}_z^2 \quad (2.7)$$

For a spin I where I is the quantum number, M is the azimuthal quantum number, we have

$$\hat{I}_z |I, M\rangle = m |I, M\rangle \quad (2.8a)$$

$$\hat{I}^2 |I, M\rangle = I(I+1) |I, M\rangle \quad (2.8b)$$

The shift operators \hat{I}_- and \hat{I}_+ were defined:

$$\hat{I}_+ = \hat{I}_x + i\hat{I}_y \quad (2.9a)$$

$$\hat{I}_- = \hat{I}_x - i\hat{I}_y \quad (2.9b)$$

Therefore,

$$\hat{I}_{\pm} |I, M\rangle = \sqrt{I(I+1) - M(M \pm 1)} |I, M \pm 1\rangle \quad (2.10)$$

2.1.3 Zeeman interaction

This is the strongest and most important interaction. When one puts the nucleus under the magnetic field \vec{B}_0 , the interaction of the magnetic moments of the nuclei $\vec{\mu}$ with the magnetic field \vec{B}_0 is called the Zeeman effect. The Hamiltonian describing the Zeeman interaction is:

$$\hat{\mathcal{H}} = -\gamma B_0 \hat{I}_z = \omega_0 \hat{I}_z \quad (2.11)$$

where ω_0 is the Larmor frequency, the rate at which the spins rotate around the magnetic field. The Larmor interaction is responsible for the difference in energy between the spin eigenstates $+1/2$ and $-1/2$ (for a spin $1/2$) or $+3/2$, $+1/2$, $-1/2$ and $-3/2$ (for a spin $3/2$), and the existence of a macroscopic magnetization along the magnetic field axis, with the spins being distributed into eigenstates following a Boltzmann distribution.

2.1.4 Chemical shift

The external magnetic field \vec{B}_0 will induce electronic currents which generate an induced magnetic field B_{CS} , which is three to six orders of magnitude lower than the applied field:

$$B_{CS} = \delta \cdot B_0 \quad (2.12)$$

where δ is a 3×3 matrix representing the chemical shift tensors with the following form:

$$\delta = \begin{bmatrix} \delta_{xx} & \delta_{xy} & \delta_{xz} \\ \delta_{yx} & \delta_{yy} & \delta_{yz} \\ \delta_{zx} & \delta_{zy} & \delta_{zz} \end{bmatrix} \quad (2.13)$$

In the principle axis system (PAS), this matrix will be transformed into:

$$\delta = \begin{bmatrix} \delta_{xx} & \delta_{xy} & \delta_{xz} \\ \delta_{yx} & \delta_{yy} & \delta_{yz} \\ \delta_{zx} & \delta_{zy} & \delta_{zz} \end{bmatrix} \xrightarrow{PAS} \delta_{PAS} = \begin{bmatrix} \delta_{XX} & 0 & 0 \\ 0 & \delta_{YY} & 0 \\ 0 & 0 & \delta_{ZZ} \end{bmatrix} \quad (2.14)$$

We have isotropic chemical shift defined as:

$$\delta_{iso} = \frac{1}{3} (\delta_{XX} + \delta_{YY} + \delta_{ZZ}) \quad (2.15)$$

Then the anisotropic part of the chemical shift tensor can be defined by:

$$\delta_{aniso} = \delta_{ZZ} - \delta_{iso} \quad (2.16)$$

using, as a convention:

$$|\delta_{ZZ} - \delta_{iso}| \geq |\delta_{YY} - \delta_{iso}| \geq |\delta_{XX} - \delta_{iso}| \quad (2.17)$$

The asymmetry parameter can be written as:

$$\eta = \frac{\delta_{YY} - \delta_{XX}}{\delta_{aniso}} \quad (2.18)$$

The Hamiltonian of chemical shift can be presented as:

$$\hat{\mathcal{H}}_{CS} = \gamma \hat{I} \cdot \delta B_0 \quad (2.19)$$

2.1.5 Dipolar interaction

Each spin can generate itself a magnetic field around itself, which in turn can affect the other neighboring spins. This interaction is usually called the through-space dipole-dipole or direct dipole-dipole coupling. [52]

In the homonuclear case, where the two interacting nuclear spins belong to the same isotopic species, the Hamiltonian is written as:

$$\hat{\mathcal{H}}_{D,II} = \frac{-\mu_0}{4\pi} \frac{\gamma_I^2 \hbar}{r^3} [A + B + C + D + E + F] \quad (2.20)$$

where

$$\begin{aligned}
A &= I_z^2 (3 \cos^2 \Theta - 1) \\
B &= -\frac{1}{4} [I_{1+} I_{2-} + I_{1-} I_{2+}] (3 \cos^2 \Theta - 1) \\
C &= -\frac{3}{2} [I_{1z} I_{2+} + I_{1+} I_{2z}] \sin \Theta \cos \Theta e^{-i\Theta} \\
D &= -\frac{3}{2} [I_{1z} I_{2-} + I_{1-} I_{2z}] \sin \Theta \cos \Theta e^{+i\Theta} \\
E &= -\frac{3}{4} [I_{1+} I_{2+}] \sin^2 \Theta e^{-2i\Theta} \\
F &= -\frac{3}{4} [I_{1-} I_{2-}] \sin^2 \Theta e^{+2i\Theta}
\end{aligned} \tag{2.21}$$

where $\mu_0 = 4\pi 10^{-7} \text{Hm}^{-1}$ is the magnetic constant, r is the distance between the two nuclei and Θ is the angle between \vec{r} and \vec{B}_0 .

2.1.6 Quadrupolar interaction

Quadrupolar spins ($I > 1/2$) undergo a quadrupolar interaction, which comes from the interaction between the electric quadrupolar moment and the electric field gradient at the nucleus.[55] The electric field gradient at the nuclear site can be presented as a tensor:

$$V = \begin{bmatrix} V_{xx} & V_{xy} & V_{xz} \\ V_{yx} & V_{yy} & V_{yz} \\ V_{zx} & V_{zy} & V_{zz} \end{bmatrix} \xrightarrow{PAS} V_{PAS} = \begin{bmatrix} V_{XX} & 0 & 0 \\ 0 & V_{YY} & 0 \\ 0 & 0 & V_{ZZ} \end{bmatrix} \tag{2.22}$$

And

$$V_{XX} + V_{YY} + V_{ZZ} = 0 \tag{2.23a}$$

$$|V_{YY}| < |V_{XX}| < |V_{ZZ}| \tag{2.23b}$$

η_Q is the quadrupolar parameter (or asymmetry parameter):

$$\eta_Q = \frac{V_{XX} - V_{YY}}{V_{ZZ}} \tag{2.24}$$

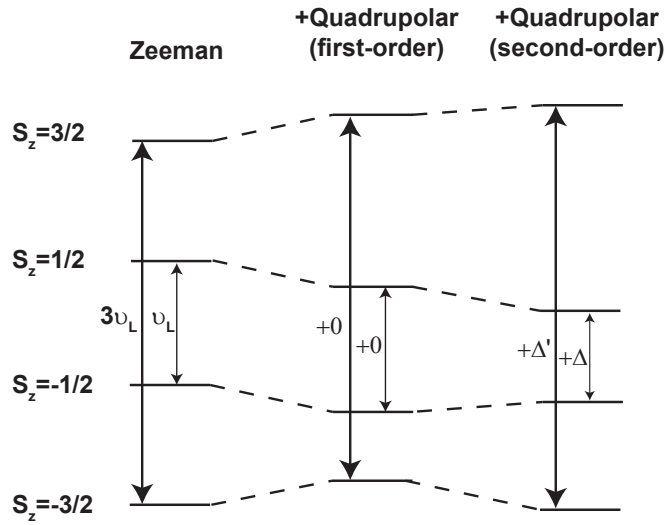


FIGURE 2.1: Energy diagram of a spin-3/2, showing the cumulative effects of first-and second-order quadrupolar effects when the Zeeman interaction is dominant. The arrows indicate the transitions between the $S_z = +m$ and $S_z = -m$ states, which are unaffected to first order by the quadrupolar Hamiltonian (adapted from ref [56])

The Hamiltonian of the quadrupolar interaction can be written as:

$$\hat{\mathcal{H}}_Q = \frac{eV_{ZZ}Q}{4I(2I-1)\hbar} \left[3\hat{I}_Z^2 - I(I+1) + \frac{1}{2}\eta_Q (\hat{I}_X^2 - \hat{I}_Y^2) \right] \quad (2.25)$$

where Q is the quadrupolar moment of the nuclear spin. The quadrupole coupling constant C_Q is defined by:

$$C_Q = \frac{eV_{ZZ}Q}{h} \quad (2.26)$$

Figure 2.1 [56] shows the energy level diagram of a spin-3/2 including the Zeeman, first-and second order quadrupolar interactions. In our case, the quadrupolar interaction for ${}^7\text{Li}$ is very small, and we can neglect the second-order quadrupolar interaction.

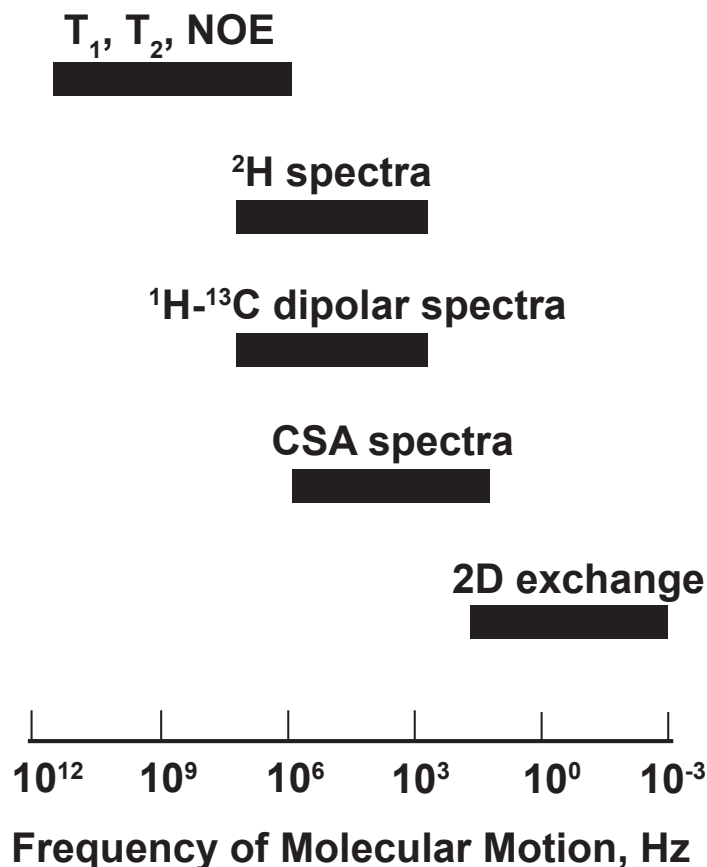


FIGURE 2.2: Frequencies of the molecular motion detectable by NMR spectroscopy (adapted from ref [58])

2.2 Relaxation of nuclear spins to study molecular motion

NMR experiments not only give structural information with atomic resolution, but also can characterize the amplitude and time scales of motions over broad ranges of length and time.[57] Relaxation time measurements have long been used to characterize molecular motions in solids.[55] Figure 2.2 shows the range of frequencies for molecular motions which can be detected by NMR. [58] In this thesis, we will focus on analyzing the relaxation times T_1 and T_2 of ^7Li nuclei.

The measurements of T_1 and T_2 we performed at various temperatures or different magnetic fields can help to characterize the fast dynamics in the nanosecond to microsecond range.[59] The next two parts describe how longitudinal and transverse relaxation times are measured.

2.2.1 Longitudinal relaxation time T_1

When one applies a RF (radio frequency) pulse on a spin system under a magnetic field, it will put the spin system into a thermodynamically unstable state. The longitudinal relaxation time T_1 is the characteristic time a spin system takes to return to the equilibrium Boltzmann distribution of the populations. For a mono-exponential relaxation behaviour, the evolution of magnetization after its saturation by a train of RF pulses is given by:

$$M_z(t) = M_z(0) \left[1 - \exp\left(\frac{-t}{T_1}\right) \right] \quad (2.27)$$

where $M_z(t)$ is the nuclear spin magnetization at time t , $M_z(0)$ is the nuclear spin magnetization at equilibrium. The pulse sequence used is a saturation recovery sequence, where the saturation pulse train (8 to 16 pulses, separated by delays between 1 to 10 ms) is followed by a variable relaxation delay (t) and a $\pi/2$ "read" pulse which converts the relaxed magnetization into a detectable signal. The relaxation rate is simply defined by $R_1 = 1/T_1$. For quadrupolar spins, a consequence of their quadrupolar nature (as opposed to differences in the populations/environments) longitudinal relaxation is biexponential [60] and can be fitted by using the equation:

$$\frac{M_z(t)}{M_z(0)} = \left[1 - \frac{1}{5} \exp\left(\frac{-t}{T_{1,\text{fast}}}\right) - \frac{4}{5} \exp\left(\frac{-t}{T_{1,\text{slow}}}\right) \right] \quad (2.28)$$

However, if the difference between the two relaxation rates is small, usually, an effective relaxation rates is measured and used in the calculations:

$$\frac{M_z(t)}{M_z(0)} = \left[1 - \exp\left(\frac{-t}{T_{1,\text{eff}}}\right) \right] \quad (2.29)$$

2.2.2 Transverse relaxation time T_2

After a perfect $\pi/2$ pulse, all spins are aligned in xy plane. The dephasing which is caused by the sample's inhomogeneity is prevented by the application of a refocusing π pulse in the middle of the variable relaxation delay t (Hahn echo sequence). The decay of the magnetization in the xy plan during the echo time t is characterized by the transversal relaxation time T_2 . The equation describing

mono-exponential transverse relaxation is:

$$M_{xy}(t) = M_{xy}(0) \exp\left(\frac{-t}{T_2}\right) \quad (2.30)$$

For quadrupolar spins, the relaxation curve is also biexponential:[60]

$$\frac{M_{xy}(t)}{M_{xy}(0)} = \left[\frac{3}{5} \exp\left(\frac{-t}{T_{2,\text{fast}}}\right) + \frac{2}{5} \exp\left(\frac{-t}{T_{2,\text{slow}}}\right) \right] \quad (2.31)$$

provided no residual quadrupolar interaction is present. As no splitting is observed in our samples, we consider that no residual quadrupolar interaction is ever observed in our samples. Similar to the case of longitudinal relaxation above, if two transverse relaxation rates are close to each others, we have:

$$\frac{M_{xy}(t)}{M_{xy}(0)} = \exp\left(\frac{-t}{T_{2,\text{eff}}}\right) \quad (2.32)$$

2.2.3 Molecular vibrations

The different types of motions which are relevant to the NMR experiments are described in Levitt's book.[52] We will briefly present about them. First, very fast motions must be taken into account. This type of motion comes from the nuclei which vibrates rapidly in their mean positions. The timescale of this motion is in the range of 10^{-12} s (10^{12} Hz), thus it cannot be detected by relaxation experiments (see figure 2.2) and the NMR Hamiltonians are effectively averaged over this timescale.

2.2.4 Molecular flexibility

This motion comes from the internal flexibility (rotations around chemical bonds, etc...) like in proteins or polymers. In our case, we studied PEO which is a flexible polymer. The timescale of these motions can be short (picoseconds) to much longer (seconds) when restraints to the motion are present.

2.2.5 Molecular rotations

This type of motion comes from the rotational diffusion of molecules which can be detected by modulations in the CSA, direct dipole-dipole or quadrupolar interactions. In most case, the timescale lies in the range of picoseconds (10^{-12} s for small molecules) to nanosecond (10^{-9} s for larger molecules) or 10^{12} to 10^9 Hz, so that it can be detected by relaxation experiments.

It is very valuable to mention translational motion (the motion of the molecular mass center through space) which is also detected by NMR. This type of motion cannot be detected by relaxation experiments because its timescale is in microseconds. To measure this motion, in this thesis, we used the method of pulse field gradients (PFG) which is presented later.

2.3 How to study molecular motions with relaxation times

2.3.1 Angular dependent NMR interactions

As discussed above, the molecular motions can take place in a wide range of timescale. The NMR interactions can detect the geometry and timescales of molecular motions via isotropic and anisotropic nuclear spin interactions [57]. The relaxation processes characterized by T_1 , T_2 are dominated by the NMR interactions mentioned above. In other words, we understand the NMR interactions so we can back-calculate the characteristics of molecular motions. In a recent paper, Hansen et al. [57] have revisited the coupling between molecular motion and the NMR interactions.

The general equation which describes the orientation-dependence of NMR interactions can take the following form: [57, 61]

$$\omega(\theta_\lambda, \phi_\lambda) - \omega_L = \omega_{iso} + \frac{\Delta_\lambda}{2} (3 \cos^2 \theta_\lambda - 1 - \mu_\lambda \sin^2 \theta_\lambda \cos 2\phi_\lambda) \quad (2.33)$$

where ω_L is Larmor frequency, ω_{iso} is the isotropic frequency component. Δ_λ , μ_λ are asymmetry parameters, describing the deviation of axial system. The subscript

λ describes the nature of the NMR interaction (CSA, dipole-dipole, quadrupolar coupling). θ_λ , ϕ_λ denote the polar angles of the interaction PAS with respect to external magnetic field.

Here, we should introduce an important concept: the order parameter. This parameter is the scaling factor of an interaction resulting from its averaging during a given timescale. If the magnitude of the interaction does not fluctuate, during this time, the tensor is distributed over an ensemble of thermally accessible orientations defined by θ [62]. The order parameter S^2 associated with this averaging process can be written as:

$$S^2 \approx 1 - 3 \langle \theta^2 \rangle \quad (2.34)$$

2.3.2 Auto-correlation functions

If the Hamiltonian fluctuates, the solution to the Liouville-von Neumann will be found by using a perturbation treatment as shown in equation 2.4: [63]

$$\frac{d\bar{\hat{\rho}}}{dt} = -i \left[\bar{\hat{\mathcal{H}}}, \bar{\hat{\rho}}(0) \right] - \int_0^t \left[\bar{\hat{\mathcal{H}}}(t), \left[\bar{\hat{\mathcal{H}}}(t'), \bar{\hat{\rho}}(t') \right] \right] dt' \quad (2.35)$$

where $\hat{\rho}_0$ is the thermal equilibrium of $\hat{\rho}$.

Now, we will treat the Hamiltonian in form of spherical tensors which allows a clear distinction between the time-dependent spin matrix elements and the time-dependent spatial matrix elements. [64] The Hamiltonian in the laboratory frame is given by:

$$\hat{\mathcal{H}}(t) = \sum_{\alpha} F_{\alpha}(t) T_{\alpha} \quad (2.36)$$

where T_{α} ($\alpha = \{k, l, \lambda\}$) are the irreducible spherical tensor operators (acting on the spin coordinates) of rank k and order l and λ denotes the type of interaction.

The ranks of irreducible spherical tensors T_{α} concern different interactions:

- Rank k=1: The spin-rotation and chemical shift anisotropy interactions
- Rank k=2: The dipolar and quadrupolar interactions

F_α is the spatial part of the Hamiltonian interaction (linked to the orientation of the interaction tensor in the laboratory frame): $F_\alpha(\Omega(t)) = F_\alpha(\theta(t), \phi(t))$

As equation 2.35 is developed, one can extract the spin parts from the integral, and compute the integrals of products of the spatial parts $\mathcal{J}_{\alpha,\alpha'}(\omega)$:

Using this representation of the Hamiltonian, equation 2.35 will become:

$$\begin{aligned} \frac{d}{dt}\hat{\rho}(t) &= -i [\hat{\mathcal{H}}_0, \hat{\rho}(t)] \\ &\quad - \sum_{\alpha,\alpha'} \mathcal{J}_{\alpha,\alpha'}(\omega) [T_\alpha, [T_{\alpha'}, (\rho(t) - \rho_0)]] \end{aligned} \quad (2.37)$$

The spectral densities $\mathcal{J}_{\alpha,\alpha'}(\omega)$ are the Fourier transforms of the correlation functions, which express the correlation over time of the F_α functions with each other. It can be written as: [53]

$$\mathcal{G}_{\alpha\alpha'}(|t - t'|) = \langle F_\alpha(\Omega(t)) F_{\alpha'}(\Omega(t')) \rangle \quad (2.38)$$

where bra-ket notation is to show an ensemble or time average and $(|t - t'|) = \tau$.

The Fourier transform of this correlation function transforms the time-dependent $\mathcal{G}_{\alpha\alpha'}(\tau)$ function into a frequency-dependent function $\mathcal{J}_{\alpha\alpha'}(\omega)$:

$$\mathcal{J}_{\alpha\alpha'}(\omega) = \int_0^\infty \mathcal{G}_{\alpha\alpha'}(\tau) \exp(i\omega\tau) d\tau \quad (2.39)$$

which is called the spectra density.

For quadrupolar relaxation, the first order quadrupolar Hamiltonian is reduced to only one term $H_Q = C_Q F_{2,0}(t) T_{2,0}$, and cross-correlations with the much weaker dipolar interactions will be neglected. Neglecting the effect of dipolar relaxation is justified by the relative sizes of the interactions (tens of kHz for the quadrupolar coupling, compared to 1.7 kHz for the dipolar interaction between ^7Li and ^1H if they are 3 Å apart), and second we lack the necessary data to compute an extensive model which would require many parameters. The only option would be to use atomic trajectories from molecular dynamics simulations over sufficient timescales to see if NMR relaxation parameters can be reproduced. Therefore, one has to compute:

$$G_\alpha(\tau) = \frac{\langle F_\alpha(\Omega(t)) F_\alpha(\Omega(t')) \rangle}{\langle F_\alpha^2(\Omega(t)) \rangle} \quad (2.40)$$

where $\langle F_\alpha^2(\Omega(t)) \rangle$ is the mean square of $F_\alpha(\Omega(t))$. Simple models of the correlation functions usually consider it to be a mono-exponential decay with a time constant τ_c . More generally, the correlation time τ_c expresses the time constant of the decay of the reduced auto-correlation function, $G_\alpha(\tau)$, which can be defined as:

$$\tau_\alpha = \int_0^\infty G_\alpha(t) dt \quad (2.41)$$

Equation 2.39 can be written as:

$$\mathcal{J}_\alpha(\omega) = \langle F_\alpha^2(\Omega(t)) \rangle J_\alpha(\omega) \quad (2.42)$$

where $J_\alpha(\omega)$ is the reduced spectra density. We will focus on determining the reduced spectra density from our relaxation data.

2.3.3 Determination of the spectral density

A nuclear spin relaxation rate R form can be written as:[64]

$$R(\omega_j, x_i) = \mathcal{A}q(\omega_j, x_i) \quad (2.43)$$

where \mathcal{A} represents the spin interactions.

The $q(\omega_j, x_i)$ function can be written as:

$$q(\omega_j, x_i) = \sum_j n_j J(\omega_j, x_i) \quad (2.44)$$

where ω_j is a set of frequencies, x_i is a set of parameters characterizing the dynamical processes involved.

From equation 2.42, equation 2.43 and equation 2.44 we can see the relationship between relaxation rates, NMR interactions and molecular dynamics.

2.3.4 Spectral densities

Here, we present some spectral densities which are used frequently in fitting relaxation times.

2.3.4.1 Bloembergen-Purcell-Pound (BPP) model

We started by analyzing the relaxation times T_1 and T_2 by the common Bloembergen-Purcell-Pound (BPP) model [65–67], in which the correlation function is a single exponential decay (i.e. one physical process, such as in the rotational diffusion of a rigid molecule).

The spectral density is then given by:

$$J_n = \frac{\tau_c}{1 + n^2\omega^2\tau_c^2} \quad (2.45)$$

2.3.4.2 Cole-Davidson function

An other model was also tried, the so-called Cole-Davidson function:

$$J_n = \frac{2 \sin(\beta \arctan(\omega\tau_c))}{\omega [1 + (n^2\omega^2\tau_c^2)^{\beta/2}]} \quad (2.46)$$

where $\beta(0 \leq \beta \leq 1)$ describes the deviation from exponentiality. This function originates from spectral density function used in dielectric relaxation.[68] The Davidson-Cole spectral density is the most successful one used to interpret nuclear spin relaxation experiments in solids.[64]

This function takes into account the distribution of motional barriers to correlated motion like other models based on dielectric relaxation.

2.3.4.3 Lipari-Szabo model

This model-free approach is based on combining the effects of internal motion $-C_I(t)-$ in molecules, which lead to partial averaging of the interactions, and of the overall rotational motion $-C_O(t)-$ which averages the interactions over a longer timescale.[69, 70]. For the case of isotropic overall motion, the total correlation function is given by:

$$C(t) = C_O(t) C_I(t) \quad (2.47)$$

The internal correlation function is given by:

$$C_I(t) = \langle P_2(\hat{\mu}(0) \cdot \hat{\mu}(t)) \rangle = (1 - S^2)e^{-t/\tau_I} + S^2 \quad (2.48)$$

where the unit vector $\hat{\mu}$ describes the orientation of the interaction vector (or tensor) in a reference frame and S^2 describes the partial averaging of the interaction by this internal correlation function. The overall correlation function $C_O(t)$ can be defined in the case of isotropic or anisotropic motion, which is fully described in reference. [70] In the case of isotropic molecules:

$$C_O(t) = e^{-t/\tau_O} \quad (2.49)$$

The spectral density is given by:

$$J(\omega) = \frac{2}{5} \left[\frac{S^2 \tau_O}{1 + \omega^2 \tau_O} + \frac{(1 - S^2) \tau_e}{1 + \omega^2 \tau_e^2} \right] \quad (2.50)$$

where τ_O is the overall correlation time and τ_e is defined as:

$$\frac{1}{\tau_e} = \frac{1}{\tau_O} + \frac{1}{\tau_I} \quad (2.51)$$

2.4 Diffusion

Diffusion is a phenomena, in which the molecules or small particles move randomly due to the motion caused by thermal energy.[71] It is a transportation process of particles in order to equalize the concentration in a whole system. The particles will move from the high concentration places to low ones. Diffusion is a very important process as it describes the mobility of each species (such as lithium from one electrode to the other). This process can be presented by a specific parameter D , called the diffusion coefficient with general unit in SI [m²/s]. Often, D may follow an Arrhenius' law:

$$D = D_0 \exp(-E_a/k_B T) \quad (2.52)$$

whereas E_a is the activation energy, k_B is Boltzmann's constant, T is the absolute temperature, D_0 is the diffusion coefficient at infinite temperature.

2.4.1 Fick's laws

The Fick's laws are used to describe the diffusion process. We will consider only the one-dimension diffusion. The engine of the diffusion process is the concentration's gradient. The movement of species is time and place-dependent; hence the concentration is a function of the position and time t .

$$C = f(x, t) \quad (2.53)$$

One can define the flux of diffusion $J = \frac{\partial n}{S \partial t}$, where ∂n is the quantity of moving species and S is the area perpendicular with the direction of diffusion. The first Fick's law describes the flux of one type of species (atoms, small particles etc...):

$$J = \frac{\partial n}{S \partial t} = -D \frac{\partial C}{\partial x} = -D \nabla C \quad (2.54)$$

where D is the diffusion coefficient (or the speed of diffusion when the gradient of concentration is equal to unity). The sign '-' indicates that the flux J occurs in the opposite direction of the concentration gradient (i.e. towards zones of lower concentrations) and D is positive. The diffusion coefficient is expressed in $[\text{cm}^2/\text{s}]$ or $[\text{m}^2/\text{s}]$.

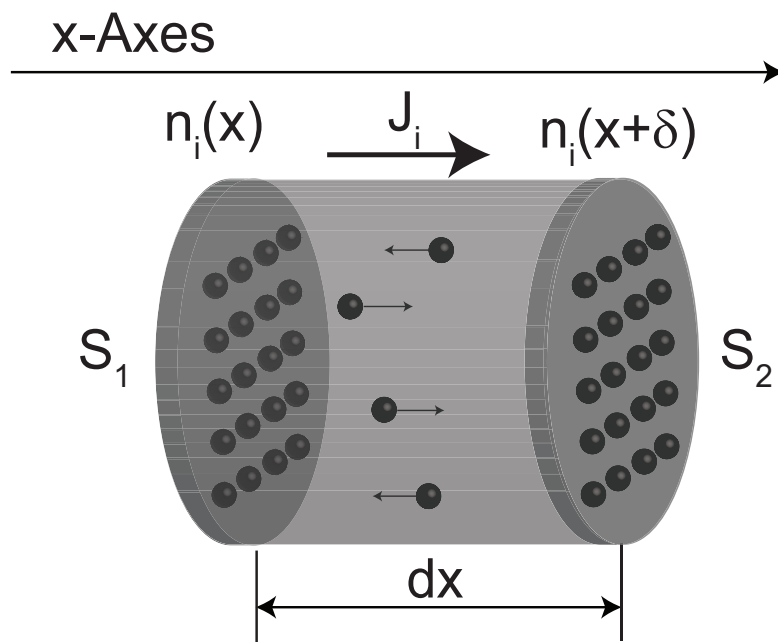


FIGURE 2.3: Model of Fick's laws

The second Fick's law is an expression of the law of conservation of matter:

$$\frac{\partial C}{\partial t} + \nabla \cdot J = 0 \quad (2.55)$$

Combining with equation 2.54, we have:

$$\frac{\partial C}{\partial t} = \nabla \cdot (D \nabla C) = D \frac{\partial^2 C}{\partial x^2} \quad (2.56)$$

for a one-dimensional problem.

2.4.2 Self-Diffusion

2.4.2.1 Introduction

Self-diffusion is the transportation process without any chemical potential gradient, describing the uncorrelated movement of a particle. [72]

Figure. 2.3 explains how Fick's laws are derived. The time it takes for the i species to go from x to $x + \delta$ is τ (or the rate $1/\tau$). The probability for the i species to go to the left or to the right are equal. The flux of i species that move across the S plane is given by:

$$J_i = - \left[\frac{n(x + \delta, t)}{\tau} - \frac{n(x, t)}{\tau} \right] \quad (2.57)$$

Since

$$C(x, t) = \frac{n(x + \delta, t)}{S\delta} \quad (2.58)$$

Therefore

$$C(x, t) - C(x + \delta, t) = -\delta \frac{\partial C}{\partial x} \quad (2.59)$$

From equation 2.57 and equation 2.58, we have:

$$J = -\frac{\delta^2}{\tau} \frac{\partial C}{\partial x} \quad (2.60)$$

Combining this with the first Fick's law equation 2.54, we can derive the diffusion coefficient in one-dimension:

$$D = \frac{\delta^2}{\tau} \quad (2.61)$$

2.4.2.2 Stokes-Einstein equation

To explain Brownian motion, Einstein applied Stokes' law to the diffusion of species with Stokes drag $\zeta = 6\pi\eta R$, and found the self-diffusion coefficient:

$$D = \frac{k_B T}{\zeta} \quad (2.62)$$

This equation is also called Sunderland-Einstein equation.

2.4.2.3 Random walk theory

Now, we consider N species moving like in figure 2.3 with same velocity $v = \sqrt{k_B T/m}$, whereas k_B is Boltzmann's constant, m is the mass of the considered species. The distance between the position of the species from their origins after n jumps is:

$$\langle x \rangle = \frac{\sum_j x(j)}{j} \quad (2.63)$$

Because the probabilities of jumps to the left and to the right are equal (half-half), the average distance will be $\langle x \rangle = 0$. To quantify the random walk movement, we will focus on the mean square distance $\langle x^2 \rangle$, which is the characteristic of a random walk:

$$\langle x^2 \rangle = \frac{\sum_j [x(j)]^2}{j} \quad (2.64)$$

The magnitude of $\langle x^2 \rangle$ is proportional to n jumps, and the time t :

$$\begin{aligned} \langle x^2 \rangle &\propto n, \\ \langle x^2 \rangle &\propto t \end{aligned} \quad (2.65)$$

Now, we consider Figure. 2.3. The transit plane is in the middle between S_1 and S_2 , with the distance between each one is $\sqrt{\langle x^2 \rangle}$. The concentration of region between S and S_1 is C_1 , between S and S_2 is C_2 . The diffusion flux of species across the transit plane (or the net number of moles of species crossing through the unit area of the transit plane per second from the left to the right) is given by:

$$J = \frac{1}{2} \frac{\sqrt{\langle x^2 \rangle}}{t} (C_1 - C_2) \quad (2.66)$$

Since

$$C_1 - C_2 = -\sqrt{\langle x^2 \rangle} \frac{dc}{dx} \quad (2.67)$$

The equation 2.66 can be given:

$$J = -\frac{1}{2} \frac{\sqrt{\langle x^2 \rangle}}{t} \frac{dc}{dx} \quad (2.68)$$

In comparing with first Fick's law equation 2.54:

$$D = \frac{\sqrt{\langle x^2 \rangle}}{2t} \text{ or } \sqrt{\langle x^2 \rangle} = 2Dt \quad (2.69)$$

Eq. 2.69 is also called the Einstein-Smoluchowski equation. It presents the microscopic approach to diffusion. In two and three-dimensions, equation 2.69 transforms into $\sqrt{\langle r^2 \rangle} = 4Dt$ and $\sqrt{\langle r^2 \rangle} = 6Dt$, respectively.

2.4.2.4 Diffusion propagators

We consider the three-dimensional case with free isotropic diffusion, the propagator is a function of the displacement but is independent of the initial position. $P(r_0, r_1, t)$ is the conditional probability of finding a particle initially in r_0 , and in r_1 after a time t . $P(r_0, r_1, t)$ follows the normalization condition:

$$\int P(r_0, r_1, t) dr_1 = 1 \quad (2.70)$$

The equilibrium particle density is given by:

$$\rho(r_0) = \int \lim_{t \rightarrow \infty} P(r_0, r_1, t) dr_1 \quad (2.71)$$

and $\int \rho(r_0) dr_0 = 1$. The total probability $P(r_1, t)$ of finding a species at position r_1 at time t will be given by:

$$P(r_1, t) = \int \rho(r_0) P(r_0, r_1, t) dr_0 \quad (2.72)$$

A detailed description can be found in.[73] Replacing C by $P(r_0, r_1, t)$, the initial condition can be written in the following form:

$$P(r_0, r_1, 0) = \delta(r_1 - r_0) \quad (2.73)$$

where δ is the Dirac delta function. Then, equation 2.56 will become:

$$\frac{\partial P(r_0, r_1, t)}{\partial t} = D\nabla^2 P(r_0, r_1, t) \quad (2.74)$$

Eq. 2.74 has the following solution:

$$P(r_0, r_1, t) = (4\pi Dt)^{-3/2} \exp\left[-\frac{(r_1 - r_0)^2}{4Dt}\right] \quad (2.75)$$

2.4.3 Conductivity and diffusion

In this thesis, we focused on the materials used in battery systems. Therefore, the connection between conductivity and diffusion is worth mentioning. The equations were adapted from Modern Electrochemistry, vol 1. [74]

2.4.3.1 Mobility of Ions

Under an electric field, the random walk of ions becomes non-random. The ions move in the direction dragged by the force \vec{F} with a drift velocity v_d :

$$v_d = \frac{dv}{dt}\tau = \frac{\vec{F}}{m}\tau \quad (2.76)$$

and τ is the time between ionic jumps. The absolute mobility is defined by:

$$\bar{u}_{abs} = \frac{\tau}{m} = \frac{v_d}{\vec{F}} \quad (2.77)$$

The absolute mobility \bar{u}_{abs} is the measure of drift velocity v_d of ionic species under force \vec{F} . The conventional (electrochemical) mobility is defined by:

$$u_{conv} = \bar{u}_{abs} z_i e_0 \quad (2.78)$$

whereas $z_i e_0$ is the charge of ion.

2.4.3.2 Nernst-Einstein equation

The molar ionic conductivity of a solution containing a $z : z$ valent electrolyte is given by:

$$\Lambda = F \left[(u_{conv})_+ + (u_{conv})_- \right] \quad (2.79)$$

where F is the Faraday constant. Combining Einstein relation $D = \bar{u}_{abs} kT$ with equation 2.78, and replacing u_{conv} , we have:

$$\Lambda = \frac{ze_0 F}{kT} (D_+ + D_-) \quad (2.80)$$

This shows the direct relationship between conductivity and the sum of the self-diffusion coefficients.

The ionic transport number (or transference number) is an important parameter, describing the contribution of an ion to the overall conductivity. The ionic transport number the cation t_+ can be defined as:

$$t_+ = \frac{u_+}{u_+ + u_-} = \frac{D_+}{D_+ + D_-} \quad (2.81)$$

Hence, the transport numbers are related by: $t_- = 1 - t_+$. In lithium batteries, the cation transport number is of particular concern. A cation transport number of one is expected to overcome the problems stemming from concentration gradients. [75]

2.4.4 Diffusion coefficient measurements by NMR

In this thesis, we used the NMR method called "Pulsed Field Gradient" (PFG) to measure the self-diffusion coefficients of spin bearing species. This is a noninvasive method which is selective for nucleus of interest. [76]

A magnetic field gradient can be produced by a coil such as anti-Helmholtz or Golay pairs of coils. When a magnetic field gradient \mathbf{G} (T/m) is applied, where the additional field is parallel to B_0 , it can be defined by: [77]

$$\mathbf{G} = \nabla B_z = \frac{\partial B_z}{\partial x} \mathbf{i} + \frac{\partial B_z}{\partial y} \mathbf{j} + \frac{\partial B_z}{\partial z} \mathbf{k} \quad (2.82)$$

where $\mathbf{i}, \mathbf{j}, \mathbf{k}$ are unit vectors of the laboratory frame of reference. The precession frequency of a nuclear spin will be modified:

$$\omega(\mathbf{r}) = \omega_0 + \gamma(\mathbf{G} \cdot \mathbf{r}) \quad (2.83)$$

We now consider the case of the magnetic field gradient is aligned with the z direction, the magnitude of \mathbf{G} will be: $G = \mathbf{G} \cdot \mathbf{k} = \frac{\partial B_z}{\partial z}$.

In the case of single quantum coherences, the cumulative phase shift experienced by a nucleus in $z(t)$ is given by:

$$\phi(t) = \gamma B_0 t + \gamma \int_0^t G(t') z(t') dt' \quad (2.84)$$

the term $\gamma \int_0^t G(t') z(t') dt'$ is the result of the applied gradient. Eq. 2.84 shows the dependence of the dephasing with the strength of the field gradient $G(t)$ (pulsed gradients have varying intensities), the duration t during which it is applied (otherwise the field is homogeneous and no gradient is present), and the position $z(t)$ of the spin along the direction of the gradient.

The Hahn echo sequence [79] is used to measure diffusion coefficient by applying the magnetic field gradient see Figure 2.4. The signal attenuation can be calculated as:

$$S(2\tau) = S(0) \exp\left(-\frac{2\tau}{T_2}\right) f(\delta, G, \Delta, D) \quad (2.85)$$

The term of $\exp\left(-\frac{2\tau}{T_2}\right)$ expresses the attenuation due to relaxation. The function $f(\delta, G, \Delta, D)$ expresses the attenuation due to diffusion: as the diffusing species are not in the same place after Δ , they do not experience the same gradient-induced phase shifts, and therefore the magnetization is not refocused.

To eliminate the former term, we can perform several experiments with constant Δ values and varying gradient strengths G . We then need to measure the following quantity:

$$E = \frac{S(2\tau)}{S(2\tau)_{g=0}} = f(\delta, G, \Delta, D) \quad (2.86)$$

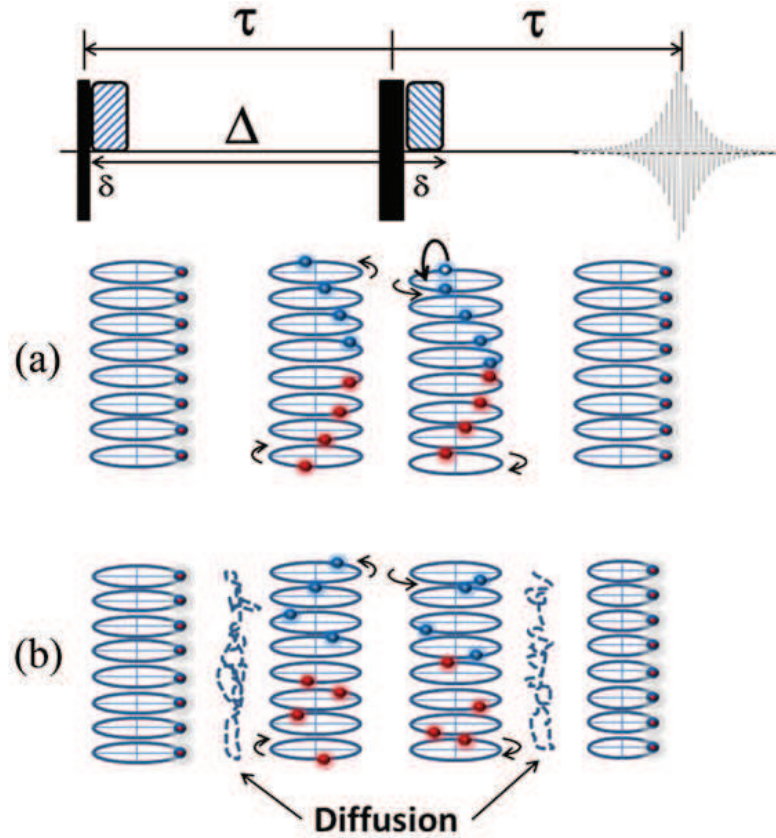


FIGURE 2.4: The Hahn spin-echo used to measure the diffusion coefficient. In (a), no diffusion means that the magnetizations of each slice in the sample along z are refocused at the end. In (b), the random motion of spins implies that they do not experience the same dephasing during the first and second gradient, and therefore, the signal is incompletely refocused (adapted from ref [78])

The determination of the f function will lead to the diffusion coefficient D . Using equation 2.75, for the standard spin-echo sequence, the expression of f is:

$$f(\delta, G, \Delta, D) = \exp \left[-D\gamma^2 g^2 \delta^2 \left(\Delta - \frac{\delta}{3} \right) \right] \quad (2.87)$$

In our case, the measurement of the diffusion coefficient was made with a gradient applied along the MAS axis (see Figure 2.5), implying that MAS does not modulate the gradient experienced by each spin. Such a gradient is created by applying three gradients of equal strengths along the x , y and z axis. Diffusion is measured along the MAS axis in this case.

In this thesis, we used the bipolar-gradient pulses which reduce the effects of inhomogeneous background gradients and of eddy-currents.[81] As in our samples

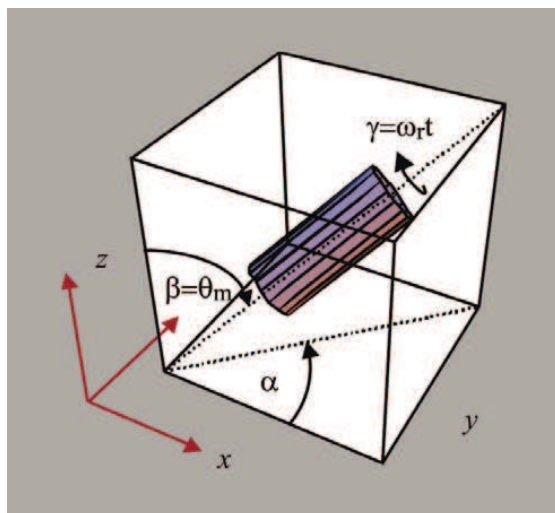


FIGURE 2.5: Magic Angle Spinning: rotating the sample around the diagonal of the cube exchange the x , y and z axis for each crystallite and therefore averages the anisotropic interactions. The three Euler angles α , β , γ describe the coordinate transformation from the MAS rotor frame to the laboratory frame where $\beta = \theta_m$ (magic angle), $\gamma = \omega_r t$ (ω_r is the speed of rotation about the rotor axis)(adapted from ref [80])

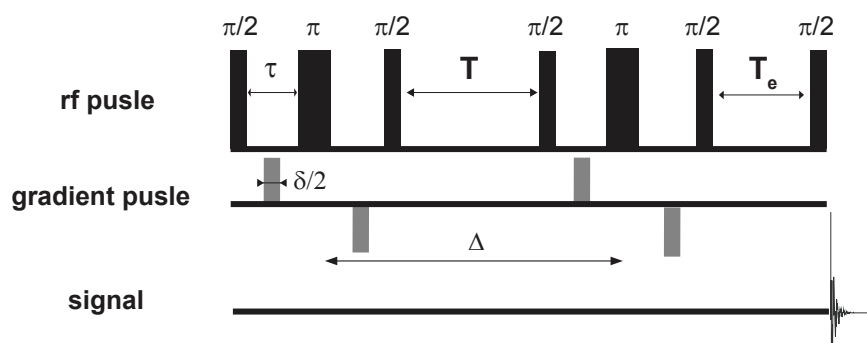


FIGURE 2.6: Stimulated echo-bipolar gradient pulse sequence used to measure the diffusion coefficient

$T_2 < T_1$, the magnetization was stored along z during Δ , as in the stimulated echo sequence.

Figure 2.6 shows the pulse sequence that we used to measure the diffusion coefficient in this thesis. The f attenuation function is similar. To retrieve the diffusion coefficient, several experiments are recorded, with varying gradient intensities, keeping δ and Δ constant. An example is shown below, in figure 2.7.

The measurements were performed on a 17.6 T wide-bore Avance HD Bruker spectrometer, using a three axes Micro 2.5 G/A/cm gradient system coupled to 40 A amplifiers, therefore able to achieve a maximum 160 G/cm gradient with a 3.2

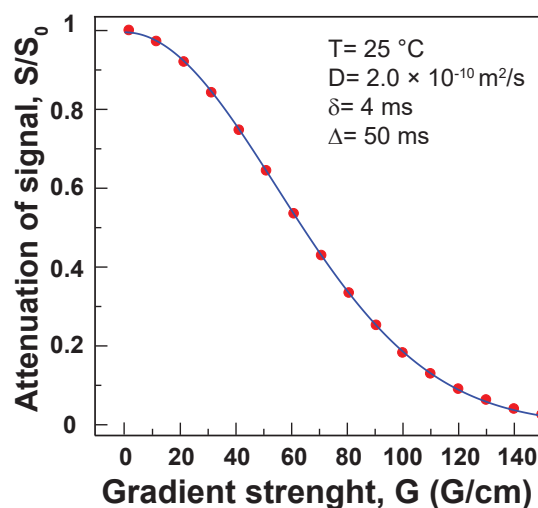


FIGURE 2.7: Fitting the diffusion coefficient of Li⁺ in 1M LiPF₆ in EC:DMC 1:1.

mm Magic Angle Spinning (MAS), ¹H-¹⁹F / ³¹P-¹⁴N double resonance probe. To ensure that experimental errors can be neglected, the measurements were repeated several times and the presented results are averaged.

Chapter 3

The Effect of Magic Angle Spinning on Relaxation and Diffusion

3.1 Magic angle spinning

Magic angle spinning is a technique used to reduce inhomogeneous magnetic susceptibility effects [80] and anisotropic spin interactions such as CSA, dipolar coupling and quadrupolar coupling (first order). This technique is usually used in solid-state NMR. The spinning axis is inclined at the magic angle (54.74°) with respect to the magnetic field B_0 , see figure 3.1.

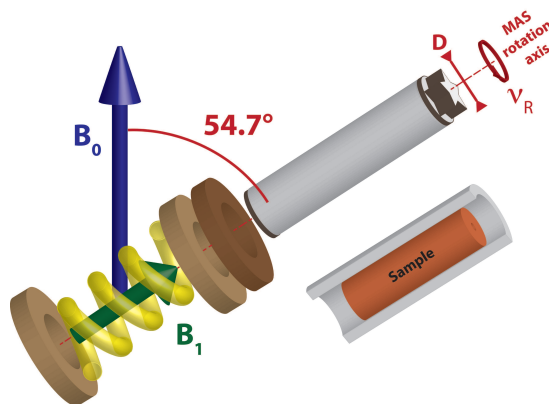


FIGURE 3.1: Magic angle spinning of a rotor

If the spinning frequency is high enough, the high-resolution isotropic NMR spectrum is obtained. Furthermore, small signals can become visible as narrower peaks are easier to detect. [82] It should be mentioned that reducing the interactions stated above can lead to an increase of T_2 which limits the gradient pulse length δ .

3.2 Temperature calibration

When the sample is rotated, friction forces tend to heat the rotor and the temperature inside the rotor rises. Therefore, a proper monitoring of the temperature is necessary. The temperature calibration for MAS spinning rates between 2 and 10 kHz with $\text{Pb}(\text{NO}_3)_2$. [83] To calculate the temperature inside the rotor, we used the relationship between ^{207}Pb chemical shift δ_{CS} and temperature: [83]

$$T (\text{°C}) = \frac{\delta_{CS} (\text{ppm})}{0.753 (\text{ppm/°C})} \quad (3.1)$$

This equation works in the temperature range between -130 and +150 °C.

The temperature calibration under static conditions was done with ethylene glycol (EG). [84] The relationship between the difference of the ^1H chemical shifts of the two peaks ($\Delta\delta_{CS}$) and temperature is:

$$T (\text{K}) = 466.5 - 102.00 \times \Delta\delta (\text{ppm}) \quad (3.2)$$

This equation works in the temperature range between 273 and 416 K (or between 0 and +143 °C).

3.3 Observation

The comparison of the ^7Li spectra with different MAS rates is shown in figure 3.2. The ^7Li static spectrum can be fitted by two Lorentzian components (at the same position), as expected from its quadrupolar nature. Table 3.1 shows the linewidth of ^7Li -NMR spectra in figure 3.2. Clearly, under MAS, the linewidth of the ^7Li spectrum becomes narrower than under static conditions. This shows that a clear gain in sensitivity is obtained by MAS, allowing a significant gain in experimental

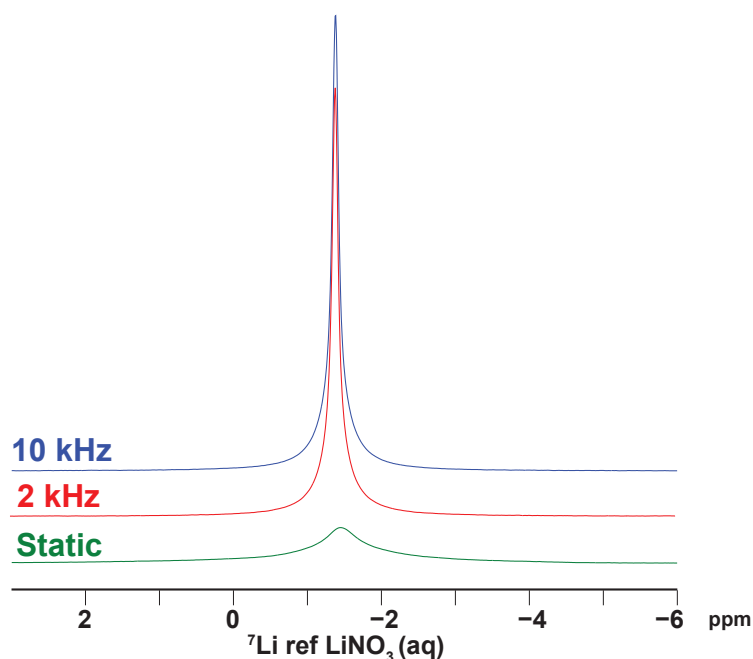


FIGURE 3.2: ${}^7\text{Li}$ NMR spectrum of PEO(LiTFSI) with different MAS rates at 35 °C.

time, especially at lower temperatures, where the lines are broadened by residual interactions. Interestingly, the linewidth is more or less the same under 2 kHz and 10 kHz MAS, as most residual interactions (quadrupolar, dipolar, susceptibility) are quickly averaged by MAS.

TABLE 3.1: The linewidths (in Hz) extracted from the ${}^7\text{Li}$ -NMR spectra of PEO(LiTFSI) in figure 3.2

	1 st component	2 nd component
Static	150.70	626.40
2 kHz	27.30	150.25
10 kHz	29.00	171.90

The experiments were performed also at higher temperatures up to 97 °C where PEO(LiTFSI) is melted.

After our experiments at a 10 kHz MAS rate, we stored the sample in the glove box. After one week, we ran a ${}^1\text{H}$ -NMR spectrum, as seen in figure 3.3. The lineshape of the ${}^1\text{H}$ -NMR spectrum is clearly changed upon spinning, and the splitting does not disappear quickly after spinning the sample. The same splitting is also detected in the ${}^7\text{Li}$ and ${}^{19}\text{F}$ NMR spectra, as seen in figure 3.4, and the lineshapes can be superimposed to each other if the scale is in ppm. Two questions

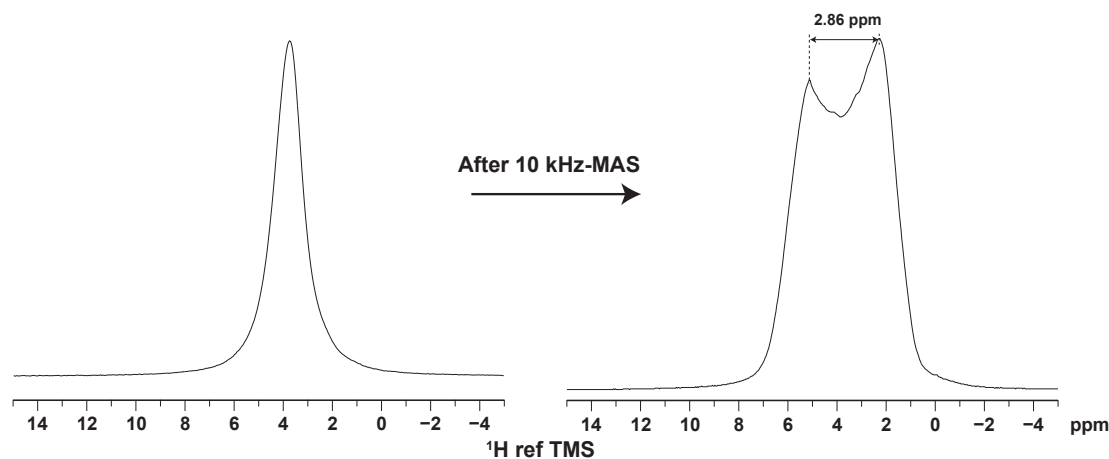


FIGURE 3.3: Comparison of the static ^1H -NMR spectra of PEO(LiTFSI) before (left) and after (right) the experiments 10 kHz-MAS. These experiments were performed at 31 °C

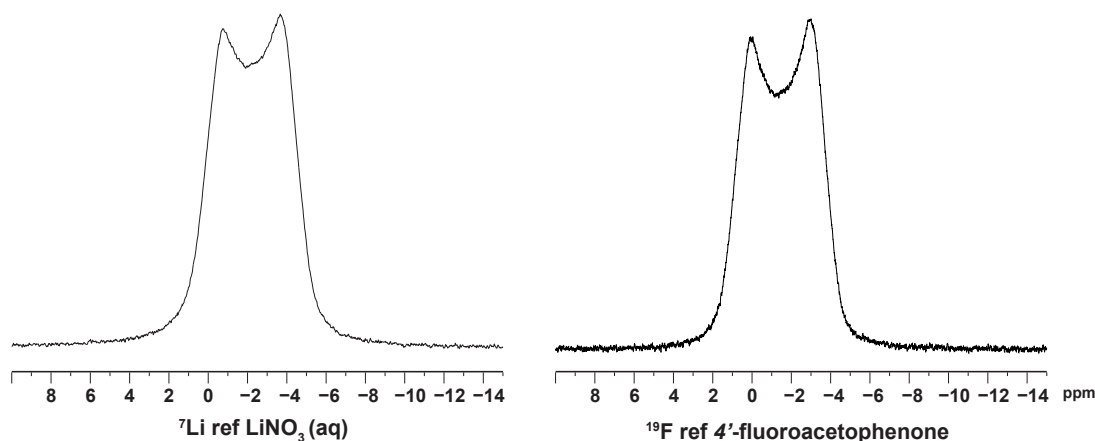


FIGURE 3.4: Static ^7Li - and ^{19}F -NMR spectra of PEO(LiTFSI) at room temperature after spinning the samples at a 10 kHz MAS rate.

arise: what happens to the polymer sample? How does this affect other properties such as diffusion and relaxation?

3.4 Previous studies

Kawamura et al. explain in their paper [85] that spinning the sample generates a pressure on it, because of the centrifugal forces that press the sample against the inner wall of the rotor. Calculations show that MAS induce a pressure that is proportional to the square of the MAS frequency. They observed the pressure effect on the equilibrium constant of [all-*trans*-bR]/[13-*cis*-bR] in retinal. They

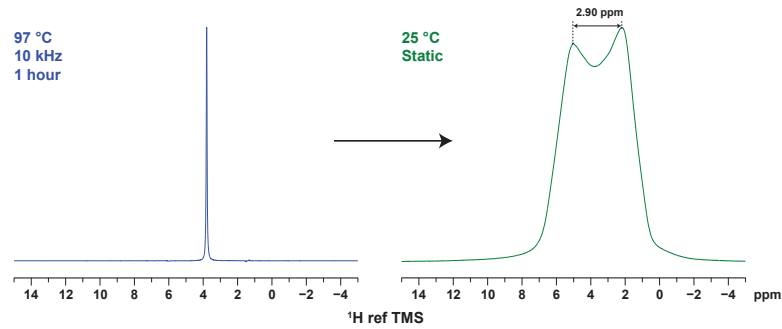


FIGURE 3.5: Comparison of ^1H -NMR spectrum under 10 kHz MAS at 97°C (left) and under static condition at 25°C (right)

also observed how this pressure generates isomerization of retinal from all-*trans* to 13-*cis* state in the membrane protein bR.

Asano et al. [86] studied by ^1H MAS-NMR styrene-butadiene rubbers samples (SBR) filled with SiO_2 (SBR/Si composite). They realized that the molecular motion of SBR/Si composites became slower because of the centrifugal forces caused by spinning the sample. The authors have also calculated the pressure P (Pa) generated by MAS at ν_R (Hz), the inner radius of the rotor r (m) and the sample density ρ (kg/m^3) by: [85, 87]

$$P = \frac{4}{3}\pi^2\nu_R^2r^2\rho \quad (3.3)$$

Furthermore, MAS affects also longitudinal relaxation T_1 of ^1H . It is shown that the molecular motions are affected by the centrifugal force.

Kitamura et al. [3] observed also the effects of pressure when studying ^{13}C MAS-NMR spectrum of natural rubber(NR). The ^{13}C -NMR spectrum, after MAS at 9 kHz for 1 days at 333 K, showed anisotropic peaks. The elongated sample showed a doublet-like peak. However, WAXD analysis exhibited that there was no crystalline phase presents, so that the doublet-like peak is caused by the existence of some molecular orientation.

Kitamura [3] showed that this lineshape did no arise from a crystalline phase but was caused by the existence of molecular orientation, which affects the local magnetic susceptibility tensor (explaining why the lineshape is the same for all nuclei when compared in ppm).

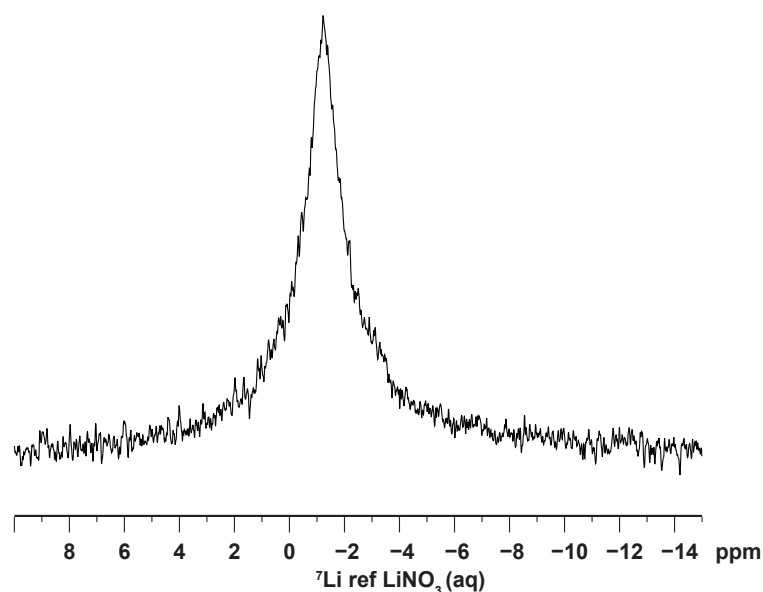


FIGURE 3.6: ${}^7\text{Li}$ -NMR spectrum of crystalline PEO(LiTFSI) at 35°C

To confirm this effect in our sample, we took a fresh polymer sample, where no splitting was observed in static spectra, placed it at 97°C , spinning at 10 kHz during 1 hour, then we cooled it down to 25°C (while spinning) and recorded a static spectrum at 25°C (see figure 3.5). The splitting of the NMR line was once again observed.

To confirm that this was not linked to pressure-induced crystallization, we recorded a 1D ${}^7\text{Li}$ -NMR spectrum of crystalline PEO(LiTFSI) (shown in figure 3.6). The ${}^7\text{Li}$ -NMR spectrum of crystalline PEO(LiTFSI) is very different from those of PEO(LiTFSI) after MAS (see figure 3.4).

3.5 Polymer state control

Choi et al. [30] have shown that the thermal history of polymer electrolytes as well as the cooling/heating rates are very important in the study of conductivity. Therefore, the thermal history of polymer electrolytes must be controlled firmly to have reproducible experiments.

First of all, we needed to understand how the state of the polymer changes in function of the temperature. We took a MAS-stretched sample, (see figure 3.3,

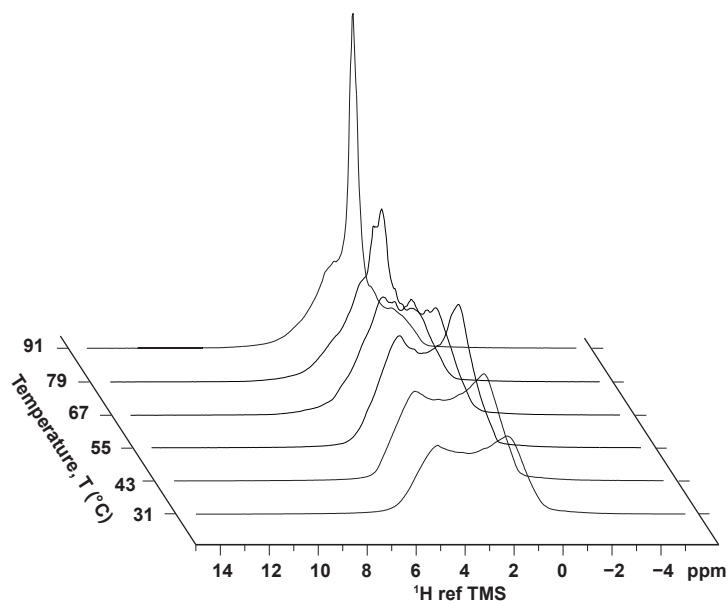


FIGURE 3.7: The evolution of the static ^1H -NMR Hahn echo spectrum as a function of temperature

right hand side), we recorded ^1H -NMR 1D spectra at various temperatures, interleaving 30 minutes waiting times between each temperature point. Figure 3.7 shows the evolution of the 1D ^1H NMR Hahn echo spectrum. From 31 to 55 °C the splitting survives, and starts vanishing at 67 °C, when the polymer starts melting. Kitamura [3] have observed same disappearance of the splitting when the sample is annealed.

The presence of a narrow component (disordered polymer) and of a splitting (still ordered polymer) may come from residual temperature gradients (the polymer is not melted everywhere in the sample), and from the kinetics of the polymer chain reorientation. To check the kinetics of this phenomenon, we recorded a series of ^1H NMR spectra at 97 °C after various evolution times (see Figure 3.8). No evolution is detected after 40 minutes, and the polymer can be considered as disordered at that stage (the lineshape is still affected by shimming and inhomogeneity issues).

We dropped the temperature down from 97 to 25 °C within 1 minute, as seen in figure 3.10 to freeze the polymer in the disordered and amorphous state. ^1H NMR spectra were recorded at 25 °C as a function of time (Figure 3.9). No evolution whatsoever of the ^1H NMR spectrum was detected after one hour.

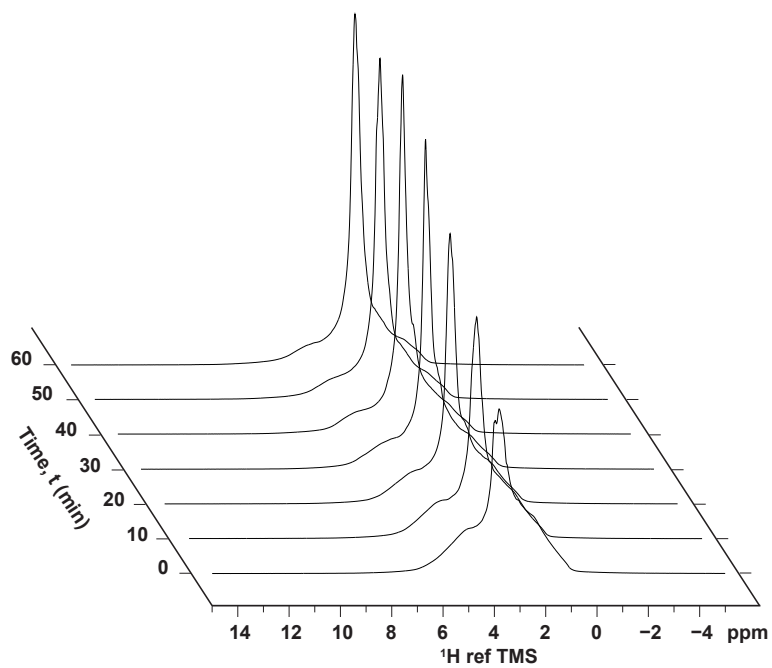


FIGURE 3.8: The evolution of the static ^1H -NMR Hahn echo spectrum at 97 $^\circ\text{C}$ as a function of time

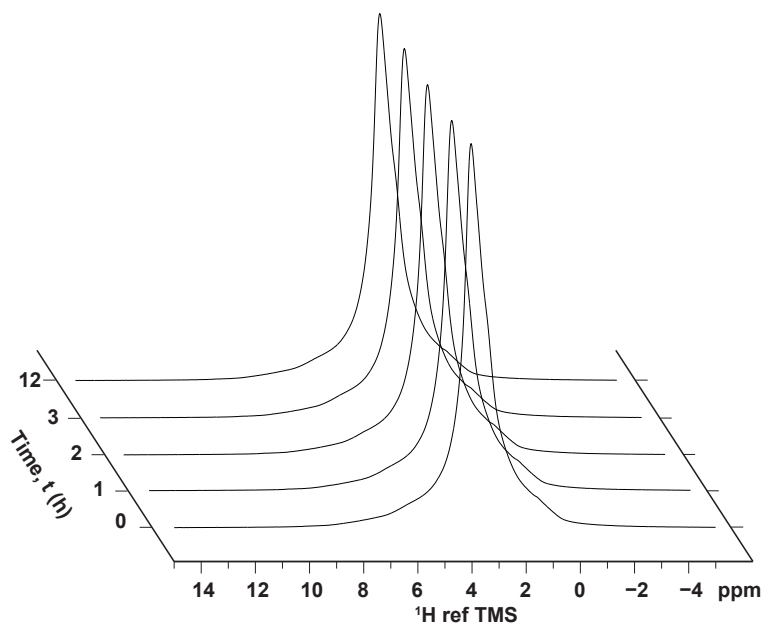


FIGURE 3.9: The evolution of the ^1H -NMR spectrum at 25 $^\circ\text{C}$ after quenching the sample from 97 $^\circ\text{C}$ under static condition

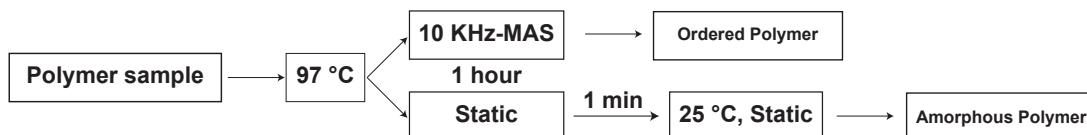


FIGURE 3.10: The scheme for controlling the polymer state

To ensure the reproducibility of our experiments, we introduced the following temperature treatment scheme (figure 3.10). The polymer sample is first completely melted at 97 °C, and quenched at 25 °C by shutting down the heating system. After one hour, the sample is considered as stabilized, and the temperature is raised at the desired temperature for relaxation or diffusion experiments. It turns out that such procedure may damage the NMR probehead and lead to difficulties in spinning the sample after a couple of heating/cooling cycles.

3.6 Diffusion and relaxation time results

It is very interesting to compare the results of diffusion and relaxation experiments with and without MAS. At the start, the sample was always conditioned in the amorphous state. Equation 3.3 was used to calculate the inner pressure induced by MAS with $\nu_R = 10^4$ Hz, $r = 1 \times 10^{-3}$ m, $\epsilon = 1.13 \times 10^3$ kg/m³. Therefore, the inner pressure inside a 3.2 mm rotor under 10 kHz MAS is around $P = 15$ bar.

Figure 3.11 shows the comparison of diffusion coefficients of Li⁺ and TFSI⁻ under 10 kHz MAS and in static conditions, at the same temperature (taking into account the real temperature inside the rotor). At around 60 °C, the change in the slope occurs at the melting temperature of our PEO(LiTFSI) polymer sample. The diffusion coefficients are fitted with an Arrhenius law, the activation energies can be found in table 3.2.

TABLE 3.2: Activation energies calculated (in kJ/mol) for D_{Li^+} and D_{TFSI^-} using an Arrhenius law.

	Static		10 kHz-MAS	
	Li ⁺	TFSI ⁻	Li ⁺	TFSI ⁻
Below T_M	101.25 ± 1.69	107.39 ± 3.42	127.90 ± 20.90	126.94 ± 16.61
Above T_M	38.15 ± 0.80	37.62 ± 0.84	47.72 ± 1.57	43.55 ± 1.71

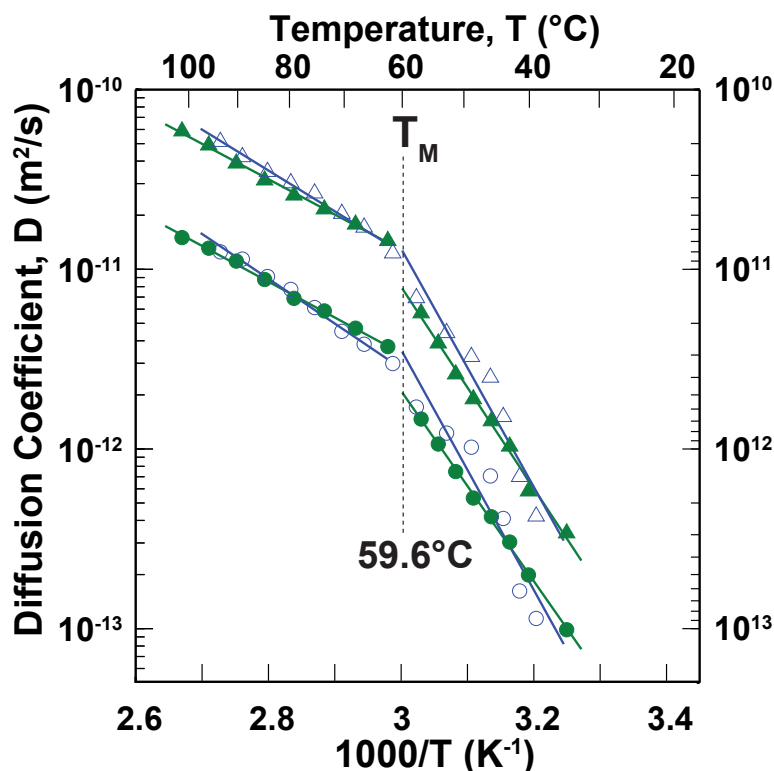


FIGURE 3.11: Diffusion coefficients of Li^+ (●) and TFSI^- (▲) under 10 kHz MAS (open blue symbols) and in static conditions (full green symbols). The continuous lines are Arrhenius fits. At low temperatures, the sensitivity of MAS experiments is much better than their static counterparts.

The diffusion coefficients can also be fitted with a VTF equation, as seen in figure 3.12. The table 3.3 shows the pseudo-activation energies calculated by the VTF fit.

TABLE 3.3: Pseudo-activation energies (kJ/mol) calculated for D_{Li^+} and D_{TFSI^-} using a VTF law, with $T_0 = -40$ °C.

	Static		10 kHz-MAS	
	Li^+	TFSI^-	Li^+	TFSI^-
Below T_M	7.34 ± 0.19	7.77 ± 0.36	9.82 ± 1.39	9.72 ± 1.06
Above T_M	4.58 ± 0.13	4.50 ± 0.20	5.46 ± 0.14	5.01 ± 0.13

In figure 3.11, the diffusion coefficients of species look very similar under both conditions. The activation energies are 18-25 % higher under MAS than in the static sample. However, when taking into account the error of the fits, we saw that the activation energies get close to each others . Anisotropic diffusion was

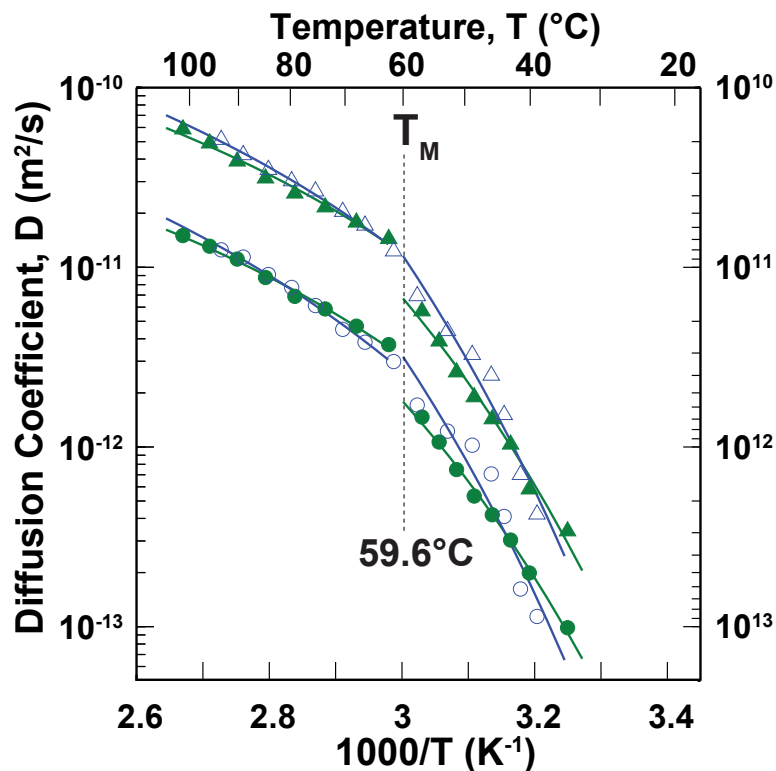


FIGURE 3.12: Diffusion coefficients of Li^+ (●) and TFSI^- (▲) under 10 kHz MAS (open blue symbols) and in static conditions (full green symbols). The continuous lines are VTF fits.

not detected as no deviation from the Gaussian decay was observed in the fitting of the attenuation curve.

On the one hand, we know that MAS has modified our sample, and that the pressure has induced some kind of alignment of the polymer chains. On the other hand, the diffusion coefficient does not change significantly under MAS, and no significant anisotropy is detected, as opposed to what Golodnitsky et al. [88] have found for PEO_9LiI : the diffusion coefficient of Li^+ measured at 60 °C can be 1.4 times faster (\parallel the stretched direction), 2.7 times slower (\perp the stretched direction) than in the unstretched one.

The longitudinal relaxation time T_1 were also recorded, as seen in figure 3.13. Interestingly, the longitudinal relaxation seems to be unaffected by spinning, although at higher temperatures, a slight difference can be detected. This may indicate that the dynamics at the nanosecond level (or close to the Larmor frequency) are unaffected by pressure.

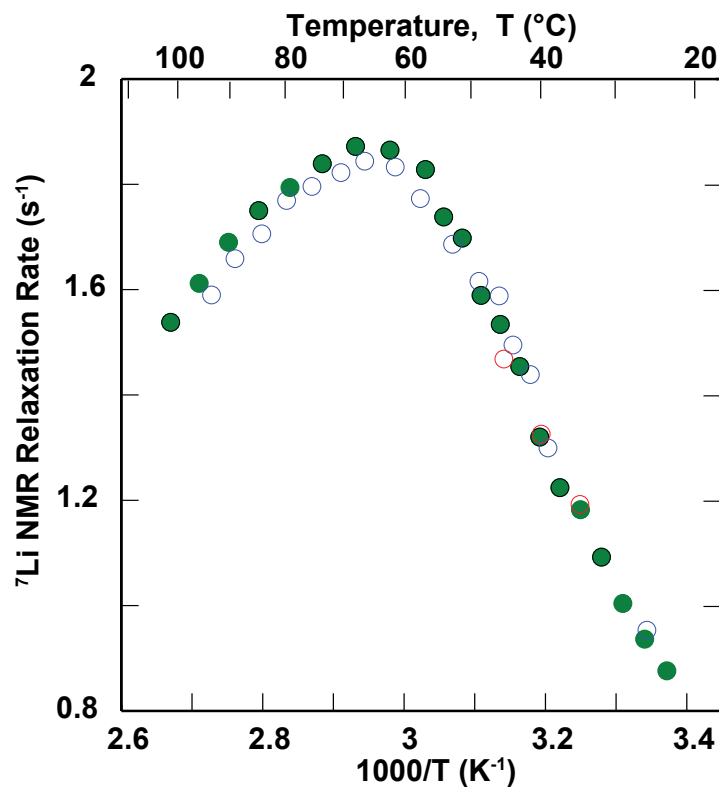


FIGURE 3.13: The longitudinal relaxation times T_1 of Li^+ in PEO(LiTFSI) under 10 kHz MAS (open blue symbols), 2 kHz MAS (open red symbols) and in static conditions (full green symbols)

3.7 Conclusion

The effect of MAS on PEO(LiTFSI) have been explored by 1D-NMR, PFG diffusion and relaxation rates measurements. The presence of a splitting is clearly caused by the change in the magnetic susceptibility tensor which is induced by MAS. This change occurs upon the ordering of the polymer chains under the pressure which results from the centrifugal forces. The diffusion coefficients of the electrolyte species and their mobility at the nanosecond timescales seem unaffected. The activation energy of the diffusion coefficients seem to be similar upon spinning the sample when we took into account the error of the fits.

The splitting is removed by melting the polymer sample, and therefore we implemented a systematic heating/cooling cycle to trap the polymer in the amorphous state and ensure the reproducibility of our experiments.

In the following, our study on relaxation rates and diffusion coefficients was performed on static samples, in order to avoid potential effects induced by MAS, such as on polymer's morphology.

Chapter 4

Relaxation times and diffusion coefficient measurement

4.1 Introduction

Lithium-polymer batteries display high specific capacities and high voltages as they benefit from the lithium-metal anode. However, at high charging rates, lithium dendrites tend to appear and lead to short-circuits, battery fire and explosions as the mechanical strength of the classical PEO polymer is small. One way to overcome this limit is to use nano-structured block copolymers[1], in which PS blocks provide the missing mechanical strength. Above their melting temperatures, block-copolymers display lower conductivities than pure PEO, as the tortuosity of the phase separated polymer slows the diffusion of Li^+ down. [50] However, at lower temperatures, the confinement effect reduces the melting temperature of the PEO domains, and the ionic conductivity of block-copolymers is comparable to the conductivity of neat PEO.

The mechanisms of Li^+ -motion were well discussed in many papers.[89] It is assumed that the Li^+ cation diffusion process is governed by the coupling of the mobile Li^+ cation with the structural relaxation modes of the polymer chains, and many studies are focused on the characterization of the polymer chain motion. For ion concentrations that give the maximum conductivity, single lithium ions are expected to be coordinated by 5-6 ether oxygens [90] and the local structures observed in crystals are expected to survive above the melting temperature. [91]

Several models[92–94] describe three mechanisms of Li^+ -motion, corresponding to motion along the polymer chain, correlated motion with the chain segments, and jumps between neighboring chains. Molecular dynamics show that lithium ions can complex oxygen atoms from several PEO chains and therefore act as cross-links with a lifetime of 13 to 40 ns [92, 95] and motions occur through changes in the lithium-oxygen bond network, with Li^+ -EO bonds that have a 0.1 to 1 ns lifetime.[96] All in all, theoretical studies based on analytical models or molecular dynamics calculations are usually in good agreement with self-diffusion coefficient or conductivity measurements. Quasi-elastic neutron scattering is usually limited to timescales around 0.1 ns, while neutron spin-echo spectrometry was used to comprehend polymer dynamics at timescales below 1.7 ns.[97] Nuclear Magnetic Resonance spectroscopy, on the other hand, can study ^7Li motion above the nanosecond timescale, but most studies obtained a single characteristic time and fail to describe the motional process in a more detailed manner. A recent study [98] highlights that contrary to the widespread belief that polymer chain motions control the ionic diffusion, the ionic mobility can be decoupled from chain motions. Therefore, more information is needed to directly characterize the motion of Li^+ at the nanosecond-nanometer scale in order to design polymer electrolytes with better mechanical properties and conductivities.

On the one hand, pulse-field gradients NMR (PFG-NMR) can be used to measure self-diffusion coefficients, which are measured for Li^+ displacement over 1-2 μm . On the other hand, Nuclear Magnetic Resonance (NMR) relaxation is able to characterize the dynamics of the fluctuations of the Hamiltonians that govern the spin system evolution. For ^7Li ($S = 3/2$), the relaxation of the spin system is governed by the quadrupolar interaction, which results from the presence of an electric field gradient (EFG) at the nucleus and are created by asymmetric charge distribution in the lithium environment. Longitudinal relaxation (characterized by T_1), for example, describes how the lithium spin polarization builds up and is the most efficient when the characteristic frequencies of the fluctuations of the quadrupolar interaction are close to the ^7Li Larmor frequency. Transverse relaxation (T_2), which describes the non-refocusable decay of single-quantum coherences is affected by slow and fast fluctuations alike, and when slow fluctuations dominate, a bi-exponential magnetization decay is observed. Most of the ^7Li relaxation measurements were made so far at a single high magnetic field and usually provided a single correlation time τ_c for the fluctuation of the lithium ion quadrupolar

interactions in the nanosecond regime. Relaxometry, on the other hand, is performed at lower magnetic fields (lower than 1 T) and has been mostly used to characterize motions on a frequency range from kHz to 10s of MHz for ^1H or ^{19}F , and therefore does not probe motion at the nanosecond timescale for ^7Li .

In this thesis, we measured longitudinal and transverse ^7Li relaxation rates at three magnetic fields (4.7, 9.4 and 17.6 T) and various temperatures ranging between 25 and 100 °C. The usage of relaxometry at high fields helps us to detect the range of motion from ns to 10s of ns. The longitudinal relaxation was observed to be single-exponential while, for transverse relaxation, bi-exponential relaxation was observed below the melting temperature for PEO(LiTFSI) and at all temperatures for PS-PEO(LiTFSI)-PS. Interestingly, above melting temperature, in PEO(LiTFSI), the transverse relaxation time was observed as single-exponential.

These relaxation rates were fitted using the Maple software with the simplest model possible describing ^7Li quadrupolar relaxation with a perturbation stemming from heteronuclear dipolar relaxation and featuring four adjustable parameters, including two nanosecond timescales τ_1 and τ_2 . Simpler models, all derived from Bloembergen-Purcell-Pound (BPP) theory,[65, 99] failed to correctly reproduce the observed relaxation rates. Similarly, using stretched exponentials or Cole-Davidson functions for correlation functions [100–102] failed to produce satisfying results.

4.2 Diffusion coefficient and conductivity of polymer samples

The diffusion coefficients of polymer samples were measured under static condition by PFG-NMR, as seen in figure 4.1. The melting temperature T_M of PEO(LiTFSI) and PS-PEO(LiTFSI)-PS was estimated by the change of slope in the diffusion coefficient curve, and the melting temperature was calculated with the averaged temperatures measured before and after such the discontinuity. The melting temperature, here, is expected to be the melting temperature of the PEO part.

Measurements were conducted such that the mean free path the ions diffusively explored over the diffusion time Δ was approximately 2 μm . The equation is used

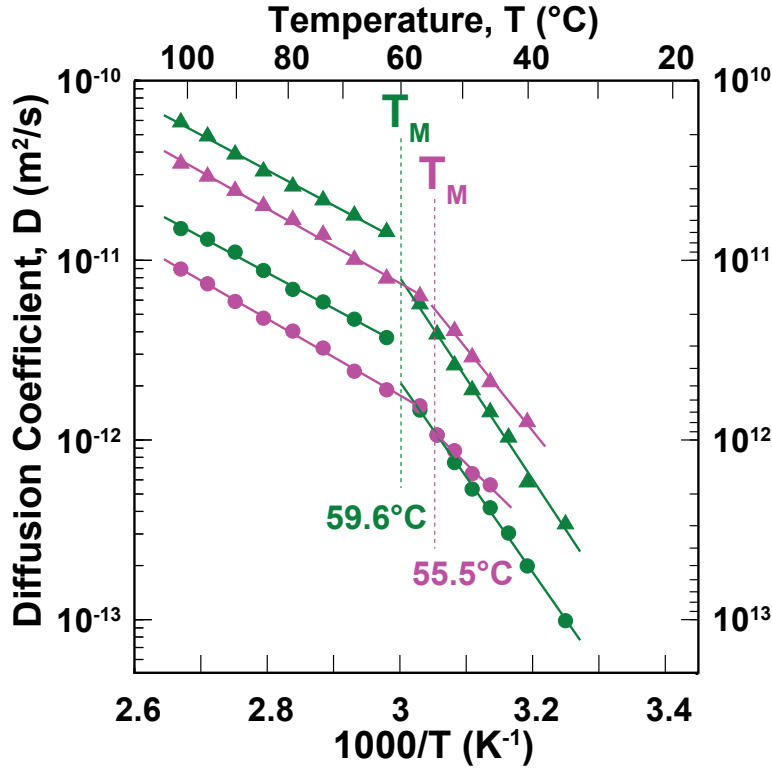


FIGURE 4.1: Diffusion coefficients of PEO(LiTFSI) and PS-PEO(LiTFSI)-PS measured under static condition: Li^+ (●), TFSI^- (▲). The lines are guides for the eyes, and the activation energies were calculated for diffusion coefficient using an Arrhenius law. The melting temperature of PEO(LiTFSI) and PS-PEO(LiTFSI)-PS were estimated around 59.6 and 55.5 $^{\circ}\text{C}$, respectively.

to calculate the mean free path:

$$I = \sqrt{6D\Delta} \quad (4.1)$$

Interestingly, the anion TFSI^- is more mobile than the Li^+ cation regardless of their respective sizes. The same phenomenon was also observed in previous studies. [2, 103, 104] It was explained by the interaction $\text{Li}^+ \dots \text{O}$ between lithium ions and oxygens in polymer chains.

The difference of T_M between PEO(LiTFSI) and PS-PEO(LiTFSI)-PS may come from the difference in molecular weight of the PEO part which is 100000 g/mol for PEO(LiTFSI) and 35000 g/mol in PS-PEO(LiTFSI)-PS. Furthermore, the decrease of the melting temperature may come from the confinement effect [105, 106] which also reduce the PEO domains crystallinity below T_M .

Above T_M , both of Li^+ and TFSI^- in PEO(LiTFSI) have higher diffusion coefficients than those in PS-PEO(LiTFSI)-PS. It is due to the PS domain which has a melting temperature of up to 240 °C. [107] The presence of PS domains over a length scale of nanometers (into which Li^+ and TFSI^- cannot diffuse) slows down the overall diffusion. The diffusion activation energies of Li^+ and TFSI^- are very similar for both polymer samples.

Below T_M , both of Li^+ and TFSI^- in PS-PEO(LiTFSI)-PS diffuses faster than those in PEO(LiTFSI). This interesting results can be explained by the confinement effect [105, 106], which lowers T_M in PS-PEO(LiTFSI)-PS and decrease its crystallinity. More amorphous region, with more mobility for polymer chains (τ_2 is shorter in PS-PEO(LiTFSI)-PS, see section 4.3) will give rise to higher diffusion coefficients, even though tortuosity slows diffusion down. The activation energies of Li^+ and TFSI^- are nearly similar for PEO(LiTFSI). For PS-PEO(LiTFSI)-PS, one can find that the activation energies of Li^+ is significantly smaller than the one measured for TFSI^- . Table 4.1 shows the activation energies calculated by the Arrhenius law for the self-diffusion coefficients of Li^+ and TFSI^- .

TABLE 4.1: Activation energies calculated (kJ/mol) for D_{Li^+} , D_{TFSI^-} and for the ionic conductivities, measured experimentally and computed from the diffusion coefficients, both using an Arrhenius law.

	PEO(LiTFSI)		PS-PEO(LiTFSI)-PS	
Diffusion coefficient	Li^+	TFSI^-	Li^+	TFSI^-
Below T_M	101.25 ± 1.69	107.39 ± 3.41	68.86 ± 6.24	87.84 ± 5.14
Above T_M	38.15 ± 0.80	37.62 ± 0.84	40.80 ± 0.63	39.64 ± 0.94
Ionic conductivity (experimental / Nernst-Einstein equation)	PEO(LiTFSI)		PS-PEO(LiTFSI)-PS	
Below T_M	144.08 ± 25.21 / 103.35 ± 2.86		97.89 ± 14.01 / 92.18 ± 4.46	
Above T_M	27.95 ± 0.31 / 34.79 ± 0.67		37.37 ± 1.05 / 36.95 ± 0.86	

The conductivities of PEO(LiTFSI) and PS-PEO(LiTFSI)-PS were also measured, as seen in figure 4.2. Activation energies of the conductivity were calculated with

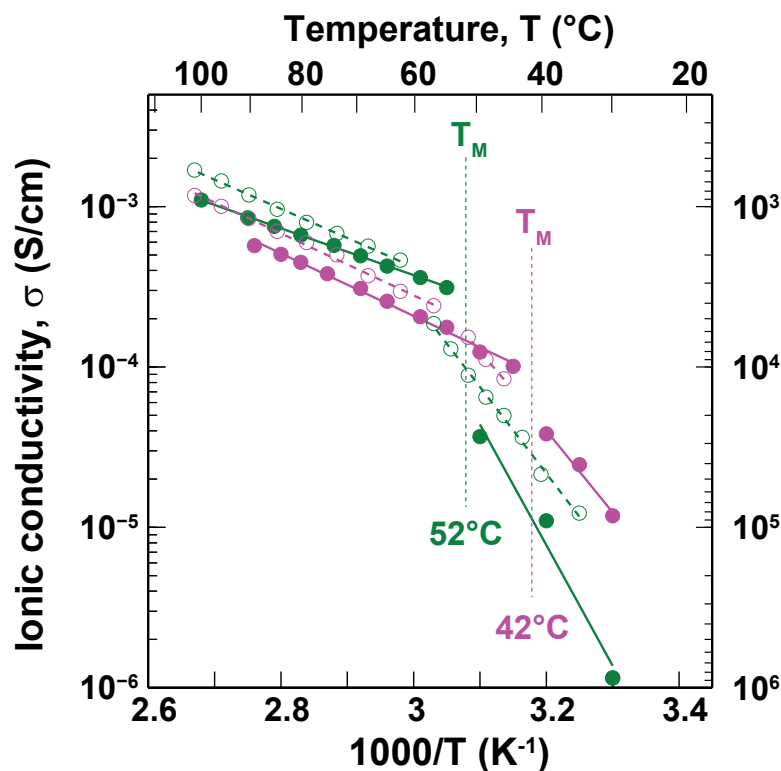


FIGURE 4.2: Ionic conductivities of **PEO(LiTFSI)** and **PS-PEO(LiTFSI)-PS**. The full symbol indicates experimental data while the open symbol indicates the data calculated with the Nernst-Einstein equation. The lines are guides for the eyes, and the activation energies were calculated for diffusion coefficients using an Arrhenius law. The melting temperature of PEO(LiTFSI) and PS-PEO(LiTFSI)-PS were estimated around 52 and 42 °C, respectively.

an Arrhenius law and the values can be found in table 4.1. The T_M found by conductivity and diffusion differ. This difference can be assigned to the kinetic of crystallization process. For diffusion measurements, we increased the temperature and waited until the system to be equilibrated. For conductivity measurements, the inverse process was performed by decreasing in the temperature. Therefore, the percent of PEO crystalline in both cases may be different to each others and it leads to the difference in melting temperature. However, the agreement between the curve is relatively good.

As expected, above T_M , the ionic conductivity in PEO(LiTFSI) is higher than in PS-PEO(LiTFSI)-PS. Below T_M , the inverse phenomena is observed again. However, the activation energies calculated from conductivity and diffusion measurements are different.

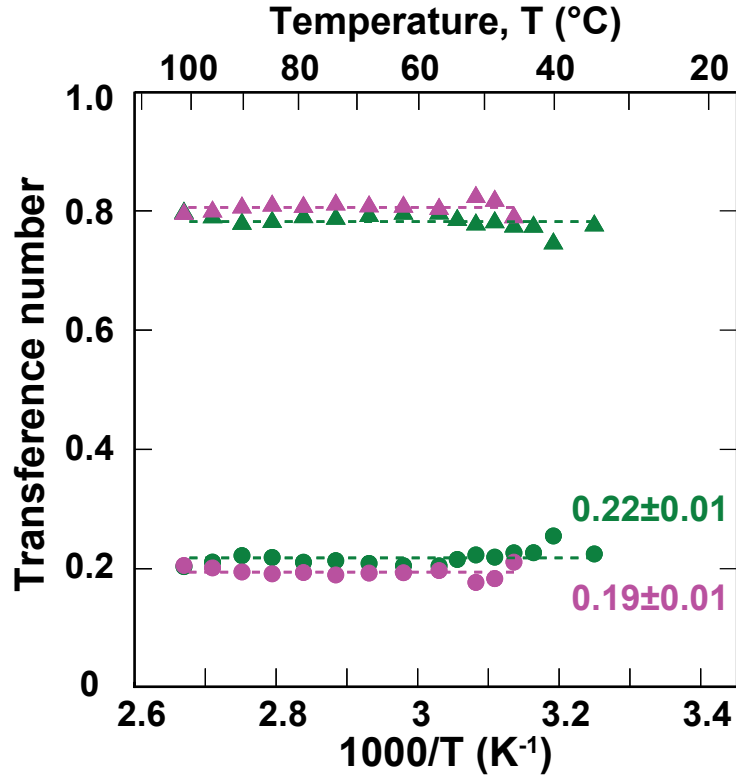


FIGURE 4.3: The transference numbers of Li^+ (●) and TFSI^- (▲) in $\text{PEO}(\text{LiTFSI})$ and $\text{PS-PEO}(\text{LiTFSI})\text{-PS}$. The dashed lines show the average values of transference numbers.

The conductivity calculated by the Nernst-Einstein equation shows an overestimated value in comparing with experimental data, see figure 4.2, the same observation was reported by Arumugam. [2] The main reason may be the presence of ion pairs and of larger ion clusters which do not (or less) contribute to the conductance. The existence of ion pairs may be expected as the diffusion activation energies for Li^+ and TFSI^- are similar, seemingly indicating a correlated diffusion process.

Figure 4.3 show the transference number of Li^+ and TFSI^- in $\text{PEO}(\text{LiTFSI})$ and $\text{PS-PEO}(\text{LiTFSI})\text{-PS}$, the calculation was performed by using the equations:

$$t_+ = \frac{D_{\text{Li}^+}}{D_{\text{Li}^+} + D_{\text{TFSI}^-}} \quad (4.2a)$$

$$t_- = \frac{D_{\text{TFSI}^-}}{D_{\text{Li}^+} + D_{\text{TFSI}^-}} \quad (4.2b)$$

The transference numbers seem to be temperature-independent. The average

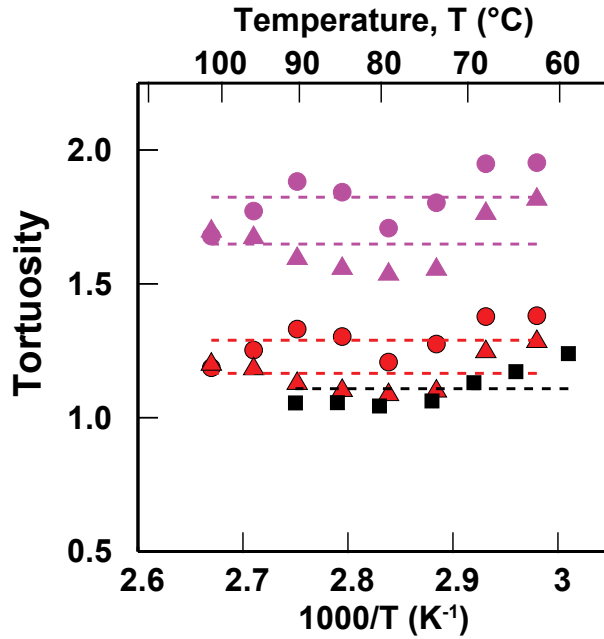


FIGURE 4.4: The tortuosities of Li^+ (●), TFSI^- (▲) in PS-PEO(LiTFSI)-PS were calculated by using equation 4.3; Li^+ (●), TFSI^- (▲) present for the tortuosities calculated by taking into account of volume fraction of PEO-TFSI ($\epsilon=0.707$). The tortuosity from conductivity is calculated by equation 4.4 (■).

The dashed lines represent for average values of each species.

transference numbers of Li^+ are 0.22 ± 0.01 and 0.19 ± 0.01 for PEO(LiTFSI) and PS-PEO(LiTFSI)-PS, respectively.

In PS-PEO(LiTFSI)-PS, the diffusion of species is deviated from straight path by the presence of PS domains (see figure 4.5a). [108] The tortuosity (\mathcal{T}) represents this deviation and was calculated by: [108]

$$\mathcal{T} = \frac{D_m}{D_{m'}} \quad (4.3)$$

where D_m , $D_{m'}$ are the diffusion coefficients of diffusing species without and with the presence of PS part, respectively. The equation 4.3 will be $\mathcal{T} = \frac{D_{\text{PEO(LiTFSI)}}}{D_{\text{PS-PEO(LiTFSI)-PS}}}$. Figure 4.4 shows the tortuosity calculated for PS-PEO(LiTFSI)-PS, assuming that, on the lengthscale of PEO domains, the diffusion coefficients are equal whether they are attached to PS chains at each end or not.

The calculation was performed above the melting temperature, as below T_M , crystalline domains may be found in PEO (in which Li^+ can't diffuse), creating some sort of undetermined tortuosity. As presented in ref. [50], Bouchet et al. have discussed the effect of the PS part in PS-PEO(LiTFSI)-PS. They proposed that

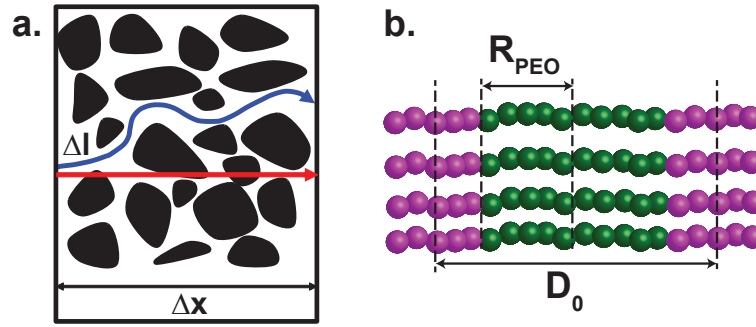


FIGURE 4.5: (a) Representation of tortuosity: the red arrow presents the straight path of the moving species in case of homogeneous polymer PEO(LiTFSI) while the blue one presents for the case of block copolymer PS-PEO(LiTFSI)-PS. The black areas shows for the PS domains. (figure adapted from ref [108]) (b) Size of polymer domains in block copolymer PS-PEO(LiTFSI)-PS where $R_{PEO}=9.45$ nm, $D_0=25$ nm.

the tortuosity can be calculated by:

$$\mathcal{T}(\epsilon) = \frac{\sigma^0 \epsilon}{\sigma} \quad (4.4)$$

where ϵ is the volume fraction of PEO-LiTFSI. σ_0 and σ are the conductivities of pure PEO(LiTFSI) and PS-PEO(LiTFSI)-PS, respectively. The authors postulated the existence of a "dead-zone" where ionic motion is forbidden (see figure 4.6). [106] The volume fraction of PEO domains seemed to be smaller than expected, indicating that a fraction of the PEO volume, at the interface between PS and PEO, is either forbidden for Li^+ or its conductivity is considerably reduced in it. The conductivity is affected by the volume fraction of PEO-LiTFSI and the thickness λ of the dead zone at the PS/PEO interface. The tortuosity was recalculated:

$$\mathcal{T}(\epsilon) = \frac{\sigma^0 \epsilon(\lambda)}{\sigma(\epsilon)} \quad (4.5)$$

The tortuosity calculated from diffusion coefficients with taking into account the volume fraction of PEO is, interestingly, close to what was obtained from the conductivities.

However, the assumption that the conductivity in PEO domain of PS-PEO(LiTFSI)-PS is identical to the conductivity in homogeneous PEO(LiTFSI), need to be proved. The technique PFG-NMR as well as conductivity measure ionic displacements at the macroscopic length scale (i.e. ≥ 1 μm). Therefore, to understand

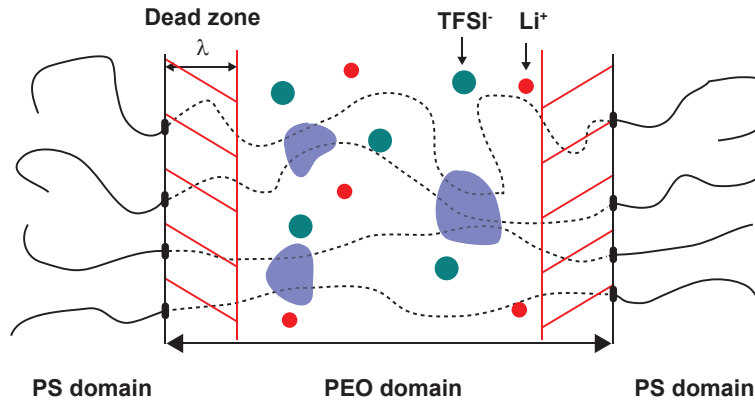


FIGURE 4.6: The representation of the microstructure of the BCE. The hatched red areas show the "dead zone" where the ions can't diffuse. The purple areas are PEO crystallites. (figure adapted from [50])

the Li⁺ mobilities over the size of the PEO domains ($\approx 20\text{nm}$, see figure 4.5b), we need relaxation study.

4.3 Relaxation rates R_1 and R_2 characterization

4.3.1 Calculation of relaxation rates

The relaxation matrix, \mathbf{R} can be described as:[109]

$$\mathbf{R} = \mathbf{R}^Q + \mathbf{R}^D + \mathbf{R}^{CSA} \quad (4.6)$$

assuming that the fluctuations of the quadrupolar (Q), dipolar (D) and chemical shift anisotropy interactions (CSA) are not correlated. For ${}^7\text{Li}$ ($S = 3/2$), the relaxation of the spin system is governed by the quadrupolar interaction, which results from the presence of an electric field gradient (EFG) at the nucleus, created by asymmetric charge distribution in the lithium environment. The relaxation rate of quadrupolar nuclei have been calculated elsewhere and are linear combinations of the spectral density function $J_{QQ}(0)$, $J_{QQ}(\omega_0)$ and $J_{QQ}(2\omega_0)$ which are the Fourier transforms of the correlation function $C_{QQ}(\tau)$ at 0, once and twice ω_0 (the Larmor frequency). [60]

For longitudinal relaxation time (T_1), the bi-exponential curve was showed as 80/20 % weight for the fast and slow components. However, these two rates are very

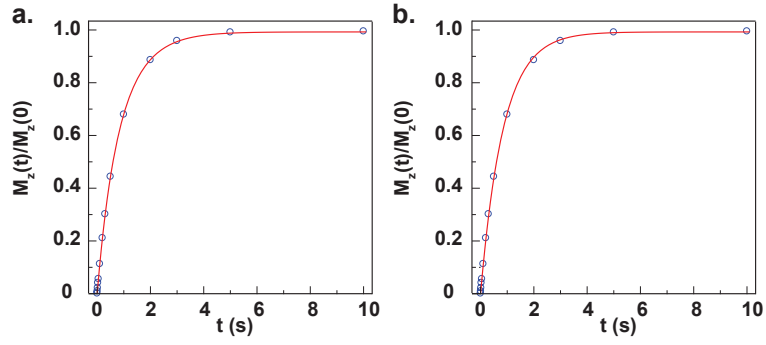


FIGURE 4.7: Comparison of bi-exponential (a) and single-exponential (b) longitudinal relaxation fits (^7Li longitudinal relaxation time of PEO(LiTFSI) at 35 °C). There is almost no difference between bi- and single-exponential fits.

close to each others and a single-exponential magnetization recovery was detected with an effective longitudinal relaxation rate (see figure 4.7 and section 2.2.1 for details) equal to:

$$R_1 = \frac{4\pi^2 \langle C_Q^2 \rangle}{50} [J(\omega_0) + 4J(2\omega_0)] \quad (4.7)$$

For transverse relaxation, the behavior is clearly bi-exponential at low temperatures (i.e. single exponential functions do not fit the relaxation curve, see figure 4.8, and section 2.2.2 for details), with:

$$R_{2,\text{fast}} = \frac{4\pi^2 \langle C_Q^2 \rangle}{20} [J(0) + J(\omega_0)] \quad (4.8)$$

$$R_{2,\text{slow}} = \frac{4\pi^2 \langle C_Q^2 \rangle}{20} [J(\omega_0) + J(2\omega_0)] \quad (4.9)$$

Above melting temperature (estimated by diffusion measurements above), in PEO(LiTFSI), $\omega_0\tau < 1$, and the bi-exponentiality becomes difficult to detect, and therefore, an effective relaxation rate (see figure 4.9) is measured in a similar manner to what was done for longitudinal relaxation:

$$R_2 = \frac{4\pi^2 \langle C_Q^2 \rangle}{20} \left[\frac{3}{5}J(0) + J(\omega_0) + \frac{2}{5}J(2\omega_0) \right] \quad (4.10)$$

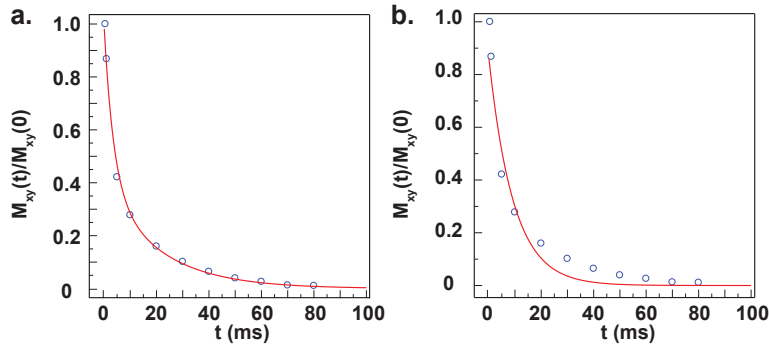


FIGURE 4.8: Comparison of bi-exponential (a) and single-exponential (b) transverse relaxation fits (${}^7\text{Li}$ transverse relaxation time of PEO(LiTFSI) at 35 °C). The biexponential fit gives a better fit than single-exponential one.

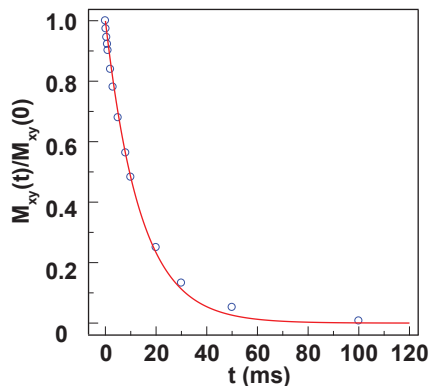


FIGURE 4.9: The single-exponential transverse relaxation fit (${}^7\text{Li}$ transverse relaxation time of PEO(LiTFSI) at 75 °C)

The experimental data of relaxation times of PEO(LiTFSI) and PS-PEO(LiTFSI)-PS was shown in figure 4.10 and 4.11, respectively.

4.3.2 Simple models: Bloembergen–Purcell–Pound (BPP) and Cole-Davidson function

The data was interpolated with polynomial functions to enable the simultaneous fit of the relaxation rates at various temperatures between 25 and 100 °C. At first, we started with the simple Bloembergen–Purcell–Pound (BPP) model, based on isotropic rotational diffusion of molecules. The correlation function $C(t)$ is a single exponential decay: $C(t) = \exp(-t/\tau)$. The spectral density was given by $J_n = \frac{\tau_c}{1+n^2\omega^2\tau_c^2}$. The calculation method was shown in appendix A. Figure 4.12 shows the fitting results of PEO(LiTFSI) relaxation rates by the BPP model. This model cannot reproduce both R_1 and R_2 .

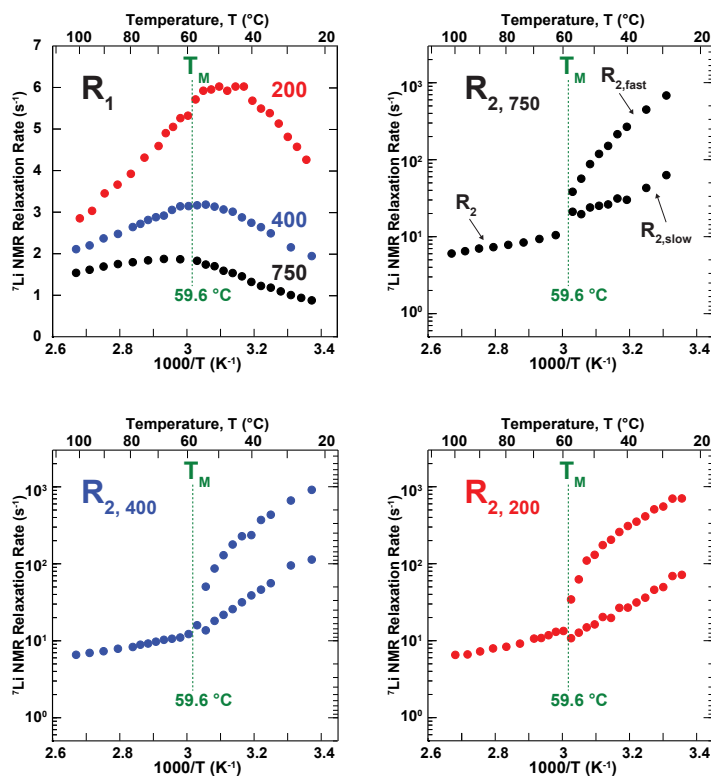


FIGURE 4.10: Relaxation rates R_1 and R_2 observed for ^7Li in PEO(LiTFSI) at three magnetic fields (17.4 T, 9.4 T, 4.7 T) and various temperatures.

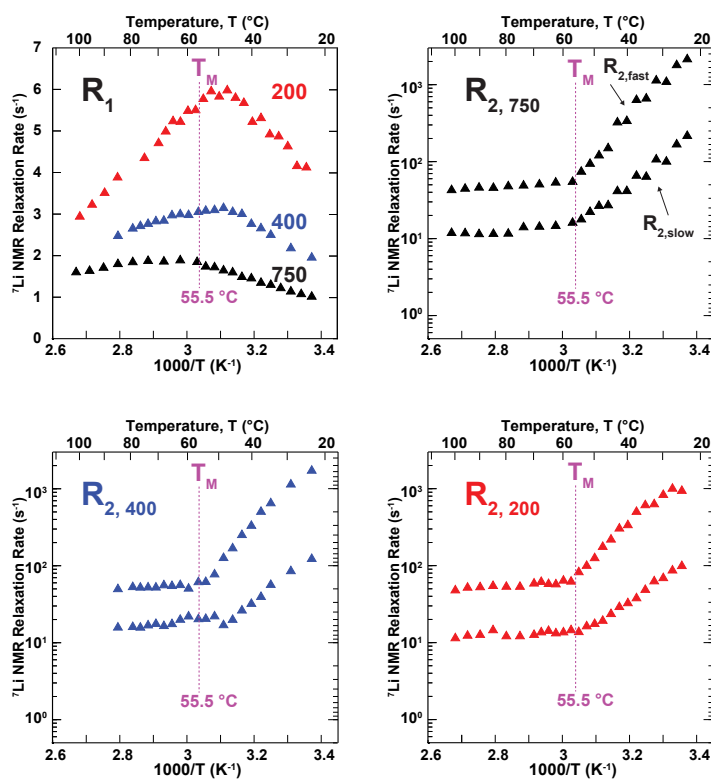


FIGURE 4.11: Relaxation rates R_1 and R_2 observed for ^7Li in PS-PEO(LiTFSI)-PS at three magnetic fields (17.4 T, 9.4 T, 4.7 T) and various temperatures.

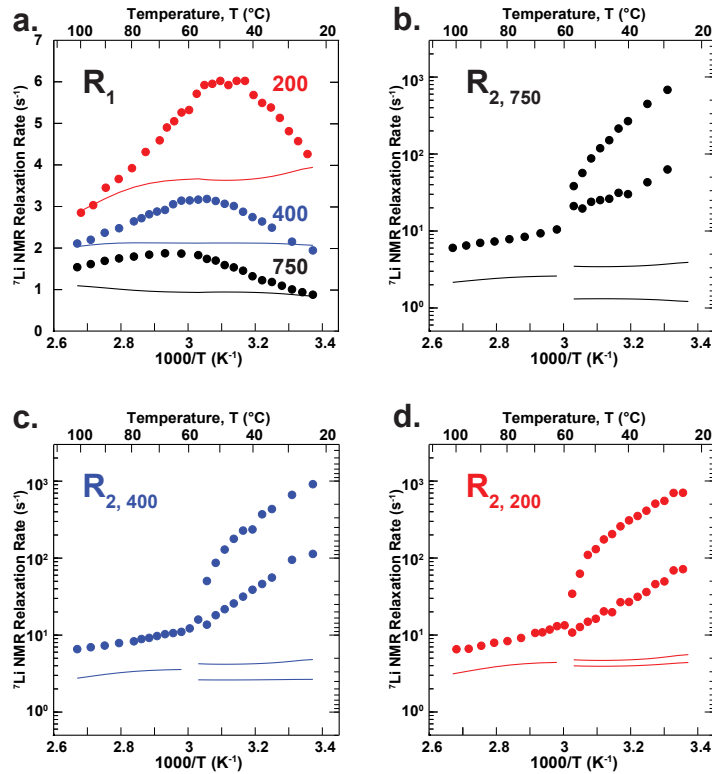


FIGURE 4.12: Fitting results of PEO(LiTFSI) relaxation rates using the BPP model. The continuous lines represent the fitted curves for R_1 and R_2 .

To introduce distributions of correlation times, the Cole-Davidson (CD) function was also used, and the spectral density of the CD function is described by $J_n = \frac{2 \sin(\beta \arctan(\omega\tau_c))}{\omega [1+(n^2\omega^2\tau_c^2)^{\beta/2}]}$. The best results were obtained here with $\beta = 0.56$. This function cannot reproduce the experimental data (see figure 4.13).

4.3.2.1 $\langle C_Q^2 \rangle$ variation

Arun et al. observed a temperature dependence of the quadrupolar coupling constant [110] when fitting the ^7Li longitudinal relaxation times while using the Bloembergen–Purcell–Pound (BPP) model for the correlation function in the following intercalated polymer electrolyte: $\text{Cd}_{0.75}\text{PS}_3\text{Li}_{0.5}(\text{PEO})$. In a follow-up paper [111], the authors gave a full description of this behavior. Halstead et al. argued that there are three mechanisms explaining the increase in quadrupolar coupling constants [112]:

- a change in the electric field gradient (EFG) at the origin of the quadrupolar interaction caused by changes in the atomic coordinates

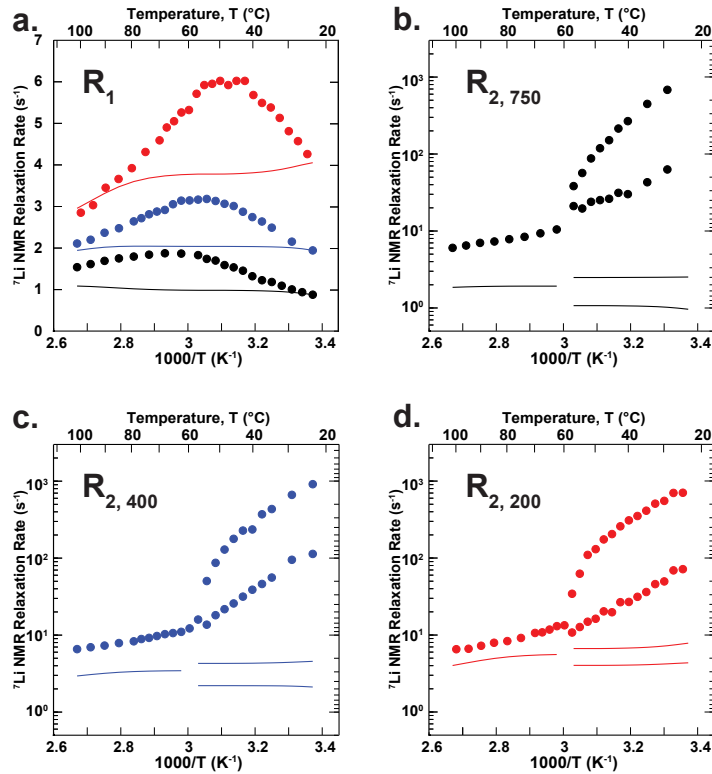


FIGURE 4.13: Fitting results of PEO(LiTFSI) relaxation rates using the CD spectral density function. The continuous lines represent the fitted curves for R_1 and R_2 .

- a change in the EFG caused by a modification of the electric density distribution
- a change in the time average of the EFG "felt" by the moving nucleus

In Arun's case, the temperature dependence of the quadrupolar coupling constant is due to the time averaged electric field gradient (EFG). As temperature increase, the region of space in which the Li^+ ion is located changes and the magnitude of the time averaged EFG depends on the shape and extent of this region. In the next paper [111], Arun et al. described the time average of the electric field gradient sampled by a ^7Li nucleus vibrating anisotropically about its equilibrium value [112]. The full details can be found in their papers. The longitudinal relaxation time equation, which Arun used, is [111]:

$$\frac{1}{T_1} = \omega_Q^2(T) [J(\omega_0) + 4J(2\omega_0)] = \omega_Q^2(T) \left[\frac{\tau_c}{1 + \omega_0^2 \tau_c^2} + \frac{4\tau_c}{1 + 4\omega_0^2 \tau_c^2} \right] \quad (4.11)$$

where ω_Q^2 represents the quadrupolar coupling pre-factor. The correlation time τ_c was described by an Arrhenius law: $\tau_c = \tau_0 \exp(-E_a/kT)$. They found that

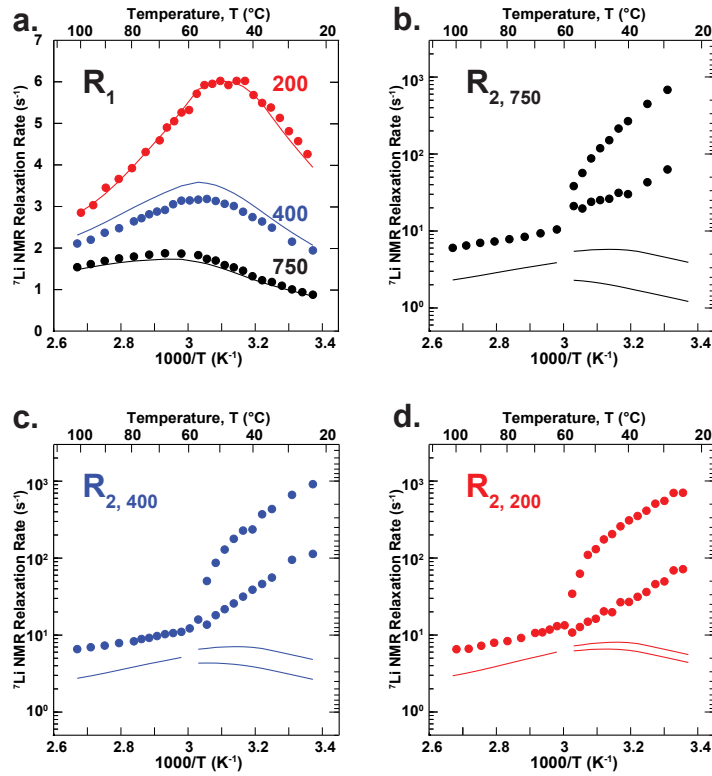


FIGURE 4.14: Fitting results of PEO(LiTFSI) relaxation rates using the BPP model with $\langle C_Q \rangle$ variation.

the quadrupolar coupling pre-factor was constant below 50 °C and increased with temperature above 50 °C.

Inspired by this idea, we let the quadrupolar coupling pre-factor vary freely in our fits. Figures 4.14 and 4.15 show the results using either the BPP or CD spectral density functions, respectively, with adjusted $\langle C_Q^2 \rangle$. The longitudinal relaxation rates are more correctly reproduced, and the CD function gives better results than the BPP model. However, the calculation of transverse relaxation rates is still poor.

Therefore, it appears that allowing the pre-factor $\langle C_Q^2 \rangle$ to vary with T is necessary to reproduce the longitudinal relaxation rates.

4.3.2.2 Dipolar Relaxation term R_{DD}

The poor agreement between our fits and the transverse relaxation times shown above pointed towards the contribution of others NMR interactions to transverse

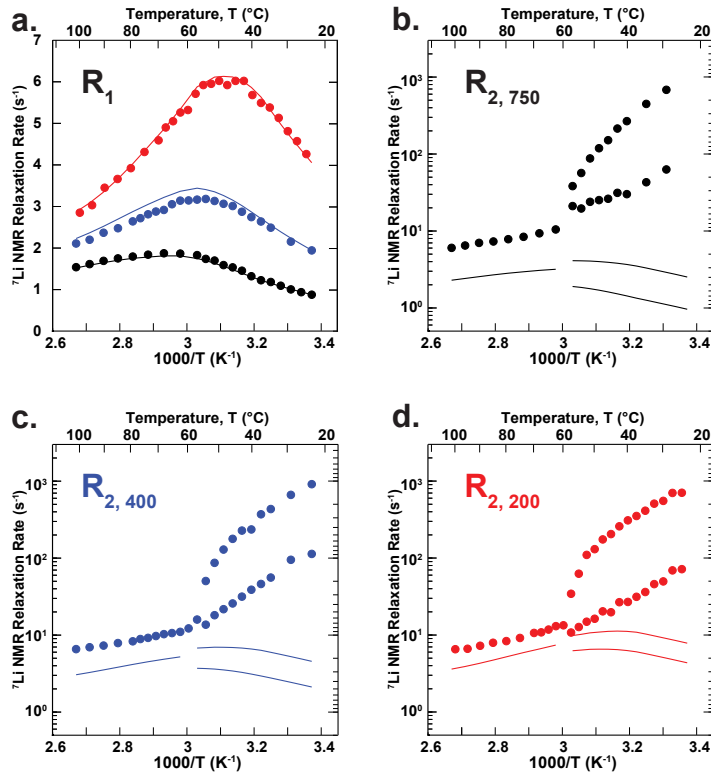


FIGURE 4.15: Fitting results of PEO(LiTFSI) relaxation rates using the CD spectral density function with $\langle C_Q \rangle$ variation.

relaxation. In ref [109], Eliav et al. have shown that both dipolar and quadrupolar interaction can potentially contribute to T_1 and T_2 . The magnitude of the quadrupolar interaction C_Q is around tens of kHz, while the dipolar interaction between ${}^7\text{Li}$ and ${}^1\text{H}$ (as the salt concentration allows us to neglect the other pairs) is a secondary potential source of relaxation, the magnitude of which is 1.7 kHz for ${}^1\text{H}$ - ${}^7\text{Li}$ pairs separated by 3 Å.[109] Therefore, the dipole-dipole term is considered as a perturbation in our treatment, while dipolar-quadrupolar cross-terms will be neglected here. ${}^{19}\text{F}$ atoms from the TFSI anion are expected to be more than 5 Å away and are expected to provide a minor contribution to relaxation [104, 113, 114] which would be at least an order of magnitude lower than the quadrupolar interaction measured at low temperatures (tens of kHz). Moreover, T_1 measurements in protonated and 100% deuterated PEO gave similar results.[113] Therefore, we neglected the dipolar contribution to longitudinal relaxation. However, fitting both T_1 and T_2 is impossible without taking into account a supplementary term, which is independent of the magnetic field and affects the three transitions of ${}^7\text{Li}$ in the same manner (no multi-exponential relaxation). The fact that it is both field independent and does not contribute to multi-exponential relaxation is in favor of dipolar interactions and rules out any effects from the chemical shift anisotropy. As

first, it is field independent and second, it does not affect longitudinal relaxation, it is most probably a contribution of the ^1H - ^7Li heteronuclear dipolar coupling with a dominant contribution from $J_{DD}(0)$. A "slow" fluctuation of this dipolar interaction would be characterized by a long correlation time τ_{dip} , leading to a large spectral density at 0 frequency $J_{DD}(0)$ and smaller spectral densities at the Larmor frequency $J_{DD}(\omega_0)$, resulting in a negligible contribution to longitudinal relaxation.

As seen in equations 4.12a-4.12b, the dipolar relaxation term is the additional term taking into account the contribution of ^7Li - ^1H dipolar interactions. Figures 4.16 and 4.17 show the calculations with this additional term R_{DD} , contributing to fast and slow transverse relaxation rates below T_M .

$$R_{2,\text{fast}} = \frac{4\pi^2 \langle C_Q^2 \rangle}{20} [J(0) + J(\omega_0)] + R_{DD} \quad (4.12a)$$

$$R_{2,\text{slow}} = \frac{4\pi^2 \langle C_Q^2 \rangle}{20} [J(\omega_0) + J(2\omega_0)] + R_{DD} \quad (4.12b)$$

$$R_2 = \frac{4\pi^2 \langle C_Q^2 \rangle}{20} \left[\frac{3}{5}J(0) + J(\omega_0) + \frac{2}{5}J(2\omega_0) \right] + R_{DD} \quad (4.12c)$$

The longitudinal relaxation and slow transverse can be correctly fitted together. However, above T_M , the calculation of transverse relaxation rates is still unsatisfactory. Therefore, we added a dipolar relaxation term above T_M (equation 4.12c), as seen in figures 4.18 and 4.19.

These calculations were performed to demonstrate the need for a $\langle C_Q^2 \rangle$ dependence to temperature, and the importance of the additional dipolar term to reproduce the relaxation rates. Furthermore, the failure of simple models like BPP and CD function lead to consider multi-exponentials correlation functions in our relaxation model. Moreover, the dipolar relaxation term strongly affects transverse relaxation rates. The same observation was found for PS-PEO(LiTFSI)-PS.

4.3.3 Multi-exponentials correlation function

To describe the effect of the fluctuations of the quadrupolar interaction on the relaxation properties of ^7Li spins, we consider that the correlation function can

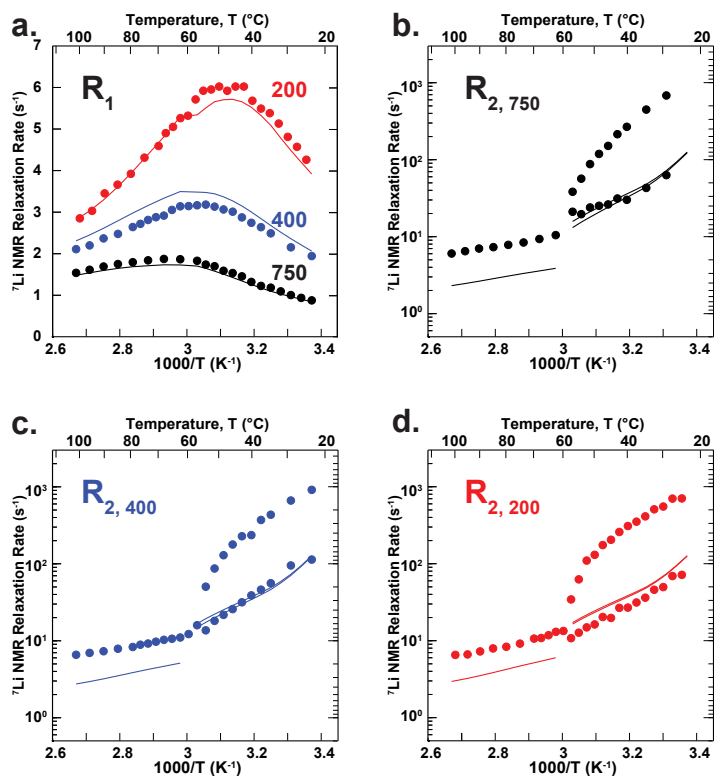


FIGURE 4.16: Fitting results of PEO(LiTFSI) relaxation rates using the BPP model with $\langle C_Q \rangle$ variation and a dipolar relaxation term below T_M .

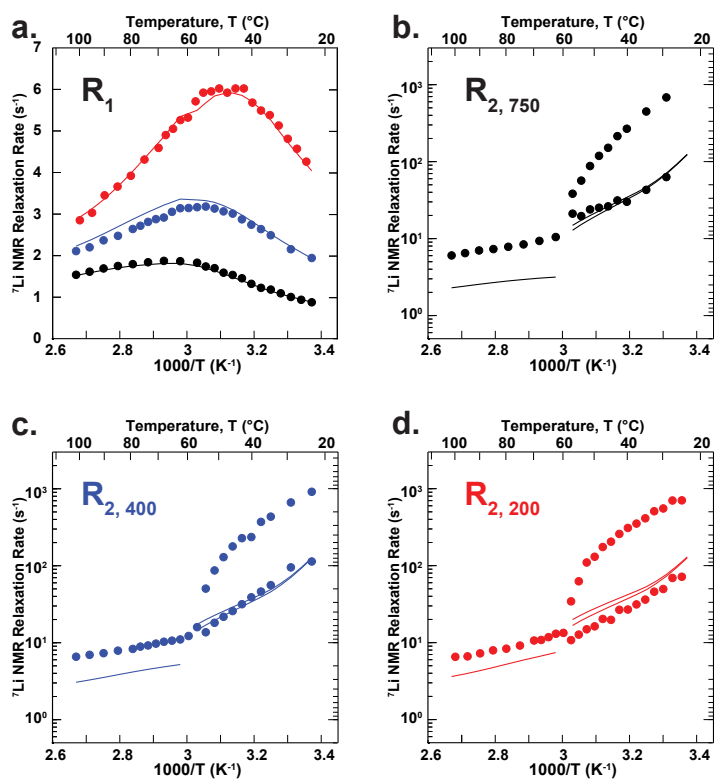


FIGURE 4.17: Fitting results of PEO(LiTFSI) relaxation rates using the CD spectral density function with $\langle C_Q \rangle$ variation and a dipolar relaxation term below T_M .

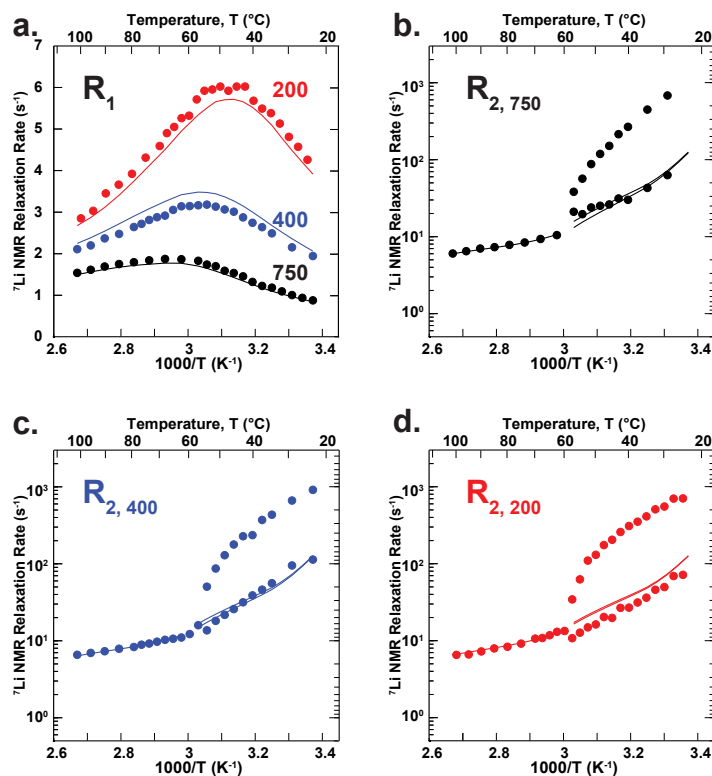


FIGURE 4.18: Fitting results of PEO(LiTFSI) by using the BPP model with $\langle C_Q \rangle$ variation and a dipolar relaxation term at all temperatures.

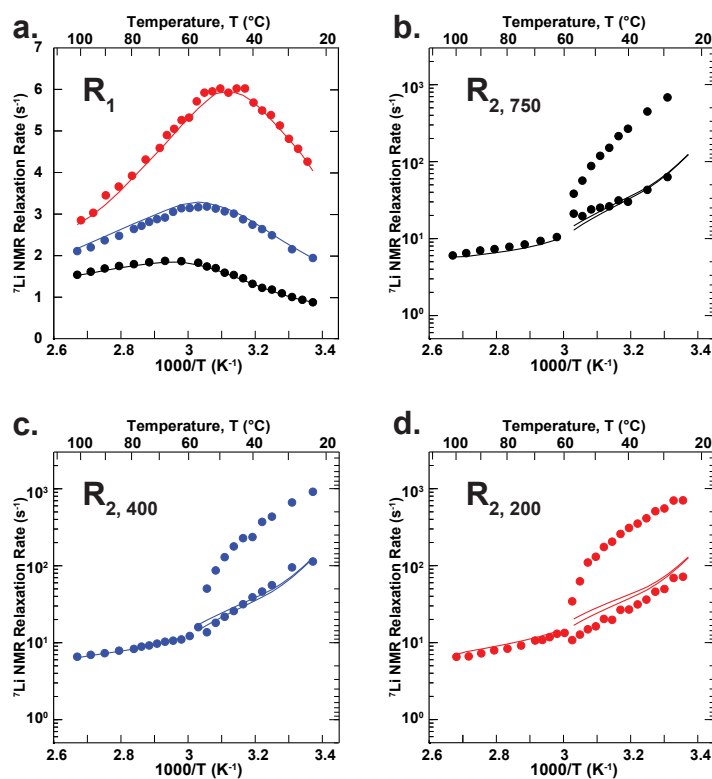


FIGURE 4.19: Fitting results of PEO(LiTFSI) relaxation rates using the CD spectral density function with $\langle C_Q \rangle$ variation and a dipolar relaxation term at all temperatures.

be described by a normalized and discrete sum of exponential functions,[64] and therefore, the spectral density function J can be written:

$$J(\omega, \tau_i, x_{ij} \dots) = \sum_i A_i(\tau_i, x_{i1}, x_{i2}, \dots) \frac{2\tau_i}{1 + \omega^2\tau_i^2} \quad (4.13)$$

where $A_i(\tau_i, x_{i1}, x_{i2}, \dots)$ is the weight of the i^{th} exponential correlation function characterized by the correlation time τ_i .

This strategy has been often used in NMR, especially for the correlation function describing the fluctuations of dipolar interactions stemming from internal bond motions and molecular tumbling in molecules.[70] In our case, we assumed that the quadrupolar interaction fluctuates at three different timescales:

- a. Very fast motions (e.g. vibrations) over sub-nanosecond timescales partly average ^7Li quadrupolar couplings, and therefore are reflected in the temperature-dependent pre-averaged $\langle C_Q^2 \rangle$ [111]
- b. Fluctuations in the coordination polyhedron of lithium ions to neighboring oxygen atoms and the concerted motion of statistical or Kuhn's segments of the polymer chains lead to partial averaging of the quadrupolar interaction, this averaging is described by an order parameter S^2 -i.e. the proportion of quadrupolar interaction that remains to be averaged at the end of this process- and a characteristic time τ_1 .
- c. The quadrupolar interaction is completely averaged over a longer timescale τ_2 , as the lithium has moved to an environment with a completely different EFG orientation. Complete reorientation of the Kuhn's segment is expected to occur on a slower timescale as our polymers are entangled, having a molar mass larger than the critical molecular mass (around 5000 g/mol for PEO[115]).

Figure 4.20 shows a simple model which depicts the influence of oxygen coordination around Li^+ . As the oxygen atoms get close to Li^+ , the electron cloud of Li^+ is deformed in the Li-O direction. This assumption was similar to Chung's study, [116] as they have found the changing of EFG distribution when passing from unstretched to stretched polymer. This changing was implied by the change of Li-O bond angle and lengths upon stretching the polymer.

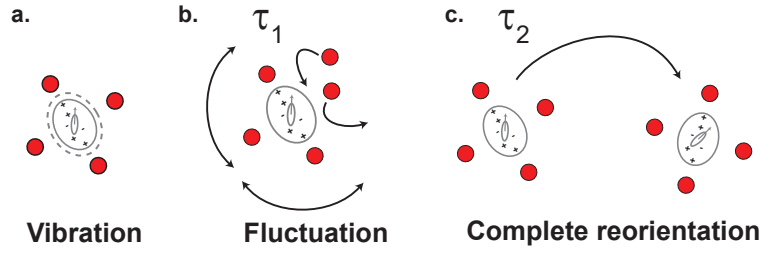


FIGURE 4.20: Modeling of the fluctuations of the quadrupolar interaction at three different timescales

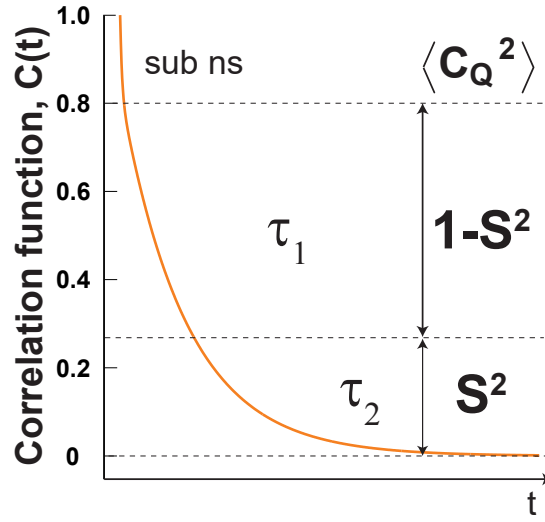


FIGURE 4.21: Correlation function's representation diagram of three different timescales.

The correlation function describing these two last averaging processes can therefore be written as (see figure 4.21):

$$C(t) = \left[(1 - S^2) \exp\left(\frac{-t}{\tau_1}\right) + S^2 \right] \exp\left(\frac{-t}{\tau_2}\right) \quad (4.14)$$

And the corresponding spectral density is given by:

$$J(\omega) = \frac{(1 - S^2) \tau_{12}}{1 + \omega^2 \tau_{12}^2} + \frac{S^2 \tau_2}{1 + \omega^2 \tau_2^2} \quad (4.15)$$

with

$$\frac{1}{\tau_{12}} = \frac{1}{\tau_1} + \frac{1}{\tau_2} \approx \frac{1}{\tau_1} \quad (4.16)$$

if $\tau_2 \gg \tau_1$.

$\langle C_Q^2 \rangle$, τ_1 , τ_2 and S^2 parameters retrieved from the relaxation data are shown in figure 4.24, for both PEO(LiTFSI) and PS-PEO(LiTFSI)-PS. In figures 4.22 and

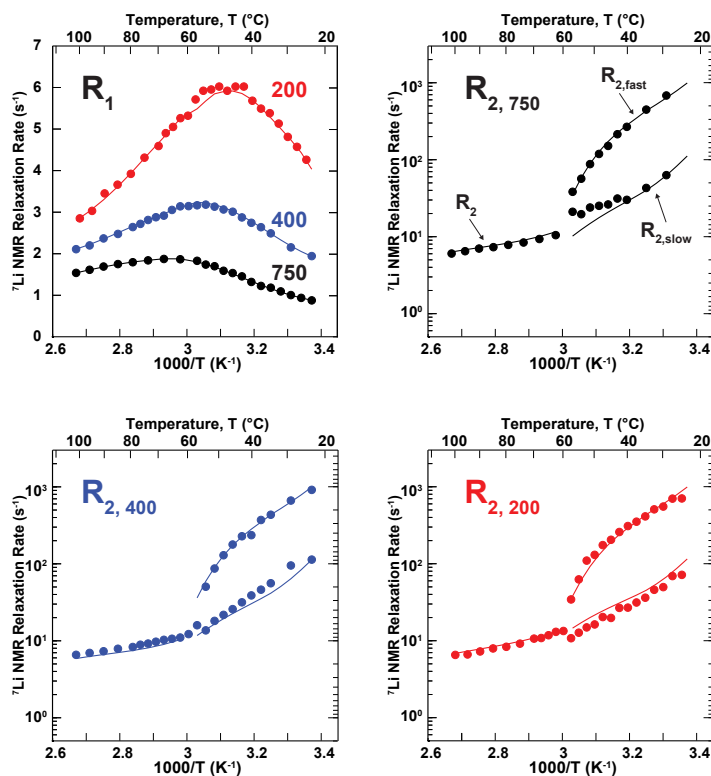


FIGURE 4.22: Fitting results of PEO(LiTFSI) by using the new relaxation model with $\langle C_Q \rangle$ variation and dipolar relaxation term at all temperatures.

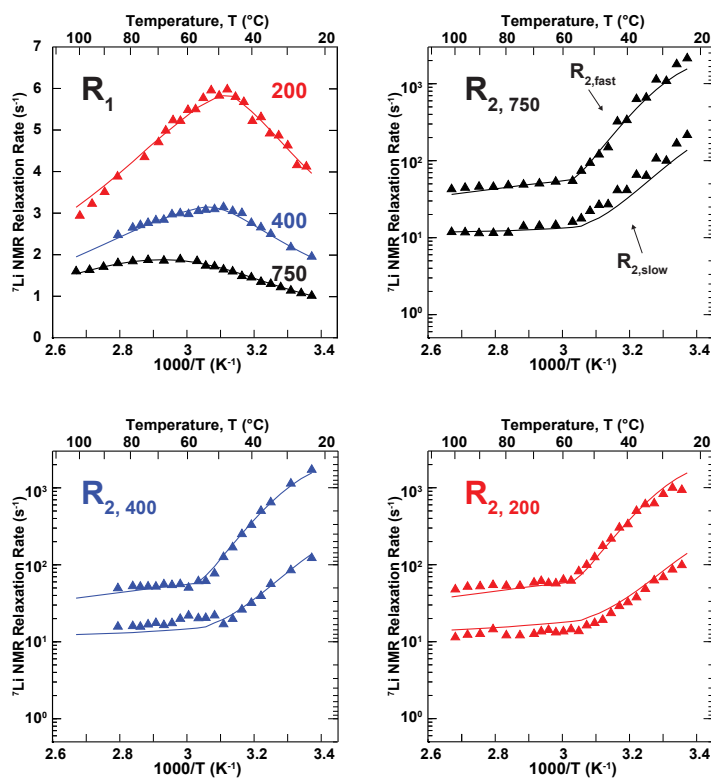


FIGURE 4.23: Fitting results of PS-PEO(LiTFSI)-PS by using the new relaxation model with $\langle C_Q \rangle$ variation and dipolar relaxation term at all temperatures.

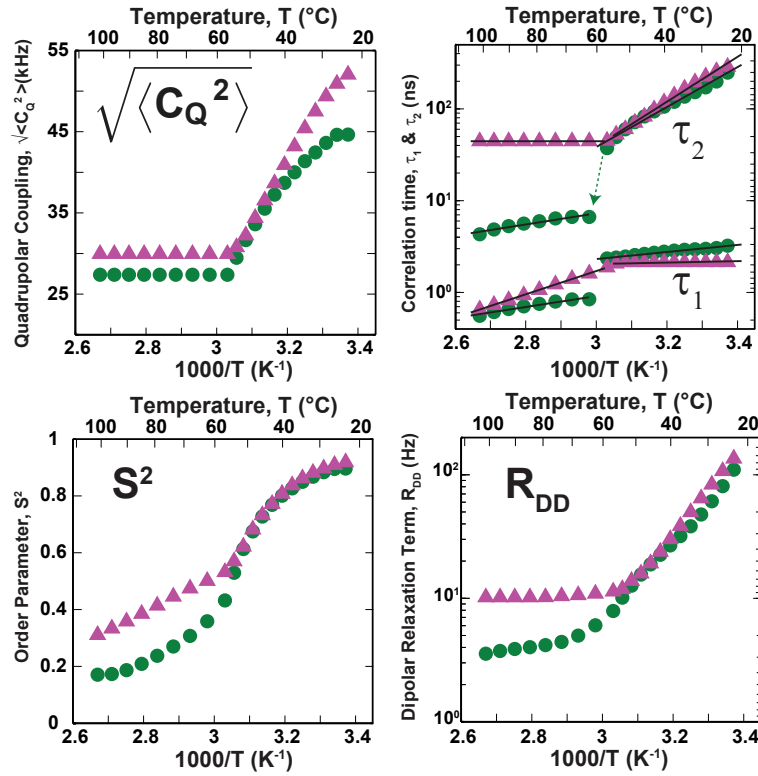


FIGURE 4.24: The parameters $\sqrt{\langle C_Q^2 \rangle}$, τ_1 and τ_2 , S^2 and R_{DD} fitted from the measured relaxation rates in PEO(LiTFSI)(●) and PS-PEO(LiTFSI)-PS(▲). The lines are guides for the eyes, and the activation energies (see table 4.2) were calculated for τ_1 and τ_2 using an Arrhenius law.

4.23, the relaxation rates obtained by adjusting the $\langle C_Q^2 \rangle$, τ_1 , τ_2 , S^2 and R_{DD} parameters (numerical results shown in appendix A) are shown as lines and fit very well with the experimental data.

TABLE 4.2: Activation energy calculated (kJ/mol) for τ_1 and τ_2 using an Arrhenius law.

	PEO(LiTFSI)		PS-PEO(LiTFSI)-PS	
	τ_1	τ_2	τ_1	τ_2
Below T_M	7.37 ± 0.31	41.71 ± 1.65	1.51 ± 0.70	46.80 ± 0.87
Above T_M	11.40 ± 0.95	11.63 ± 1.27	24.32 ± 0.12	0

Below the melting temperature, $\sqrt{\langle C_Q^2 \rangle}$ decreases as the temperature increases for both PEO and PS-PEO(LiTFSI)-PS, reflecting the increase in the amplitude

of fast motions as the temperature rises. Above the melting temperature, the decrease of $\sqrt{\langle C_Q^2 \rangle}$ stops at around 27 kHz for PEO and 30 kHz for PS-PEO(LiTFSI)-PS. When the PEO phase is melted, this indicates that no further averaging of the EFG is possible over this short timescales, and no increase in the amplitude of local motions is observed. A longer time is needed to further average the EFG, and this requires another source of EFG fluctuation, i.e. most likely a change in the oxygen coordination layer or reorientation of the EFG following concerted polymer chain motions.

Such a change is expected to occur over a time corresponding to τ_1 . τ_1 is found at around 2-3 ns below the melting temperature, and decreases to 0.5-0.8 ns above the melting temperature. The τ_1 curve can easily be fitted with an Arrhenius law where $\tau = \tau_0 \exp(E_a/RT)$, providing activation energies at 7.37 kJ/mol and 11.40 kJ/mol before and after melting respectively, confirming that it is indeed a thermally activated process. The low activation energy at below the melting temperature may result from the restriction of motion imposed by the rigidity of the polymer structure below the melting temperature. Although over such timescales, the Mean Square Displacement (MSD) is supposed to follow a subdiffusive law, [92] it is interesting to compute $\sqrt{\langle R^2 \rangle}$ using a diffusive behavior, i.e.:

$$\langle R^2 \rangle = 6D\tau_c \quad (4.17)$$

where D is the diffusion coefficient we measured in the same conditions. The results are shown in figure 4.25a. In this case, the true value of $\sqrt{\langle R^2 \rangle}$ will be larger than the one computed assuming a diffusive behavior. Such a strategy cannot be applied to PEO(LiTFSI) below the melting temperature as we expect that some PEO may be crystallized and therefore, as diffusion occurs in the glassy domains, the self-diffusion coefficient is measured over 1-2 μm and therefore influenced by the tortuosity of the glass domains. Hence, D cannot be easily related to motion at smaller lengthscale. A similar problem occurs for PS-PEO(LiTFSI)-PS because of the presence of PS domains.

Fluctuations of the EFG occurring over this timescale can therefore be associated with a displacement of the Li^+ during τ_1 : $\sqrt{\langle R^2 \rangle}$ ranges between 1 and 2 \AA when calculated for τ_1 . Such a displacement could easily be observed following rearrangements of the oxygen coordination layer or reorientation of the polymers which are coordinated to Li^+ . The latter has been detected with neutron spin-echo spectrometry,[97] while the former is expected to occur over a 0.1 to 1

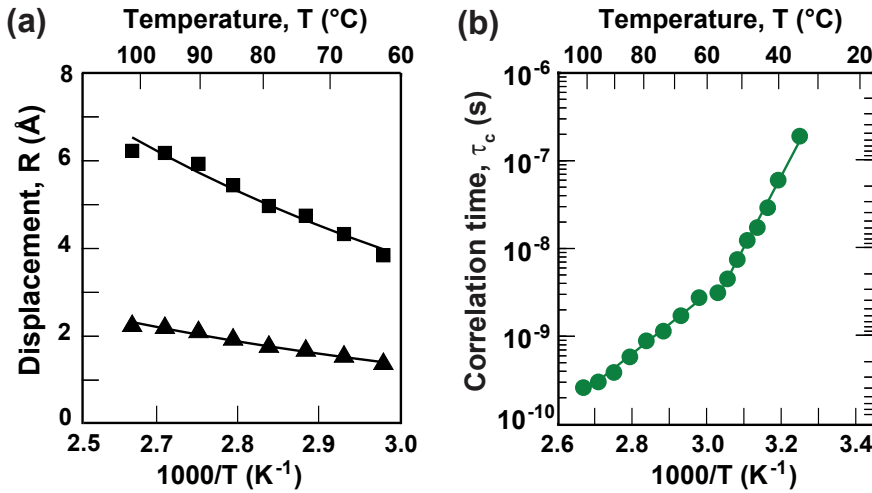


FIGURE 4.25: a. Displacement $\sqrt{\langle R^2 \rangle}$ of Li⁺ calculated from Eq. 4.17, ▲: calculated using τ_1 , ■: calculated using τ_2 ; b. The time τ_{inter} between interchain jumps for Li⁺ in PEO(LiTFSI), calculated using [93]. The lines are guides for the eyes.

ns timescale.[96] Similarly,[117] in polymer electrolyte PEO₁₀LiTFSI, the authors have shown that the hopping of Li⁺ from a cage formed by several PEO units to an alternative cage takes roughly 1 ns, and the residence time of Li⁺ within a cage is around 4-7 ns. Both phenomena are expected to be strongly correlated and both contribute to the fluctuation of the quadrupolar interaction tensor.

The results for τ_2 show a correlation time that starts at 250 ns at low temperature, decay towards 37 ns at the melting temperature with an activation energy of 41.71 kJ/mol. Above the melting temperature, in PEO(LiTFSI), the long correlation time decays sharply, down to 6.6 ns and decays to 4.3 ns at 100 °C with an activation energy of 11.63 kJ/mol. A similar calculation can be made with τ_1 , and yields $\sqrt{\langle R^2 \rangle}$ ranging between 4 to 6 Å closing to the expected length of Kuhn's segments in PEO, at 2.5 monomeric units. It would therefore make sense that the complete averaging of the EFG occurs when Li⁺ has diffused over a comparable lengthscale. Interestingly, crystal structures of PEO:LiAsF₆ complexes [118] found some lithium channels surrounded by a double PEO helix, with lithium sites separated by 4.5-5 Å distances. Although the lithium concentration is lower in our systems, it is interesting to note that such a distances could correspond well with the distance travelled by Li⁺ which had their oxygen coordination layer renewed and progress towards the next site along the double PEO helix. These studies based on molecular dynamics,[92] with polymer electrolyte PEO_nLiTFSI ($n = 7.5, 10, 20, 39$; $M_w = 2380$ g/mol) at temperatures ranging between 120 and

150 °C, the authors have pointed out by using MD simulation that the intersegmental hops in the range from 5 to 8 Å, and at lower temperature it tends to have longer intersegmental hopping length. Therefore, there is good agreement between the time and length scales we measure, and what was observed in previous studies.

Moreover, the order parameter S^2 (which describes the proportion of the quadrupolar interaction that has to be averaged over τ_2) is fairly high (0.9) at low temperature and decays fast below melting temperature. An order parameter of 0.9 corresponds to the averaging obtained by a fluctuation of $\pm 21^\circ$ amplitude of the EFG axis around its average orientation. [119] After melting, the decay slows down to 0.2 ($\pm 72^\circ$), indicating that 55% of the quadrupolar interaction is averaged during τ_1 , and the rest (45%) is averaged during τ_2 .

The comparison with PS-PEO(LiTFSI)-PS is very interesting: first, the $\sqrt{\langle C_Q^2 \rangle}$ parameter is systematically higher for PS-PEO(LiTFSI)-PS as the PS domains are crystallized over the whole temperature range, and may limit the amplitude of fast PEO segmental motions. Below the melting temperature, the S^2 parameter are similar, although after melting, S^2 measured in PS-PEO(LiTFSI)-PS has a similar decline but toward larger value (0.3 or $\pm 65^\circ$) that may be due to reduced motion caused by the rigidity induced by PS domains. The striking difference concerns τ_2 , which does not undergo the sharp decline upon melting the PEO domains, although it is similar to τ_2 measured in PEO(LiTFSI) below the melting temperature, with an activation energy of 46.80 kJ/mol. This may be linked with the fundamental difference between the PS-PEO(LiTFSI)-PS and the PEO(LiTFSI) polymers. The PEO chains in PS-PEO(LiTFSI)-PS are anchored to rigid PS chains, and therefore, these slow motions cannot be accelerated unless PS is also melted. This has a clear implication for NMR measurements: the transverse relaxation of ^7Li stays multi exponential beyond the melting of PEO domains. The short correlation time τ_1 is nearly constant at low temperatures (activation energy of 1.51 kJ/mol), which may be linked with the confinement effect: the presence of PS domains inhibits the crystallization of PEO domains in which Li^+ move inside tunnels created by parallel polymer chains,[31] so that the Li^+ motion is easier than in neat PEO. After melting, τ_1 declines with an activation energy of 24.32 kJ/mol with values close to those of PEO(LiTFSI). The dipolar coupling term is very similar in both polymers below the melting temperature, however, above the melting temperature, the dipole-dipole term shows a plateau at 10 Hz, which may be due again to the effect PS domains. Thus, it seems that the lithium motions are

constantly slowed down in PS-PEO(LiTFSI)-PS, seemingly due to the restrictions in motion imposed by the presence of rigid PS domains. This is illustrated in the correlation functions of the fluctuations of ^7Li quadrupolar interactions that are shown in figure 4.26.

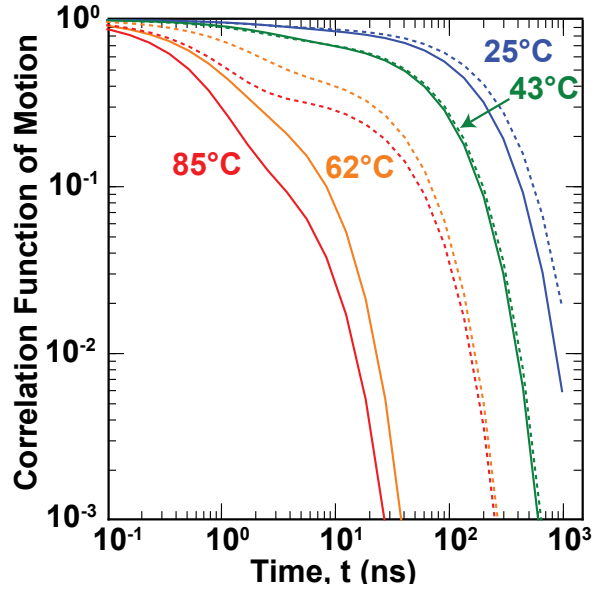


FIGURE 4.26: Correlation functions describing the fluctuations of the ^7Li quadrupolar interaction at various temperatures. The correlation function for PEO(LiTFSI) (continuous line) shows a systematically faster decay than in PS-PEO(LiTFSI)-PS (dashed line).

The dipole-dipole term slowly decays as temperature increases, and becomes very weak above the melting temperature, as expected as the mobilities of the lithium ions increase and the reorientation of CH bonds becomes faster at higher temperatures. The dipolar coupling term is very similar in both polymer below T_M , however, above T_M , the dipole-dipole term shows a plateau at 10 Hz, which may be due to again to the effect of PS domains.

Maitra et al. [93] found a relationship between the diffusion coefficient and the mean square end-to-end distance of a polymer chain R_e^2 , the correlation time τ_{intra} (Li^+ moves along one chain from head to tail), τ_{chains} (Li^+ moves cooperatively with the chains), τ_{inter} (Li^+ jumps between the chains). Figure 4.27 depicts these three different timescales. In our case, τ_{chains} is very long due to the long PEO chain. τ_{inter} can be calculated by:

$$\tau_{inter} = \frac{R_e^4}{(6\pi)^2 D^2 \tau_{intra}} \quad (4.18)$$

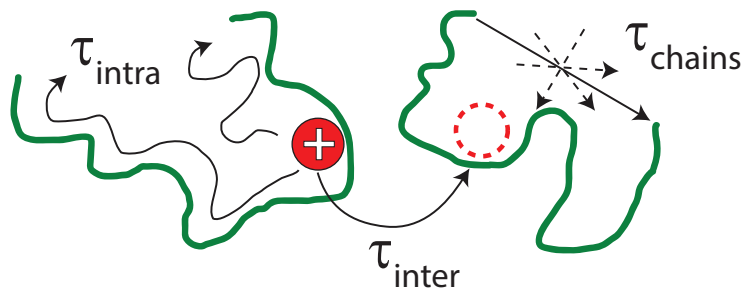


FIGURE 4.27: Three different timescales of Li^+ motion in polymers were divided by Borodin et al. [92] : τ_{intra} (Li^+ moves along one chain from head to tail), τ_{chains} (Li^+ moves cooperatively with the chains), τ_{inter} (Li^+ jumps between the chains) (figure adapted from ref [93])

where R_e^2 is $N \times L^2$ with N the number of units (2272 units), L is the distance between O-O in crystal of $(\text{G}2)_2\text{LiTFSI}$ [114] is 2.578 Å. τ_{intra} was calculated by τ_2 , because each Li^+ coordinates with 4-5 oxygens (or 4.5 in average) then the time it takes to go from head to tail is $\tau_{intra} = \frac{N^2}{4.5^2} \tau_2$. Figure 4.25b shows the τ_{inter} values calculated from equation 4.18.

Do et al. [117] have studied Li^+ transport in PEO by neutron spin-echo(NSE), dielectric spectroscopy and molecular dynamics simulation, showing the important role of the Li^+ hopping process in contributing to macroscopic conductivity.

Golodnitsky et al. [120] have proposed that the conductivity of Li^+ in PEO-based polymer electrolytes below the melting temperature may be due to 'interchain' hopping. Moreover, Maitra et al. [93] have shown that $\tau_{inter} \propto N^0$. Considering that the correlation times we measured have activation energies which are lower than the activation energy found for diffusion, it may well be possible that the limiting process for macroscopic diffusion is the inter-chain hopping motion. This could explain why spinning the sample increase the activation energy of diffusion although the relaxation properties seem unaffected by pressure. In this case, spinning the sample may change the relative orientations of polymer chains and make the inter-chain jumps more difficult.

4.4 Conclusion

The Li^+ motion were characterized by both NMR relaxation and PFG-NMR diffusion experiments. The relaxation times characterizing Li^+ motion showed that the quadrupolar interaction fluctuates at three different timescales, and for two of

them, correlation times can be extracted using a simple model for motion. The relaxation analysis clearly show that the Li^+ dynamics are slowed down in PS-PEO(LiTFSI)-PS compared to PEO(LiTFSI). From the characteristic timescale for the averaging of the quadrupolar interaction and the self-diffusion coefficients, the characteristic time τ_{inter} between interchain jumps can be estimated experimentally.

Chapter 5

Polymer electrolytes in ultra thin film battery

5.1 Introduction

In this part, we will discuss about the use of polymer electrolytes in ultra-thin battery. This project is a collaboration between the laboratory Physico Chimie de Matériaux et des Electrolytes pour l'Energie (PCM2E) in Tours and the CEMHTI laboratory.

Porous solid polymer electrolytes (PSPE) are one of the SPEs which are used in high energy batteries. [121] The ionic conductivity of PSPE mainly depends on the conductivity of the electrolyte entrapped in the pores of the membranes. [122] Microporous polymer electrolytes can feature high ionic conductivities and high mechanical strengths. [123]

PVdF (Vinylidene fluoride) and its copolymer (PVdF with hexafluoropropylene) PVdF-HFP are good candidates as battery electrolytes. Therein, PVdF-HFP has many advantages such as lower crystallinity, high solubility, lower glass transition temperature than its homogeneous counterpart PVdF. [124, 125]

Lalia et al. [126] improved the ionic conductivity by adding ionic liquids (IL) into PVdF-HFP polymers. Furthermore, IL are non-volatile, have large ionic conductivities and excellent thermal, chemical and electrochemical stabilities. [127]

In order to enhance ionic conductivity, mechanical and thermal properties of PVdF-based polymer electrolytes, polymer blends may also be used. [128] Xi et al. [129] have shown that the addition of polyoxyethylene (POE, corresponding to polymer with shorter chains than PEO) to PVdF can improve the pore configuration (pore size, pore connectivity) leading to an enhancement of their ionic conductivity. However, the mechanical strength of this polymer is lower than the one observed for pure PVdF. Chung et al. [130] added PEG to PVdF-HFP and reported that it can increase the porosity and conductivity of the PVdF-HFP network. Cheng et al. [131] designed a new polymer electrolyte based on PVdF-HFP with PEG acting like plasticizer to increase the flexibility while PEGDMA is introduced to reinforce the PVdF-HFP matrix. The combination of %wt of each polymer is crucial to control the flexibility, tensile modulus and porosity of polymer samples. Depending on the PEG:PEGDMA ratio, the mechanical strength decreases while the ionic conductivity increases.

However, the PVdF-HFP membranes show very poor retention of the liquid phase at high temperature (60 °C). POE polymers are known for their electrostatic interactions (Van der Waals) with ions. Therefore, mixing cross-linked POE with PVdF-HFP is expected to improve its retention of ionic liquid while keeping the transport properties of PVdF-HFP.

In this work, we will study the diffusion process and relaxation times of hybrid polymer electrolytes. A set of polymer electrolytes were synthesized including:

- A PVdF-HFP based electrolyte with addition of IL Pyr₁₃FSI and LiTFSI
- A PEGDM/PEGM cross-linked polymer with LiTFSI dissolved in Pyr₁₃FSI
- A mixture of PVdF-HFP and PEGM(Poly ethyleneglycol methyl ether methacrylate)/PEGDM (Poly ethyleneglycol dimethacrylate) to form a semi-interpenetrated (SRIP) network [132]

All synthesis were performed by Victor CHAUDOY in the PCM2E laboratory at the University François Rabelais of Tours.

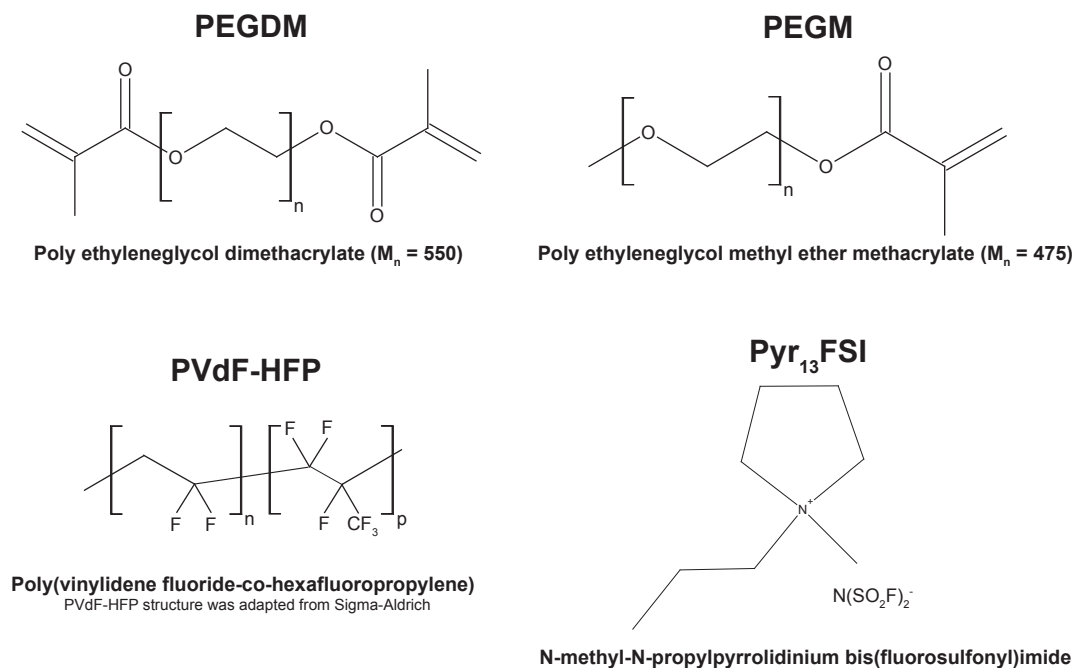


FIGURE 5.1: Molecule structure of materials used to prepare the polymer electrolytes.

5.2 Experiments

An artist's view of the structure of the PH based on linear PVdF-HFP and POE samples are shown in figures 5.2 and 5.3, respectively. In this sample, crosslinked PEGDM maintain the polymer network while the domains and pendant chains of PEGM are expected to help the flexibility of the chains and the mobility of the electrolyte species. Adding PEGM is known to lower the glass transition temperature T_g which favors higher Li^+ mobility and ionic conductivity. [133]

Figure 5.4 presents the SRIP gel polymer electrolyte. In SRIP, the PEGDM/PEGM polymer was expected to limit the syneresis (expulsion of liquid outside the polymer matrix) of PVdF-HFP. The influence of the PEGM:PEGDM ratio on diffusion coefficients in SRIP sample will be examined. The of IL was kept around 80% (% wt) for every samples. The composition of prepared samples is shown in table 5.1.

5.3 Results and discussions

Figure 5.5 shows the diffusion coefficients of cation and anion of samples in function of LiTFSI concentration in PH and SRIP(ratio PEGM:PEGDM-4:1) samples.

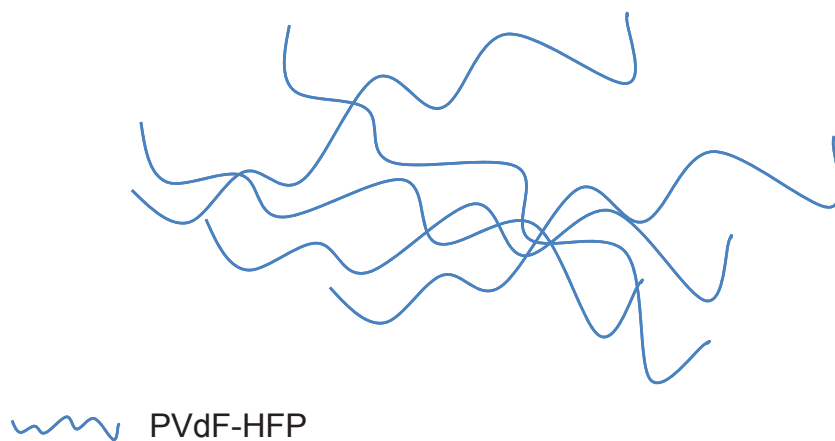


FIGURE 5.2: PH sample: only PVdF-HFP with IL PyrFSI and salt LiTFSI (©Victor Chaudoy - Université de Tours)

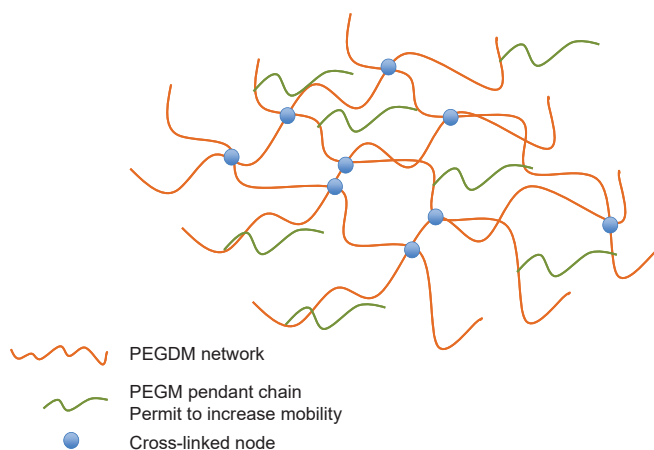


FIGURE 5.3: POE sample: PEGDM/PEGM crosslinked with IL PyrFSI and salt LiTFSI (©Victor Chaudoy - Université de Tours)

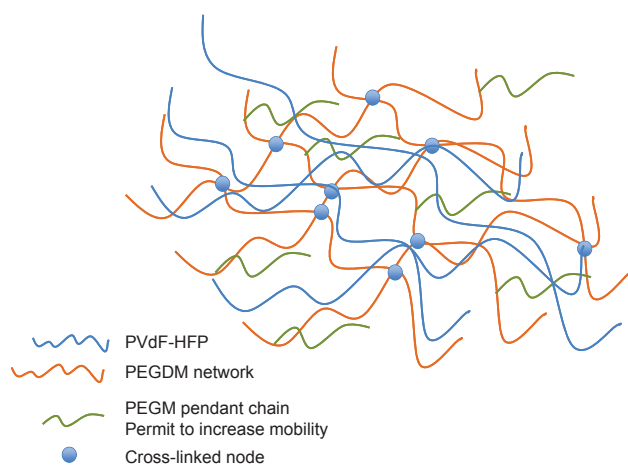


FIGURE 5.4: SRIP sample: the linear chain PVdF-HFP is tangled in network PEGM/PEGDM. There is no chemical link between PVdF-HFP and network PEGM/PEGDM (©Victor Chaudoy - Université de Tours)

TABLE 5.1: The composition of samples

Ref	Name	PVdF HFP	PEGM	PEGDM	Pyr ₁₃ FSI+LiTFSI	x
						M (mol/l)
107A	PH 1,3	20	0	0	80	1.3
109C	PH 1M	20	0	0	80	1
97C	PH 0,6M	20	0	0	80	0.6
116A	SRIP 0,6M	15	4	1	80	0.6
76F	SRIP 1M	15	4	1	80	1
109A	SRIP 1,3M	15	4	1	80	1.3
110D	SRIP 1,9M	15	4	1	80	1.9
97E	SRIP 2,8M	15	4	1	80	2.8
97F	SRIP 3,2M	15	4	1	80	3.2
109B	SRIP 1,3M4%	15	1	4	80	1.3
107F	SRIP 1,3M5%	15	0	5	80	1.3
110B	POE 1,3M	0	16	4	80	1.3

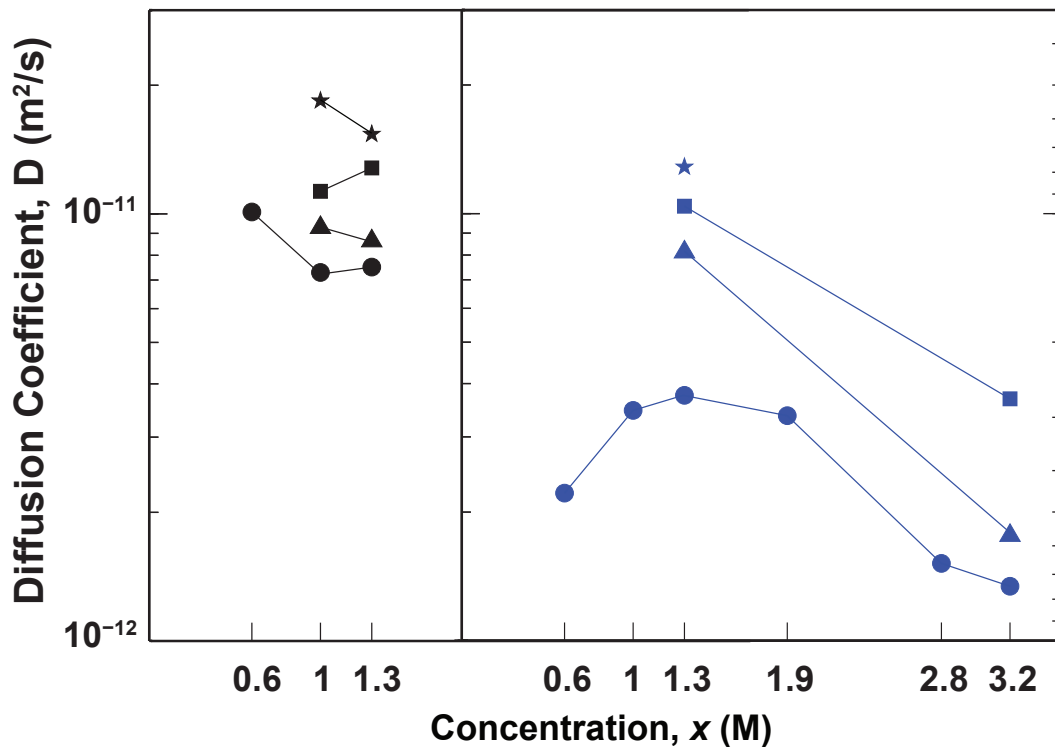


FIGURE 5.5: Diffusion coefficients of Li^+ (●), Pyr_{13}^+ (■), TFSI^- (▲) and FSI^- (★) of PH (left), SRIP (right) as a function of LiTFSI concentration x (M). The lines were guided for eyes

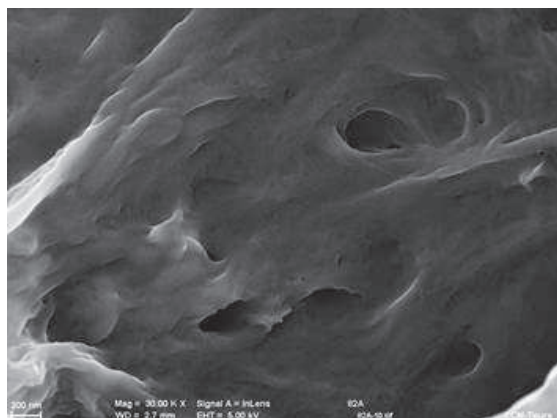


FIGURE 5.6: SEM micrographs of the PVdF-HFP membrane (PH sample without IL and LiTFSI)

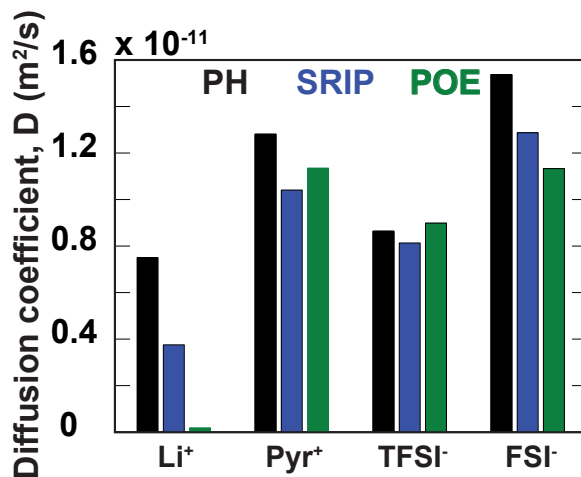
In the PH samples, the self-diffusion coefficients of Li^+ decrease with the LiTFSI concentration from 0.6 to 1.3 M when diffusion coefficients of Pyr_{13}^+ slightly increase from 1 to 1.3 M. On the other hand, diffusion coefficients of TFSI^- and FSI^- slightly decrease with increasing concentrations of LiTFSI (from 1 to 1.3 M) in the PH samples. Figure 5.6 shows the SEM micrographs of PH samples, the porous structure is easily seen. Therefore, the IL can swell inside these pores leading to a high conductivity.

FSI^- has the highest diffusion coefficient followed by Pyr_{13}^+ and TFSI^- . Li^+ is the slowest, regardless of its size as Li^+ are coordinated to FSI^- and/or TFSI^- anions which slow its diffusion to a larger extent than Pyr_{13}^+ . [134] Moreover, TFSI^- is bulkier than FSI^- [135], explaining why TFSI^- diffuses slower than FSI^- . Furthermore, as Li^+ tends to be coordinated to anions, an increase in Li^+ concentration leads to an increase in the self-diffusion coefficient of Pyr_{13}^+ and in the viscosity of the solution, while the diffusion coefficients of Li^+ , FSI^- and TFSI^- decrease. [134] It should be noted that the quantity of ionic liquid is also important for the diffusion of species. The increase of LiTFSI concentration leads to the decrease of quantity of ionic liquid because the % wt of $\text{Pyr}_{13}\text{FSI} + \text{LiTFSI}$ was kept the same for every samples. Therefore, the decrease of diffusion coefficients of species must be considered to result from several causes.

In the SRIP samples, the self-diffusion coefficient of Li^+ reaches its maximum for a LiTFSI concentration of 1.3 M. This is in contrast with the PH samples (over the LiTFSI concentration range 0.6-1.3 M). It may be explained by the presence of POE. When one adds POE, part of the Li^+ can be coordinated by the oxygen atoms of the POE part (see table 5.2 for the number of available oxygens

TABLE 5.2: Ratio of oxygen/Li in samples containing POE

Ref	Name	Total Oxygen	PEGM	PEGDM	D_{Li^+} (m^2/s)
116A	SRIP 0,6M	3.30	2.59	0.71	2.22×10^{-12}
76F	SRIP 1M	1.98	1.56	0.42	3.46×10^{-12}
109A	SRIP 1,3M	1.52	1.20	0.33	3.75×10^{-12}
110D	SRIP 1,9M	1.04	0.82	0.22	3.36×10^{-12}
97E	SRIP 2,8M	0.71	0.56	0.15	1.52×10^{-12}
97F	SRIP 3,2M	0.62	0.49	0.13	1.34×10^{-12}
109B	SRIP 1,3M4%	1.60	0.30	1.30	3.70×10^{-12}
107F	SRIP 1,3M5%	1.63	0	1.63	3.76×10^{-12}
110B	POE 1,3M	6.09	4.78	1.30	1.89×10^{-13}

FIGURE 5.7: Diffusion coefficients of Li^+ , Pyr_{13}^+ , $TFSI^-$, FSI^- of PH, SRIP and POE with a concentration of $LiTFSI$ of 1.3M

per lithium atoms). Therefore, for low Li^+ concentrations, most of the ions are bound to POE, and slowed down. Adding more lithium increase the amount of free Li^+ ions which can diffuse through the ionic liquid phase, even if the system becomes more viscous. However, when $LiTFSI$ concentration increase more than 1.3 M, the viscosity of ionic liquid increases sufficiently, leading to decreasing self-diffusion coefficients for Li^+ , Pyr_{13}^+ and $TFSI^-$. Furthermore, the quantity of ionic liquid $Pyr_{13}FSI$ also decreases and may affect the self-diffusion of these species. To compare the diffusion coefficients of the electrolyte species, we fixed the $LiTFSI$ concentration at 1.3 M.

In figure 5.7, we can observe that Li^+ diffuses the fastest in the PH sample, then in SRIP and has the slowest diffusion in POE. The diffusion coefficients of Pyr_{13}^+ and of the anions are slightly different for the three samples. As stated above, the

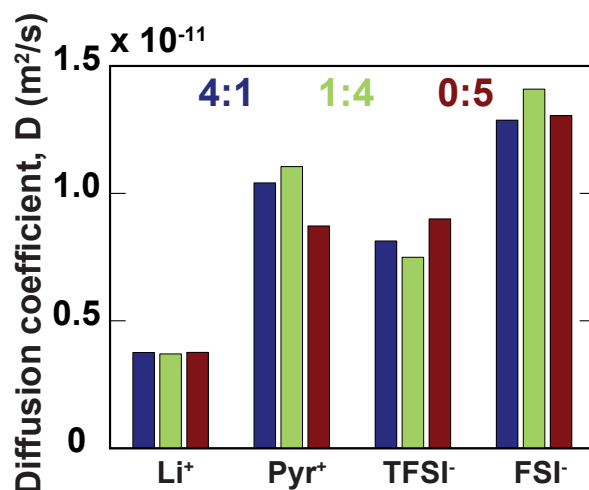


FIGURE 5.8: Diffusion coefficients of Li^+ , Pyr_{13}^+ , TFSI^- and FSI^- in SRIP samples with difference ratio of PEGM:PEGDM (4:1, 1:4, 0:5) with an LiTFSI concentration 1.3 M

largest diffusion coefficient for Li^+ is found in the PH sample, as expected as Li^+ ions are only coordinated to the anions of the ionic liquid. The higher diffusion coefficient of Li^+ in SRIP than in POE can be explained by the presence of a porous structure. The IL can swell in the pores where Li^+ can diffuse easier than the case of POE.

The self-diffusion coefficients dependence upon the PEGM:PEGDM ratio in SRIP samples is shown in figure 5.8. The PEGM:PEGDM ratio does not seem to have much influence on the Li^+ diffusion coefficients in the SRIP samples, while the diffusion coefficients of Pyr_{13}^+ and anions variate slightly. This observation is in contradiction to what was expected: increasing the PEGM:PEGDM ratio was supposed to improve the mobility of Li^+ . Therefore, we can infer that Li^+ is coordinated to oxygens of the PEGDM network and that adding PEGM decreased the glass transition temperature but do not favor the mobility of Li^+ .

The ^7Li longitudinal and transverse relaxation rates of these samples are shown in figures 5.9, 5.10, respectively. On the one hand, we observed the mono-exponential behavior of longitudinal relaxation while transverse relaxation is bi-exponential (with a 60/40 ratio between the two exponentials) in both SRIP and POE samples. On the other hand, both transverse and longitudinal relaxations are mono-exponential in the PH samples.

As shown in chapter 4, the bi-exponentiality of ^7Li transverse relaxation is found in POE(LiTFSI) below the melting temperature.

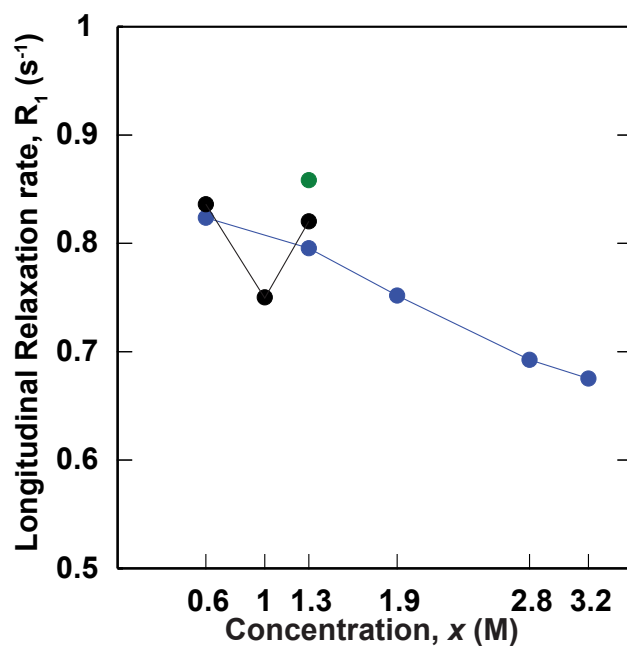


FIGURE 5.9: ^7Li longitudinal relaxation rates of PH, SRIP(PEGM:PEGDM-4:1) and POE samples as a function of the LiTFSI concentration. The lines were guided for eyes.

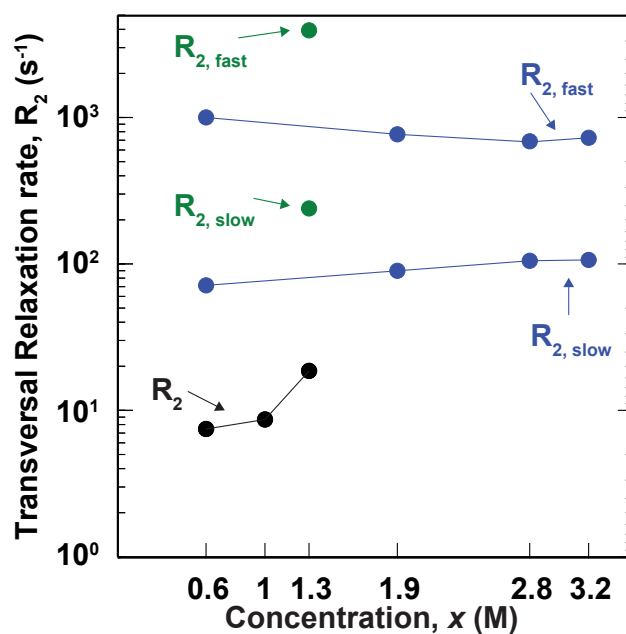


FIGURE 5.10: ^7Li transverse relaxation rates of PH, SRIP(PEGM:PEGDM-4:1) and POE samples as a function of the LiTFSI concentration. The lines were guided for eyes.

Therefore, it seems that the local environment of Li^+ is modified when adding PEGDM/PEGM into the PH sample, leading, not only to a decrease of the diffusion coefficient, but also to an increase of the correlation times of the fluctuation of the Li^+ quadrupolar interaction (less mobility at the atomic scale), confirming the presence of interactions between Li^+ and the oxygen atoms of the POE fragments.

5.4 Conclusions

The study of self-diffusion coefficients of electrolyte species provided us with interesting results. The presence of oxygen atoms lead to the coordination of Li^+ to them and slowed their diffusion down. In the SRIP samples, the presence of a porous structure improved the self-diffusion coefficients of Li^+ compared to the POE samples while the Pyr_{13}^+ cation and the anions were not strongly influenced. Adding PEGM/PEGDM to PVdF-HFP (SRIP sample) decreased the self-diffusion coefficient of Li^+ by 20 % compared to the original PH sample. Moreover, the ratio PEGM:PEGDM has no influence on the diffusion coefficient of Li^+ in the SRIP samples.

The lower diffusion results from coordination effects at the atomic scale, as the change in relaxation rates of Li^+ show an increase in the correlation times of the fluctuations of the Li^+ environment when POE domains are added. This is clearly seen as transverse relaxation becomes bi-exponential in the POE and SRIP samples, and confirms what was inferred from the lower conductivities and the worse battery performance.

Chapter 6

Conclusions and Perspectives

6.1 Conclusions

Solid polymer electrolytes are strong candidates for lithium-metal batteries regardless their low ionic conductivities. NMR is very useful for the characterization of SPEs as it gives the possibility to look at diffusion coefficients at the micron scale, and at the microscopic motion of Li^+ through high-field relaxometry. Although MAS has many advantages, like reducing the residual dipole-dipole interactions and susceptibility effects, leading to better resolution, increased sensitivity, and more homogeneous field gradients, it has some serious side effects due to the centrifugal forces. Although lithium motion at the nanoscale seems unaffected, the diffusion process seems to be altered by the applied pressure.

Microscopic motion of Li^+ was then studied by a high-field relaxometry approach. Using a "model-free" approach, two timescales are detected for the Li^+ motion, linked with changes in the coordination layer and with the complete averaging of the quadrupolar interaction, both at the nanosecond timescale, and corresponding to mean-square displacement over 2-6 Å. Other models failed to reproduce the data.

Two polymer electrolytes, PEO(LiTFSI) and PS-PEO(LiTFSI)-PS were studied by diffusion and relaxation. The phase-separated PS-PEO(LiTFSI)-PS has a slower diffusion, mainly because of the tortuosity of the PEO phase. However, relaxation rates showed that the presence of PS chains attached at each end of the

PEO chain tend to slow the motion of Li^+ at the nanosecond timescale. Therefore, assuming that the motion of Li^+ in PEO(LiTFSI) and in the PEO domains of PS-PEO(LiTFSI)-PS are similar at the atomic level may be wrong. This has deep implications for the design of block-copolymer electrolytes.

The diffusion and relaxation properties of thin film polymer electrolytes based on PVdF-HFP were also investigated. Introducing a PEGDM/PEGM network inside the porosity of PVdF-HFP increase the retention of ionic liquids, however, it also slows Li^+ diffusion down, mainly because Li^+ interacts with the oxygen atoms of these polymer chains.

6.2 Perspectives

Three main perspectives can be considered:

1. Molecular dynamics: First, the understanding of Li^+ motion could be enhanced by using molecular dynamics (MD) trajectories to retrieve relaxation properties of ^7Li , and check if an agreement can be reached between the NMR relaxation rates and the motion depicted by MD.
2. New samples, new experiments: Other samples could benefit from the relaxation and diffusion analysis, in particular, PSTFSiLi-PEO-PSTFSiLi is currently being analyzed in a similar manner. Moreover, the existence of a "dead zone" close to the PS domains could be probed by NMR correlation experiments.
3. Magnetic Resonance Imaging (MRI): In situ analysis of the concentration profiles can be measured by NMR imaging techniques, and would provide interesting information about the mobility of ions inside an electric field.

Appendix A

Experimental relaxation rates and calculated parameters

A.1 Calculation method

In this section, we will explain how the calculations were performed at each temperature points simultaneously for three different magnetic fields. For each magnetic field, the relaxation rates were measured at various temperatures between 25 and 100°C. As the temperatures are not exactly the same for each spectrometer, we modelled the data with a polynomial curve to interpolated the experimental data and obtain for each field, the relaxation rates at exactly the same temperature.

The equations of relaxation rates were shown in Chapter 4. The parameters were varied to minimize the difference between experimental relaxation rates at each field and their calculated values using a χ^2 minimization method in Maple:

$$\chi^2 = a \sum_i \left(\frac{R_1(cal) - R_1(exp, i)}{R_1(exp, i)} \right)^2 + \sum_i \left(\frac{R_{2,fast}(cal) - R_{2,fast}(exp, i)}{R_{2,fast}(exp, i)} \right)^2 + \sum_i \left(\frac{R_{2,slow}(cal) - R_{2,slow}(exp, i)}{R_{2,slow}(exp, i)} \right)^2 \quad (\text{A.1})$$

where a is a weighting parameter fo ensure the fit is correct. The additional a term compensate the large difference of R_1 and R_2 values which leads to the local χ^2 minima (see tables A.1 and A.2). In our case, a was set to 10. Equation A.1

was used for the case of PS-PEO(LiTFSI)-PS at all temperature points and for PEO(LiTFSI) below the melting temperature, while equation A.2 was used for PEO(LiTFSI) above the melting temperature. i stand for the magnetic field and takes the following values 4.7 (200 MHz for ^1H), 9.4 (400 MHz for ^1H) and 17.6 T (750 MHz for ^1H).

$$\chi = a \sum_i \left(\frac{R_1(\text{cal}) - R_1(\text{exp}, i)}{R_1(\text{exp}, i)} \right)^2 + \sum_i \left(\frac{R_2(\text{cal}) - R_2(\text{exp}, i)}{R_2(\text{exp}, i)} \right)^2 \quad (\text{A.2})$$

A.2 Experimental relaxation rates

The longitudinal and transversal relaxation rates are shown in tables A.1 for PEO(LiTFSI) and A.2 for PS-PEO(LiTFSI)-PS.

TABLE A.1: ${}^7\text{Li}$ relaxation rates (s^{-1}) of PEO, where the unit for $1000/T$ is (K^{-1})

$1000/T$	$R_{1,750}$	$1000/T$	$R_{1,400}$	$1000/T$	$R_{1,200}$	$1000/T$	$R_{2,slow,750}$	$R_{2,fast,750}$	$R_{2,750}$	$1000/T$	$R_{2,slow,400}$	$R_{2,fast,400}$	$R_{2,400}$	$1000/T$	$R_{2,slow,200}$	$R_{2,fast,200}$	$R_{2,200}$
3.372	0.876	3.372	1.942	3.356	4.260	3.310	62.786	679.569		3.372	113.000	909.000		3.356	71.625	704.176	
3.340	0.936	3.310	2.152	3.328	4.570	3.250	42.847	446.309		3.310	94.859	660.946		3.328	69.105	700.378	
3.310	1.004	3.250	2.489	3.300	4.810	3.192	30.032	266.386		3.250	55.741	432.526		3.300	49.675	551.846	
3.279	1.092	3.221	2.637	3.273	5.130	3.164	31.212	213.610		3.221	46.045	369.549		3.273	45.846	507.949	
3.250	1.182	3.192	2.743	3.247	5.380	3.136	26.152	150.664		3.192	38.751	234.852		3.247	36.189	411.435	
3.221	1.224	3.164	2.872	3.221	5.490	3.109	25.142	118.464		3.164	31.526	227.169		3.221	31.345	351.335	
3.192	1.320	3.136	3.009	3.195	5.680	3.082	23.865	87.418		3.136	25.691	177.368		3.195	26.903	308.567	
3.164	1.454	3.109	3.064	3.170	6.020	3.056	19.557	56.491		3.109	21.638	128.833		3.170	26.697	257.945	
3.136	1.534	3.082	3.131	3.145	6.020	3.030	21.021	38.201		3.082	18.083	86.580		3.145	19.769	204.456	
3.109	1.589	3.056	3.180	3.120	5.920	2.980			10.455	3.056	13.635	50.251		3.120	20.296	174.483	
3.082	1.698	3.030	3.164	3.096	6.020	2.931			9.312	3.030			15.883	3.096	16.277	130.429	
3.056	1.738	3.005	3.145	3.072	5.950	2.884			8.384	3.005			12.189	3.072	14.890	109.795	
3.030	1.828	2.980	3.139	3.049	5.920	2.839			7.807	2.980			11.001	3.049	12.711	62.610	
2.980	1.865	2.956	3.053	3.026	5.710	2.794			7.295	2.955			10.597	3.026	10.769	34.339	
2.931	1.872	2.931	2.916	3.003	5.320	2.752			6.998	2.931			10.261	3.003			13.382
2.884	1.839	2.908	2.877	2.981	5.260	2.710			6.465	2.908			9.702	2.981			13.046
2.839	1.794	2.884	2.811	2.959	5.050	2.670			6.028	2.884			9.187	2.959			11.774
2.794	1.750	2.861	2.717	2.937	4.900					2.861			8.872	2.937			10.838
2.752	1.690	2.839	2.641	2.915	4.590					2.839			8.280	2.915			10.640
2.710	1.612	2.795	2.475	2.874	4.310					2.794			7.862	2.874			9.160
2.670	1.538	2.752	2.367	2.833	3.920					2.752			7.296	2.833			8.341
		2.710	2.199	2.793	3.660					2.710			6.939	2.793			7.933
		2.670	2.108	2.755	3.450					2.670			6.557	2.755			7.258
				2.717	3.030									2.717			6.626
				2.681	2.850									2.681			6.538

TABLE A.2: ${}^7\text{Li}$ relaxation rates (s^{-1}) of PS-PEO(LiTFSI)-PS, where the unit for $1000/T$ is (K^{-1})

$1000/T$	R_1750	$1000/T$	R_1400	$1000/T$	R_1200	$1000/T$	$R_{2,slow}750$	$R_{2,fast}750$	$1000/T$	$R_{2,slow}400$	$R_{2,fast}400$	$1000/T$	$R_{2,slow}200$	$R_{2,fast}200$
3.372	1.011	3.372	1.952	3.356	4.121	3.372	215.117	2127.868	3.372	122.100	1709.402	3.356	98.700	936.000
3.340	1.073	3.310	2.176	3.328	4.154	3.340	166.667	1784.446	3.310	84.746	1129.944	3.328	86.500	998.000
3.310	1.135	3.250	2.497	3.300	4.628	3.310	99.681	1079.805	3.250	56.180	645.161	3.300	68.800	828.000
3.279	1.216	3.221	2.657	3.273	4.868	3.279	106.273	1127.040	3.221	39.216	500.000	3.273	62.500	626.000
3.250	1.296	3.192	2.762	3.247	4.916	3.250	63.452	657.412	3.192	31.847	328.947	3.247	48.400	609.000
3.221	1.345	3.164	3.000	3.221	5.308	3.221	65.405	630.146	3.164	26.110	249.377	3.221	37.700	499.000
3.192	1.451	3.136	3.049	3.195	5.217	3.192	41.333	335.503	3.136	19.763	167.785	3.195	32.500	335.000
3.164	1.485	3.109	3.145	3.170	5.672	3.164	41.225	322.079	3.109	16.835	125.471	3.170	29.000	303.000
3.136	1.595	3.082	3.094	3.145	5.795	3.136	27.013	148.640	3.082	21.930	76.923	3.145	23.500	218.000
3.109	1.643	3.056	3.080	3.120	5.975	3.109	26.564	119.992	3.056	20.367	61.350	3.120	19.200	175.000
3.082	1.718	3.034	3.049	3.096	5.826	3.082	22.154	93.500	3.034	20.161	60.976	3.096	17.500	125.000
3.056	1.735	3.005	2.976	3.072	5.953	3.056	17.700	73.669	3.005	21.866	50.251	3.072	16.300	99.400
3.030	1.845	2.980	2.994	3.049	5.767	3.030	16.029	54.435	2.980	19.802	55.866	3.049	13.700	82.200
2.980	1.885	2.956	2.968	3.026	5.498	2.980	14.580	53.286	2.955	17.391	54.348	3.026	14.500	62.000
2.931	1.856	2.931	2.839	3.003	5.482	2.931	14.228	50.398	2.931	16.420	55.556	3.003	13.600	63.800
2.884	1.871	2.908	2.825	2.981	5.218	2.884	13.995	48.768	2.908	17.500	51.900	2.981	13.200	57.100
2.839	1.842	2.884	2.763	2.959	5.234	2.839	11.575	47.668	2.884	16.722	52.083	2.959	14.200	57.700
2.794	1.796	2.861	2.710	2.937	4.985	2.794	11.478	45.508	2.861	15.649	51.813	2.937	13.600	61.400
2.752	1.707	2.839	2.650	2.915	4.706	2.752	11.400	45.840	2.839	15.949	52.632	2.915	12.600	58.500
2.710	1.632	2.795	2.472	2.874	4.347	2.710	11.692	44.369	2.794	15.699	49.505	2.874	12.100	53.100
2.670	1.598			2.793	3.879	2.670	11.811	42.510				2.833	12.100	53.200
				2.755	3.508							2.793	14.500	54.400
				2.717	3.225							2.755	12.600	52.400
				2.681	2.937							2.717	12.300	51.700
												2.681	11.400	47.700

A.3 The parameters calculated from successful model

The parameters are calculated from the model presented in chapter [4](#), as seen in table [A.3](#).

TABLE A.3: Parameters of PEO(LiTFSI) and PS-PEO(LiTFSI)-PS calculated from successful model

PEO(LiTFSI)							PS-PEO(LiTFSI)-PS				
1000/T (K ⁻¹)	$\sqrt{\langle C_Q^2 \rangle}$ (kHz)	τ_1 (ns)	τ_2 (ns)	τ_{inter} (ns)	S^2	R_{DD} (Hz)	$\sqrt{\langle C_Q^2 \rangle}$ (kHz)	τ_1 (ns)	τ_2 (ns)	S^2	R_{DD} (Hz)
3.372	44.643	3.227	248.436		0.896	109.987	52.037	2.141	288.214	0.919	135.294
3.340	44.615	3.048	198.899		0.895	80.948	50.913	2.141	257.928	0.909	107.229
3.310	43.625	2.987	171.666		0.884	60.997	49.357	2.141	226.067	0.897	83.439
3.279	42.446	2.956	151.968		0.868	47.712	47.500	2.141	195.172	0.881	64.511
3.250	41.370	2.918	136.115	1902.483	0.849	38.302	45.423	2.141	166.500	0.862	49.835
3.221	39.997	2.857	119.424		0.826	31.906	43.201	2.141	140.718	0.838	38.615
3.192	38.704	2.784	105.810	600.826	0.801	26.785	40.915	2.141	118.181	0.808	30.143
3.164	37.248	2.708	93.916	291.404	0.769	22.508	38.654	2.141	99.027	0.772	23.832
3.136	35.526	2.633	82.803	173.101	0.727	18.816	36.555	2.141	82.645	0.732	19.185
3.109	33.604	2.553	71.746	123.610	0.675	15.557	34.394	2.141	70.817	0.682	15.884
3.082	31.649	2.460	59.977	74.882	0.613	12.640	32.234	2.141	60.344	0.622	13.853
3.056	29.480	2.397	49.287	45.035	0.530	10.116	30.780	2.066	52.553	0.570	11.875
3.030	27.388	2.343	37.399	31.280	0.432	7.893	29.951	1.876	45.045	0.532	11.356
2.980	27.388	0.843	6.644	27.531	0.359	6.039	29.951	1.608	44.440	0.501	10.901
2.931	27.388	0.839	6.644	17.154	0.307	4.983	29.951	1.406	44.440	0.474	10.610
2.884	27.388	0.796	6.412	11.433	0.270	4.429	29.951	1.226	44.440	0.446	10.414
2.839	27.388	0.750	5.971	8.882	0.237	4.177	29.951	1.065	44.440	0.414	10.220
2.794	27.388	0.705	5.626	5.818	0.209	4.017	29.951	0.934	44.440	0.385	10.194
2.752	27.388	0.659	5.280	3.870	0.187	3.886	29.951	0.825	44.440	0.358	10.194
2.710	27.388	0.610	4.855	3.022	0.173	3.744	29.951	0.733	44.440	0.333	10.194
2.670	27.388	0.556	4.306	2.599	0.171	3.558	29.951	0.654	44.440	0.311	10.194

Bibliography

- [1] M. Singh, O. Odusanya, G. M. Wilmes, H. B. Eitouni, E. D. Gomez, A. J. Patel, V. L. Chen, M. J. Park, P. Fragouli, H. Iatrou, N. Hadjichristidis, D. Cookson, and N. P. Balsara, *Macromolecules* **40**, 4578 (2007).
- [2] S. Arumugam, J. Shi, D. P. Tunstall, and C. A. Vincent, *Journal of Physics: Condensed Matter* **5**, 153 (1993).
- [3] M. Kitamura, Y. Hata, H. Yasuoka, T. Kurotsu, and A. Asano, *Polymer Journal* **44**, 778 (2012).
- [4] A. Panday, S. Mullin, E. D. Gomez, N. Wanakule, V. L. Chen, A. Hexemer, J. Pople, and N. P. Balsara, *Macromolecules* **42**, 4632 (2009).
- [5] R. Bouchet, S. Maria, R. Meziane, A. Aboulaich, L. Lienafa, J.-P. Bonnet, T. N. T. Phan, D. Bertin, D. Gigmes, D. Devaux, R. Denoyel, and M. Armand, *Nature Materials* **12**, 452 (2013).
- [6] M. S. Whittingham, *Proceedings of the IEEE* **100**, 1518 (2012).
- [7] J. Qian, W. A. Henderson, W. Xu, P. Bhattacharya, M. Engelhard, O. Borodin, and J.-G. Zhang, *Nature Communications* **6**, 6362 (2015).
- [8] W. Xu, J. Wang, F. Ding, X. Chen, E. Nasybulin, Y. Zhang, and J.-G. Zhang, *Energy & Environmental Science* **7**, 513 (2014).
- [9] M. Dollé, L. Sannier, B. Beaudoin, M. Trentin, and J.-M. Tarascon, *Electrochemical and Solid-State Letters* **5**, A286 (2002).
- [10] N. Dudney and B. Neudecker, *Current Opinion in Solid State and Materials Science* **4**, 479 (1999).
- [11] N. J. Dudney, *The Electrochemical Society Interface* **17**, 44 (2008).

- [12] A. Patil, V. Patil, D. W. Shin, J.-W. Choi, D.-S. Paik, and S.-J. Yoon, *Materials Research Bulletin* **43**, 1913 (2008).
- [13] J. Bates, N. Dudney, B. Neudecker, A. Ueda, and C. Evans, *Solid State Ionics* **135**, 33 (2000).
- [14] N. Dudney, J. Bates, and B. Neudecker, in *Encyclopedia of Materials: Science and Technology* (Elsevier BV, 2001) pp. 9302–9306.
- [15] N. J. Dudney, *Materials Science and Engineering: B* **116**, 245 (2005).
- [16] J. Bates, N. Dudney, G. Gruzalski, R. Zuhr, A. Choudhury, C. Luck, and J. Robertson, *Journal of Power Sources* **43**, 103 (1993).
- [17] X. Yu, J. Bates, G. Jellison, and F. Hart, *Journal of The Electrochemical Society* **144**, 524 (1997).
- [18] M. Liu, S. J. Visco, and L. C. De Jonghe, *Journal of The Electrochemical Society* **138**, 1891 (1991).
- [19] P. E. Trapa, B. Huang, Y.-Y. Won, D. R. Sadoway, and A. M. Mayes, *Electrochemical and Solid-State Letters* **5**, A85 (2002).
- [20] P. E. Trapa, M. H. Acar, D. R. Sadoway, and A. M. Mayes, *Journal of The Electrochemical Society* **152**, A2281 (2005).
- [21] D. Fenton, J. Parker, and P. Wright, *Polymer* **14**, 589 (1973).
- [22] M. Armand, J. Chabagno, and M. Duclot, *Fast ion transport in solids*, edited by P. Vashishta, J. Mundy, and G. Shenoy (North Holland, Amsterdam, 1979).
- [23] J.-M. Tarascon and M. Armand, *Nature* **414**, 359 (2001).
- [24] J.-H. Shin, W. A. Henderson, and S. Passerini, *Journal of The Electrochemical Society* **152**, A978 (2005).
- [25] R. Agrawal and G. Pandey, *Journal of Physics D: Applied Physics* **41**, 223001 (2008).
- [26] F. Gray and M. Armand, in *Handbook of Battery Materials* (Wiley-Blackwell, 2011) pp. 627–656.

- [27] S. D. Druger, A. Nitzan, and M. A. Ratner, *The Journal of Chemical Physics* **79**, 3133 (1983).
- [28] M. A. Ratner and D. F. Shriver, *Chemical Reviews* **88**, 109 (1988).
- [29] C. Berthier, W. Gorecki, M. Minier, M. Armand, J. Chabagno, and P. Rigaud, *Solid State Ionics* **11**, 91 (1983).
- [30] B.-K. Choi and Y.-W. Kim, *Electrochimica Acta* **49**, 2307 (2004).
- [31] Z. Gadjourova, Y. G. Andreev, D. P. Tunstall, and P. G. Bruce, *Nature* **412**, 520 (2001).
- [32] D. Golodnitsky, E. Livshits, Y. Rosenberg, I. Lapides, and E. Peled, *Solid State Ionics* **147**, 265 (2002).
- [33] M. Marzantowicz, J. Dygas, F. Krok, Z. Florjańczyk, and E. Zygadło-Monikowska, *Electrochimica Acta* **53**, 1518 (2007).
- [34] K. Nagaoka, H. Naruse, I. Shinohara, and M. Watanabe, *Journal of Polymer Science: Polymer Letters Edition* **22**, 659 (1984).
- [35] J. L. Souquet, M. Levy, and M. Duclot, *Solid State Ionics* **70**, 337 (1994).
- [36] J. Shi and C. A. Vincent, *Solid State Ionics* **60**, 11 (1993).
- [37] J.-F. L. Nest, A. Gandini, and H. Cheradame, *British Polymer Journal* **20**, 253 (1988).
- [38] W. H. Meyer, *Advanced Materials* **10**, 439 (1998).
- [39] U. Lauter, W. H. Meyer, and G. Wegner, *Macromolecules* **30**, 2092 (1997).
- [40] J. Giles, F. Gray, J. MacCallum, and C. Vincent, *Polymer* **28**, 1977 (1987).
- [41] F. Alloin, J. Sanchez, and M. Armand, *Electrochimica Acta* **37**, 1729 (1992).
- [42] T. Niitani, M. Shimada, K. Kawamura, K. Dokko, Y.-H. Rho, and K. Kanamura, *Electrochemical and Solid-State Letters* **8**, A385 (2005).
- [43] K. Xu, *Chemical Reviews* **104**, 4303 (2004).
- [44] J. L. Schaefer, D. A. Yanga, and L. A. Archer, *Chemistry of Materials* **25**, 834 (2013).

- [45] L. M. Bronstein, R. L. Karlinsky, B. Stein, Z. Yi, J. Carini, and J. W. Zwanziger, *Chemistry of Materials* **18**, 708 (2006).
- [46] K. L. Mathews, A. M. Budgin, S. Beeram, A. T. Joenathan, B. D. Stein, U. Werner-Zwanziger, M. Pink, L. A. Baker, W. E. Mahmoud, J. P. Carini, and L. M. Bronstein, *Journal of Materials Chemistry A* **1**, 1108 (2013).
- [47] T. Hamaide and C. Le Deore, *Polymer* **34**, 1038 (1993).
- [48] K. Ito, N. Nishina, Y. Tominaga, and H. Ohno, *Solid State Ionics* **86**, 325 (1996).
- [49] R. J. Klein and J. Runt, *The Journal of Physical Chemistry B* **111**, 13188 (2007).
- [50] R. Bouchet, T. Phan, E. Beaudoin, D. Devaux, P. Davidson, D. Bertin, and R. Denoyel, *Macromolecules* **47**, 2659 (2014).
- [51] Z. Xue, D. He, and X. Xie, *Journal of Materials Chemistry A* **3**, 19218 (2015).
- [52] M. H. Levitt, *Spin dynamics: basics of nuclear magnetic resonance, Second edition* (John Wiley & Sons, 2008).
- [53] R. Böhmer, K. Jeffrey, and M. Vogel, *Progress in Nuclear Magnetic Resonance Spectroscopy* **50**, 87 (2007).
- [54] T. Meersmann, *Relaxation and Coherenceherent Evolution as Competing Mechanisms for Coherence Transfer in Nuclear Magnetic Resonance Spectroscopy*, Ph.D. thesis, University of Lausanne (1997).
- [55] M. J. Duer, *Solid state NMR spectroscopy: principles and applications* (John Wiley & Sons, 2008).
- [56] A. Medek, J. S. Harwood, and L. Frydman, *Journal of the American Chemical Society* **117**, 12779 (1995).
- [57] M. R. Hansen, R. Graf, and H. W. Spiess, *Accounts of Chemical Research* **46**, 1996 (2013).
- [58] T. Asakura and I. Ando, *Solid state NMR of polymers*, Vol. 84 (Elsevier, 1998).

- [59] K. Saalwächter and H. Spiess, in *Polymer Science: A Comprehensive Reference* (Elsevier BV, 2012) pp. 185–219.
- [60] S. Wimperis, *Encyclopedia of Magnetic Resonance* (2011).
- [61] K. Schmidt-Rohr and H. W. Spiess, *Multidimensional Solid-State NMR and Polymers* (Academic Press, 1994).
- [62] A. G. Palmer III and C. Bracken, in *NMR in Supramolecular Chemistry* (Springer, 1999) pp. 171–190.
- [63] M. Goldman, *Journal of Magnetic Resonance* **149**, 160 (2001).
- [64] P. A. Beckmann, *Physics Reports* **171**, 85 (1988).
- [65] N. Bloembergen, E. M. Purcell, and R. V. Pound, *Physical Review* **73**, 679 (1948).
- [66] K. Hayamizu, Y. Aihara, and W. S. Price, *Journal of Chemical Physics* **113**, 4785 (2000).
- [67] L. G. Werbelow, *Encyclopedia of Magnetic Resonance* (2011).
- [68] L. A. Dissado and R. M. Hill, *Nature* **279**, 685 (1979).
- [69] G. Lipari and A. Szabo, *Biochemistry* **20**, 6250 (1981).
- [70] G. Lipari and A. Szabo, *Journal of the American Chemical Society* **104**, 4546 (1982).
- [71] R. M. Roque-Malherbe, *The Physical Chemistry of Materials: Energy and Environmental Applications* (CRC Press, 2010).
- [72] M. Kizilyalli, J. Corish, R. Metselaar, *et al.*, *Pure and Applied Chemistry* **71**, 1307 (1999).
- [73] W. S. Price, *NMR Studies of Translational Motion: Principles and Applications* (Cambridge University Press, 2009).
- [74] R. A. K. Bockris, John O'M., *Volume 1: Modern Electrochemistry*, edited by J. O. Bockris (Springer US, 1998).
- [75] J. Kerr, in *Lithium Batteries: Science and Technology* (Springer, 2003) pp. 575–622.

- [76] E. M. Terentjev, P. T. Callaghan, and M. Warner, *The Journal of Chemical Physics* **102**, 4619 (1995).
- [77] W. S. Price, *Concepts in Magnetic Resonance* **9**, 299 (1997).
- [78] K. A. Heisel, J. J. Goto, and V. V. Krishnan, *American Journal of Analytical Chemistry* **3**, 401 (2012).
- [79] E. Stejskal and J. Tanner, *The Journal of Chemical Physics* **42**, 288 (1965).
- [80] A. Pampel, F. Engelke, D. Groß, T. Oerther, and K. Zick, *Spin Report* **157-158**, 26 (2006).
- [81] D. Wu, A. Chen, and C. S. Johnson, *Journal of Magnetic Resonance, Series A* **115**, 260 (1995).
- [82] A. Pampel, D. Michel, and R. Reszka, *Chemical Physics Letters* **357**, 131 (2002).
- [83] A. Bielecki and D. P. Burum, *Journal of Magnetic Resonance, Series A* **116**, 215 (1995).
- [84] C. Ammann, P. Meier, and A. Merbach, *Journal of Magnetic Resonance* (1969) **46**, 319 (1982).
- [85] I. Kawamura, Y. Degawa, S. Yamaguchi, K. Nishimura, S. Tuzi, H. Saitô, and A. Naito, *Photochemistry and Photobiology* **83**, 346 (2007).
- [86] A. Asano, S. Hori, M. Kitamura, C. T. Nakazawa, and T. Kurotsu, *Polymer Journal* **44**, 706 (2012).
- [87] I. Kawamura, N. Kihara, M. Ohmine, K. Nishimura, S. Tuzi, H. Saitô, and A. Naito, *Journal of the American Chemical Society* **129**, 1016 (2007).
- [88] D. Golodnitsky, E. Livshits, A. Ulus, Z. Barkay, I. Lapidés, E. Peled, S. Chung, and S. Greenbaum, *The Journal of Physical Chemistry A* **105**, 10098 (2001).
- [89] J. K. Maranas, in *Polymers for Energy Storage and Delivery: Polyelectrolytes for Batteries and Fuel Cells* (American Chemical Society (ACS), 2012) pp. 1–17.

- [90] Z. Gadjourova, D. Martín y Marero, K. H. Andersen, Y. G. Andreev, and P. G. Bruce, *Chemistry of Materials* **13**, 1282 (2001).
- [91] R. Frech, S. Chintapalli, P. G. Bruce, and C. A. Vincent, *Chemical Communications*, 157 (1997).
- [92] O. Borodin and G. D. Smith, *Macromolecules* **39**, 1620 (2006).
- [93] A. Maitra and A. Heuer, *Physical Review Letters* **98** (2007).
- [94] D. Diddens, A. Heuer, and O. Borodin, *Macromolecules* **43**, 2028 (2010).
- [95] O. Borodin, G. D. Smith, and R. Douglas, *The Journal of Physical Chemistry B* **107**, 6824 (2003).
- [96] O. Borodin and G. D. Smith, *Macromolecules* **33**, 2273 (2000).
- [97] G. Mao, M.-L. Sabounji, D. L. Price, M. Armand, F. Mezei, and S. Pouget, *Macromolecules* **35**, 415 (2002).
- [98] Y. Wang, A. L. Agapov, F. Fan, K. Hong, X. Yu, J. Mays, and A. P. Sokolov, *Physical Review Letters* **108**, 088303 (2012).
- [99] K. Hayamizu, Y. Aihara, and W. S. Price, *Electrochimica Acta* **46**, 1475 (2001).
- [100] D. Davidson and R. Cole, *The Journal of Chemical Physics* **19**, 1484 (1951).
- [101] M. Zeidler, *Berichte der Bunsen-Gesellschaft für Physikalische Chemie* **95**, 971 (1991).
- [102] A. Friedrich, A. Dölle, and M. D. Zeidler, *Magnetic Resonance in Chemistry* **41**, 813 (2003).
- [103] S. Bhattacharja, S. Smoot, and D. Whitmore, *Solid State Ionics* **18-19**, **Part 1**, 306 (1986).
- [104] W. Gorecki, M. Jeannin, E. Belorizky, C. Roux, and M. Armand, *Journal of Physics: Condensed Matter* **7**, 6823 (1995).
- [105] T. H. Epps, T. S. Bailey, R. Waletzko, and F. S. Bates, *Macromolecules* **36**, 2873 (2003).

- [106] E. Beaudoin, T. N. Phan, M. Robinet, R. Denoyel, P. Davidson, D. Bertin, and R. Bouchet, *Langmuir* **29**, 10874 (2013).
- [107] R. O. Ebewele, *Polymer Science and Technology* (CRC Press, 2000).
- [108] L. Shen and Z. Chen, *Chemical Engineering Science* **62**, 3748 (2007).
- [109] U. Eliav and G. Navon, *Journal of Magnetic Resonance, Series A* **123**, 32 (1996).
- [110] N. Arun, S. Vasudevan, and K. Ramanathan, *Journal of Chemical Physics* **119**, 2840 (2003).
- [111] N. Arun, S. Vasudevan, and K. Ramanathan, *Journal of Chemical Physics* **119**, 2849 (2003).
- [112] T. Halstead, *The Journal of Chemical Physics* **53**, 3427 (1970).
- [113] W. Gorecki, P. Donoso, and M. Armand, *Brazilian Journal of Physics* **22**, 194 (1992).
- [114] W. A. Henderson, F. McKenna, M. A. Khan, N. R. Brooks, V. G. Young, and R. Frech, *Chemistry of Materials* **17**, 2284 (2005).
- [115] R. Kimmich, *Principles of Soft-Matter Dynamics: Basic Theories, Non-invasive Methods, Mesoscopic Aspects* (Springer, 2012).
- [116] S. Chung, Y. Wang, S. Greenbaum, D. Golodnitsky, and E. Peled, *Electrochemical and Solid-State Letters* **2**, 553 (1999).
- [117] C. Do, P. Lunkenheimer, D. Diddens, M. Götz, M. Weiß, A. Loidl, X.-G. Sun, J. Allgaier, and M. Ohl, *Physical Review Letters* **111**, 018301 (2013).
- [118] G. S. MacGlashan, Y. G. Andreev, and P. G. Bruce, *Nature* **398**, 792 (1999).
- [119] G. Lipari, A. Szabo, and R. M. Levy, *Nature* **300**, 197 (1982).
- [120] D. Golodnitsky, E. Livshits, Y. Rosenberg, E. Peled, S. Chung, Y. Wang, S. Bajue, and S. Greenbaum, *Journal of Electroanalytical Chemistry* **491**, 203 (2000).
- [121] R. Miao, B. Liu, Z. Zhu, Y. Liu, J. Li, X. Wang, and Q. Li, *Journal of Power Sources* **184**, 420 (2008).

- [122] A. M. Stephan and Y. Saito, *Solid State Ionics* **148**, 475 (2002).
- [123] S. W. Choi, S. M. Jo, W. S. Lee, and Y.-R. Kim, *Advanced Materials* **15**, 2027 (2003).
- [124] A. S. Gozdz, C. N. Schmutz, and J.-M. Tarascon, “Rechargeable lithium intercalation battery with hybrid polymeric electrolyte,” (1994), US Patent 5,296,318.
- [125] J.-M. Tarascon, A. Gozdz, C. Schmutz, F. Shokoohi, and P. Warren, *Solid State Ionics* **86-88**, 49 (1996).
- [126] B. S. Lalia, K. Yamada, M. Hundal, J.-S. Park, G.-G. Park, W.-Y. Lee, C.-S. Kim, and S. Sekhon, *Applied Physics A* **96**, 661 (2009).
- [127] P. Kubisa, *Journal of Polymer Science Part A: Polymer Chemistry* **43**, 4675 (2005).
- [128] C. M. Costa, M. M. Silva, and S. Lanceros-Méndez, *RSC Advances* **3**, 11404 (2013).
- [129] J. Xi, X. Qiu, J. Li, X. Tang, W. Zhu, and L. Chen, *Journal of Power Sources* **157**, 501 (2006).
- [130] N. Chung, Y. Kwon, and D. Kim, *Journal of Power Sources* **124**, 148 (2003).
- [131] C. Cheng, C. Wan, and Y. Wang, *Electrochemistry Communications* **6**, 531 (2004).
- [132] F. Tran-Van, L. Beouch, F. Vidal, P. Yammine, D. Teyssié, and C. Chevrot, *Electrochimica Acta* **53**, 4336 (2008).
- [133] C. Liao, X.-G. Sun, and S. Dai, *Electrochimica Acta* **87**, 889 (2013).
- [134] H. Ye, J. Huang, J. J. Xu, A. Khalfan, and S. G. Greenbaum, *Journal of The Electrochemical Society* **154**, A1048 (2007).
- [135] H.-B. Han, S.-S. Zhou, D.-J. Zhang, S.-W. Feng, L.-F. Li, K. Liu, W.-F. Feng, J. Nie, H. Li, X.-J. Huang, *et al.*, *Journal of Power Sources* **196**, 3623 (2011).

Etude par Résonance Magnétique Nucléaire de la mobilité du lithium dans les électrolytes à base de polymères

Résumé :

Dans les matériaux de batterie, le contrôle de la mobilité des cations lithium est la clé pour repousser les limites de la puissance et des vitesses de charge des batteries. La spectroscopie RMN permet de mesurer les coefficients d'auto-diffusion des espèces porteuses d'un spin nucléaire en utilisant des gradients de champ pulsés qui mesurent le déplacement atomique sur une échelle de 1-2 μm . La relaxation des spins nucléaires à des champs magnétiques élevés, d'autre part, est régie par les fluctuations des interactions à des fréquences proches de la fréquence de Larmor (fluctuant donc à l'échelle de la nanoseconde), et celles-ci sont généralement liées à des mouvements atomiques sur 1 Å - 1 nm. Dans cette thèse, nous avons mesuré les coefficients d'auto-diffusion et les temps de relaxation du ^7Li pour deux électrolytes polymères: LiTFSI dans de l'oxyde de polyéthylène (PEO) et dans un copolymère à blocs PS-PEO(LiTFSI)-PS. Les temps de relaxation ont été mesurés à trois champs magnétiques élevés (4.7, 9.4 et 17.6 Tesla) nous permettant d'effectuer une étude simple par relaxométrie des mouvements du Li^+ à l'échelle de la nanoseconde. Afin de reproduire l'ensemble des vitesses de relaxation, il est apparu nécessaire d'introduire un modèle simple à deux temps de corrélation. Ceci a montré pour la première fois que la dynamique de lithium dans PS-PEO(LiTFSI)-PS est ralentie par la présence de domaines de PS par rapport au PEO pur avec des longueurs de chaîne similaires. Les résultats sont analysés et comparés à d'autres études basées sur des modèles de dynamique moléculaire ou de diffusion dans les polymères. Une deuxième série d'électrolytes polymères en gel à base de poly(fluorure de vinylidène-co-hexafluoropropylène (PVDF-HFP), PEGM (Poly-éther méthylique d'éthylèneglycol méthacrylate)/PEGDM (Poly diméthacrylate d'éthylèneglycol), et LiTFSI dans les liquides ioniques ont également été étudiés. L'ajout de polymères oxygénés permet d'augmenter la rétention des liquides ioniques, mais ralentit la diffusion expliquant ainsi la baisse de performance de ces batteries à vitesse de charge élevée.

Mots clés : RMN, diffusion, relaxation, polymère, batterie, lithium

NMR study of lithium mobility in polymer electrolytes

Abstract :

In battery materials, the mobility of lithium cations is the key to the limitations in battery power and charging rates. NMR spectroscopy can give access to self-diffusion coefficients of spin bearing species using pulsed field gradients which measure atomic displacement over 1 – 2 μm length scales. The relaxation of nuclear spins at high magnetic fields, on the other hand, is governed by fluctuations of NMR interactions resonant with the Larmor frequency, at the nanosecond timescale, and these are usually related to atomic motions over 1 Å – 1 nm. In this thesis, we recorded self-diffusion coefficients and ^7Li relaxation rates for two polymer electrolytes: LiTFSI in polyethylene oxide (PEO) and in a block-copolymer PS-PEO(LiTFSI)-PS. We first investigated the effect of magic-angle spinning (MAS) on diffusion and relaxation, showing that MAS can help retrieve coefficient diffusion when relaxation is fast and diffusion is slow, and second, that lithium motion is not perturbed by the partial alignment of PEO under MAS induced pressure. The relaxation rates of ^7Li were measured at three high magnetic fields (4.7, 9.4 and 17.6 Tesla) allowing us to perform a simple relaxometry study of Li^+ motion at the nanosecond timescale. In order to reproduce the transverse and longitudinal relaxation behaviors, it proved necessary to introduce a simple model with two correlation times. It showed for the first time that the lithium dynamics in PS-PEO(LiTFSI)-PS is slowed down by the presence of PS domains compared to the pure PEO with similar chain lengths. The results are analyzed and compared to other studies based on molecular dynamics or physical models of diffusion in polymers. A second series of gel polymer electrolytes based on poly(vinylidene fluoride-co-hexafluoropropylene (PVdF-HFP), PEGM (Poly ethyleneglycol methyl ether methacrylate)/PEGDM (Poly ethyleneglycol dimethacrylate), and LiTFSI in ionic liquids were also studied. Adding oxygenated polymers to increase the retention of ionic liquids slowed the diffusion down and explained why the battery performance was degraded at higher charging rates.

Keywords : NMR, diffusion, relaxation, polymer, battery, lithium

